

NORTHWESTERN UNIVERSITY

# Study of Lasing in Random and Periodic Systems

A DISSERTATION

SUBMITTED TO THE GRADUATE SCHOOL  
IN PARTIAL FULFILLMENT OF THE  
REQUIREMENTS

for the degree

DOCTOR OF PHILOSOPHY

Field of Physics and Astronomy

By

XIAOHUA WU

EVANSTON, ILLINOIS

June 2007



## ABSTRACT

Experimental and numerical studies of lasing in multiple light scattering media with gain are presented in this thesis. Depending on the dielectric constant spatial distribution is random or periodic, two different kinds of lasers are discussed: the random laser and the photonic crystal laser. This thesis, therefore, is divided into two parts with each discussing one type of laser.

In the first part, we study on random lasers with the resonant feedback from both weakly and strongly scattering media. We choose the colloidal laser dye solutions as our weakly scattering systems, and experimentally demonstrate coherent random laser emission from them. We numerically illustrate the similarity (difference) between the quasimodes of a passive system and its lasing modes under a global (local) pumping. We also investigate the difference in statistics of the random lasing peaks and the stochastic amplified spontaneous emission spikes from the colloidal solutions, therefore distinguish their distinct physical mechanisms.

For random lasing in strongly scattering media, we utilize closely packed resonant scatterers to enhance the scattering strength and lower the lasing threshold. We synthesize monodispersed ZnO spheres to prepare the resonant scattering samples. We measure the transport mean free path by coherent backscattering, and compare the experimental data to the predicted value by Mie theory. We find that the dependent scattering occurs

when the scatterers are close to each other and the resonance from each single scatterer is changed. Nevertheless, we show that the resonant scattering indeed lowers the random lasing threshold.

The second part presents our studies on ZnO photonic crystal slab (PhCS) lasers. We design the PhCS structures with a triangular lattice by a band structure calculation. By varying the in-plane lattice constant, the air cylinder radius, and the ZnO slab thickness, we optimize the in-plane bandgap near ZnO maximum gain frequency. We fabricate the structures with FIB etching technique, and realize single mode lasing at room temperature under optical excitation. Moreover, the lasing wavelength is tuned across a 30 nm wavelength range by varying the lattice constant. The unavoidable fabrication defects can balance the vertical and lateral energy loss and facilitate the lasing.

## ACKNOWLEDGEMENTS

It has been a long but fruitful journey for me to pursuit my degree in Northwestern University. During the last six years, I have received professional training on various technical skills, gained precious experiences on experiment design and conductance, and most importantly, learned how to find and solve problems in scientific researches. All these gains would have been impossible to obtain without help from people all around me, and I would like to offer my most sincere thanks to them.

First, I would like to thank my advisor, Professor Hui Cao. Besides fundings and facilities which make my study in Northwestern possible, she always provides crucial guidance and detailed instructions for my research projects. Her strong support and challenging requirement greatly benefit me as a graduate student.

I thank my former and current colleagues in Professor Cao's group. As a theoretician, Dr. Alexey Yamilov have collaborated closely with me for almost all my projects, and taught me many numerical programming skills as well. Dr. Wei Fang, joined our group the same year with me, have been a very helpful friend with all my experiments and I enjoyed our inspiring discussions very much. Dr. Yong Ling and Dr. Junying Xu taught me various experimental skills when I first entered the group, and Dr. Bo Liu, Dr. Katyayani Seal, Dr. Andrey Chabanov and Dr. Mikhail Erementchouk have all helped me with their knowledge and experiences. I also thank all my colleague graduate

students: Heeso Noh, Jonathan Andreasen and Gideon Alon, who have always been willing to give me a helping hand in any concerns.

In my research projects, there have been extensive collaborations with other research groups. In Material Science and Engineering Department, I thank Professor R. P. H. Chang and his group members: Xiang Liu, Michael Scharrer, Eric Seelig, Min Yan, Jun Liu, Yan Li, and Haitao Zhang. Without the sample supply from them, my research would have been impossible. In the Electron Probe Instrumentation Center, I need to thank Professor Vinayak P. Dravid and other technical members: Dr. Shuyou Li, Dr. Gajendra Shekhawat and Ben Myers for training on FIB, AFM and SEM. In Electrical Engineering and Computer Science Department, I need thank Professor Seng-Tiong Ho and his group members: Dr. Guoyang Xu and Yingyan Huang for help me doing the rapid thermal annealing on my ZnO photonic crystals; Professor Allen Taflove and his group member Dr. Gilbert Chang for help on FDTD programming guidance; also Professor Prem Kumar and his group members for various inspiring discussions. In Chemistry Department, I need thank Professor George Schatz and his group member Dr. Shengli Zou for help on Mie scattering calculations of metal nanoparticles.

Finally, I must thank my family. My parents who bring me to this world and give me the educational opportunities to come this far, and my sibling who have been always supporting me with their lovely hearts and helpful hands. This thesis is dedicated to them.

## TABLE OF CONTENTS

ABSTRACT . . . . .	3
ACKNOWLEDGEMENTS . . . . .	5
LIST OF FIGURES . . . . .	9
LIST OF TABLES . . . . .	11
<b>1 INTRODUCTION . . . . .</b>	<b>12</b>
1.1 Light Scattering . . . . .	12
1.1.1 Single Scattering . . . . .	12
1.1.2 Multiple Scattering . . . . .	24
1.1.3 Coherent Backscattering . . . . .	29
1.1.4 Photon Localization . . . . .	35
1.2 Lasing in Multiple Light Scattering Systems . . . . .	40
1.2.1 Random Lasers . . . . .	41
1.2.2 Photonic Crystal Lasers . . . . .	48
1.3 Outline of This Thesis . . . . .	50
<b>2 COHERENT RANDOM LASERS IN WEAKLY SCATTERING COLLOIDAL DYE SOLUTIONS . . . . .</b>	<b>54</b>
2.1 Motivation . . . . .	54
2.2 Lasing Experiments in Colloidal Dye Solutions . . . . .	56
2.3 FDTD Simulation of Random Lasing in 2D Weakly Scattering Systems . . . . .	74
2.4 Quasimodes and Lasing Modes Calculation in 1D Random Systems . . . . .	83
2.5 Statistics of Amplified Spontaneous Emission Spikes and Coherent Ran- dom Laser Peaks . . . . .	101
2.6 Conclusion . . . . .	110
<b>3 COHERENT RANDOM LASERS IN CLOSELY PACKED RESONANT SCAT- TERING ZNO SPHERES . . . . .</b>	<b>112</b>
3.1 Motivation . . . . .	112
3.2 Chemical Synthesis of Monodisperse ZnO Spheres . . . . .	114
3.3 Self-Assembly and Optical Calibration of ZnO Opal Structures . . . . .	118
3.4 Coherent Backscattering of Light in Random Samples Formed by Closely Packed Resonant ZnO Spheres . . . . .	123
3.5 Lasing in Random Samples Formed by Closely Packed Resonant ZnO Spheres	133
3.6 Discussion and Conclusion . . . . .	141

4	ZNO PHOTONIC CRYSTAL SLAB LASERS . . . . .	146
4.1	Motivation . . . . .	146
4.2	Band Structure Calculation of ZnO Photonic Crystal Slabs . . . . .	148
4.3	Fabrication of ZnO Photonic Crystal Slab Lasers . . . . .	162
4.4	Optical Characterization of ZnO Photonic Crystal Slab Lasers . . . . .	167
4.5	Effect of Disorder on Photonic Crystal Lasers . . . . .	172
4.6	Conclusion . . . . .	180
5	CONCLUSION AND FUTURE WORK . . . . .	182

## LIST OF FIGURES

1.1	Mie scattering of a dielectric sphere . . . . .	19
1.2	Angular distribution of scattering from a dielectric sphere . . . . .	22
1.3	Time reversed paths in coherent backscattering . . . . .	30
2.1	Measured laser emission from TiO <sub>2</sub> colloidal solutions with Rhodamine dye	58
2.2	Measured lasing threshold from solutions with different particle density .	60
2.3	Measured angular distribution of both ASE and lasing emission from col- loidal dye solutions . . . . .	61
2.4	Measured emission spectra and excitation region images through cuvette side window . . . . .	64
2.5	Measured single shot lasing emission spectrum from colloidal solution and its correlation . . . . .	65
2.6	Measured single shot ASE emission spectrum from Rhodamine 640 solution	67
2.7	Measured effect of metallic rod position on lasing from colloidal solution	68
2.8	Measured single shot emission spectra from colloidal solutions with differ- ent dye concentration . . . . .	71
2.9	Calculated far-field intensity angular distribution of laser emission by gain guiding . . . . .	79
2.10	Comparison between the lasing mode and the quasimode from a weakly scattering 2D system . . . . .	80
2.11	Calculated quasimodes of 1D random systems and lasing modes under global gain . . . . .	89
2.12	Calculated intensity spatial distribution of quasimodes and lasing modes under global gain . . . . .	91
2.13	Calculated lasing modes threshold and spacing under local excitation . .	95
2.14	Calculated lasing modes from reduced system . . . . .	98
2.15	Measured emission spectra of ASE spikes and random lasing peaks . . . .	103
2.16	Measured ensemble-averaged spectral correlation and peak spacing statis- tics for ASE spikes and lasing peaks . . . . .	106
2.17	Measured peak height statistics of ASE spikes and random lasing peaks .	108
3.1	Setup for the synthesis of monodisperse ZnO powders . . . . .	115
3.2	SEM images for both polydisperse and monodisperse ZnO spheres . . . .	117
3.3	SEM images of self-assembled ZnO opal structures . . . . .	119
3.4	Measured transmission and reflection spectra of ZnO opals . . . . .	120
3.5	PBG center frequency and frequency width calculations for ZnO opals . .	123

	10
3.6 Measured Coherent backscattering cones from closely packed resonant ZnO spheres . . . . .	126
3.7 Transport mean free path of closely packed resonant ZnO spheres derived by CBS measurement . . . . .	128
3.8 Calculated scattering mean free path for clusters with different number of spheres . . . . .	131
3.9 Calculated transport mean free path for clusters with different number of spheres . . . . .	132
3.10 Measured random lasing spectra of closely packed resonant ZnO spheres .	134
3.11 Measured average random lasing threshold change with individual ZnO sphere size . . . . .	135
3.12 Calculated average threshold for 2D random lasers change with scatterer size . . . . .	138
3.13 Calculated standard deviation of 2D random laser threshold change with scatterer size . . . . .	139
4.1 Super-cell used in photonic band structure simulation for ZnO PhCS . .	151
4.2 Symmetric and antisymmetric solutions for ZnO PhCS super-cell structures	152
4.3 Calculated band structure of ZnO PhCS structures . . . . .	154
4.4 Calculation of integrated E and H components in ZnO PhCS . . . . .	155
4.5 Experimentally measured emission intensity from ZnO film as a function of polarization angle. . . . .	157
4.6 Calculated optimization of PBG for ZnO PhCS on radius and thickness .	158
4.7 Calculated polarization degree of the modes $M$ and $K$ k-points for lowest four bands . . . . .	161
4.8 TEM and SEM images of ZnO films grown on sapphire substrate . . . .	163
4.9 The setup sketch of focused ion beam etching process . . . . .	165
4.10 Top and side SEM images of ZnO PhCS fabricated by FIB . . . . .	166
4.11 Sketch of lasing experiment setup on ZnO PhCS samples . . . . .	168
4.12 Measured emission spectrum and spatial profile of a localized lasing mode	169
4.13 Measured emission spectrum and spatial profile of a extended lasing mode	171
4.14 Measured wavelength tuning with ZnO PhCS laser by changing lattice constant . . . . .	173
4.15 Structure deviation of fabricated ZnO PhCS from the ideal template . . .	175
4.16 Calculated balance between $Q_{//}$ and $Q_{\perp}$ by disorder in PhCS structures	177

## LIST OF TABLES

2.1	Calculated frequencies and quality factors of lasing modes and quasimodes	81
3.1	Measured ZnO opal PBG center wavelength for different sphere sizes by transmission . . . . .	121
3.2	Measured fluctuation of lasing threshold change with individual ZnO sphere size . . . . .	136

## CHAPTER 1

### INTRODUCTION

#### 1.1 Light Scattering

The interaction process between a light wave and matter can be simply described as follows: the incoming electromagnetic field induces an electric polarization in the object with some energy dissipation into the object, which is called absorption. This polarization generates a new outgoing EM wave from the object, which is called scattering. The often referred to terms "transmission" or "reflection" can be viewed as a special scattering case where the scattering angle is 0 or 180 degrees. Light scattering is so crucial to our everyday life that without it we cannot even see the world around us. Moreover, scattering offers a powerful tool for studies on both light and matter.

##### *1.1.1 Single Scattering*

We start with the simplest scattering problem: the interaction of an incoming plane wave  $E_0(\vec{r})e^{-i\omega t}$  with a single object. The incoming wave induces the charge distribution inside the object to vary sinusoidally in time, generating a vector potential  $A(\vec{r}, t)$ . The radiative electromagnetic field caused by  $A(\vec{r}, t)$  can be expanded as multiple radiation components leading with an electric dipole term, followed by a magnetic dipole field,

electric quadrupole field, magnetic quadrupole field and so on. When the object size is much smaller than incoming wavelength, the leading dipole field term is dominant [1]:

$$\begin{aligned}\mathbf{E} &= \frac{1}{4\pi\epsilon_0} \left\{ k^2(\mathbf{n} \times \mathbf{p}) \times \mathbf{n} \frac{e^{i\mathbf{k}\mathbf{r}}}{r} + [3\mathbf{n}(\mathbf{n} \cdot \mathbf{p}) - \mathbf{p}] \left( \frac{1}{r^3} - \frac{i\mathbf{k}}{r^2} \right) e^{i\mathbf{k}\mathbf{r}} \right\} \\ \mathbf{H} &= \frac{ck^2}{4\pi} (\mathbf{n} \times \mathbf{p}) \frac{e^{i\mathbf{k}\mathbf{r}}}{r} \left( \mathbf{1} - \frac{\mathbf{1}}{i\mathbf{k}\mathbf{r}} \right)\end{aligned}\quad (1.1)$$

where  $\mathbf{p}$  is the dipole momentum, and  $k$  is the scattered wave number. In the far field zone ( $kr \gg 1$ ), the first term in  $\mathbf{E}$  and  $\mathbf{H}$  is dominant, while in the near field zone ( $kr \ll 1$ ), the second term is dominant. The time-averaged power radiation per unit solid angle by  $\mathbf{p}$  is

$$\frac{dP}{d\Omega} = \frac{1}{2} \text{Re}[r^2 \mathbf{n} \cdot \mathbf{E} \times \mathbf{H}^*] \quad (1.2)$$

where  $\mathbf{E}$  and  $\mathbf{H}$  are given by Eq. 1.1. If we only consider the leading term in both  $\mathbf{E}$  and  $\mathbf{H}$ , we find

$$\frac{dP}{d\Omega} = \frac{ck^4}{32\pi^2\epsilon_0} |(\mathbf{n} \times \mathbf{p}) \times \mathbf{n}|^2 = \frac{ck^4}{32\pi^2\epsilon_0} \sin^2\theta \quad (1.3)$$

where  $\theta$  is angle between  $\mathbf{n}$  and  $\mathbf{p}$ . The total power radiated is

$$P = \frac{ck^4}{12\pi\epsilon_0} |\mathbf{p}|^2 \quad (1.4)$$

The radiated power can be viewed as "scattered" energy from the incoming wave, so a virtual *scattering cross section* with units of area can be defined as

$$\sigma_s = \frac{P}{|\mathbf{S}_{\text{inc}}|} = \frac{P}{\frac{c\epsilon_0}{2} |\mathbf{E}_{\text{inc}}|^2} \quad (1.5)$$

where  $\mathbf{S}_{\text{inc}}$  is the incident energy flux. Similar to Equ. 1.2, the *differential scattering cross section* is

$$\frac{d\sigma_s}{d\Omega} = \frac{\frac{dP}{d\Omega}}{|\mathbf{S}_{\text{inc}}|} = \frac{k^4}{(4\pi\epsilon_0)^2} \frac{|\mathbf{p}|^2}{|\mathbf{E}_{\text{inc}}|^2} \sin^2\theta \quad (1.6)$$

The  $k^4$  dependence of the differential (and total) scattering cross section on wave number (or on wavelength as  $\lambda^{-4}$ ) is an almost universal characteristic of the long-wavelength limit scattering by any finite system. This dependence on frequency is known as *Rayleigh's law*, and the dipole scattering is known as *Rayleigh scattering*. Both  $\sigma_s$  and  $\frac{d\sigma}{d\Omega}$  include the term  $\frac{|\mathbf{p}|^2}{|\mathbf{E}_{\text{inc}}|^2}$ , which needs a brief discussion here. We know that induced polarization  $\mathbf{P} = \epsilon_0\chi_e\mathbf{E}$ , where  $\chi_e = \epsilon/\epsilon_0 - 1$  is called the *electric susceptibility* of the medium. The term  $\epsilon$  is the *electric permittivity* and the frequently used term *dielectric constant* is  $\epsilon_r = \epsilon/\epsilon_0$ . Generally  $\epsilon$  and  $\chi_e$  are tensors and  $\mathbf{P}$  and  $\mathbf{E}$  are vectors pointing in different directions. Only in isotropic media are  $\epsilon$  and  $\chi_e$  scalars and  $\mathbf{P}$  and  $\mathbf{E}$  point along the same direction. Two things need to be noticed: first, in Eq. 1.5 and 1.6 there is an incident wave  $\mathbf{E}_{\text{inc}}$ , not a local field  $\mathbf{E}$ , thus one has to find the relation between them by solving the recursive polarization equation; second, in Equ. 1.5 and 1.6 there is an electric dipole moment  $\mathbf{p}$ , which is usually a volume integration over the local polarization

**P.** As a very simple example of dipole scattering, we consider a small dielectric sphere of radius  $a$  with  $\mu_r = 1$  and a uniform isotropic dielectric constant  $\epsilon_r$ , the electric dipole momentum can be calculated to be [1]

$$\mathbf{p} = 4\pi\epsilon_0 \left( \frac{\epsilon_r - 1}{\epsilon_r + 2} \right) \mathbf{a}^3 \mathbf{E}_{\text{inc}} \quad (1.7)$$

Substituting Eq. 1.7 into Eq. 1.6 and 1.5, we get

$$\begin{aligned} \frac{d\sigma_s}{d\Omega} &= k^4 a^6 \left| \frac{\epsilon_r - 1}{\epsilon_r + 2} \right|^2 \sin^2\theta \\ \sigma_s &= \frac{8\pi}{3} k^4 a^6 \left| \frac{\epsilon_r - 1}{\epsilon_r + 2} \right|^2 \end{aligned} \quad (1.8)$$

Though Equ. 1.8 is for the particular case of dipole scattering from a small dielectric sphere, some general conclusions can be drawn from it: (1): the electric dipole scattering cross section has the characteristic  $k^4$  dependence. (2): the electric dipole scattering cross section has  $V^2$  dependence, where  $V$  is the volume of the scatterer. (3): the differential scattering cross section shows the  $\sin^2\theta$  angular distribution. One has to notice that  $\theta$  is the angle between the dipole momentum  $\mathbf{p}$  and scattering direction  $\mathbf{n}$ , not the incoming field  $\mathbf{E}_{\text{inc}}$ . Only for specific conditions are  $\mathbf{E}_{\text{inc}}$  and  $\mathbf{p}$  in the same direction. In such cases, if we define a scattering plane formed by an incoming wave vector  $\mathbf{k}$  and scattering direction  $\mathbf{n}$ , then for  $\mathbf{E}_{\text{inc}}$  perpendicular to the scattering plane,  $\theta = 90^\circ$ , while for  $\mathbf{E}_{\text{inc}}$  parallel to the scattering plane, the usual referred to *scattering angle* is  $90^\circ - \theta$ .

Besides being scattered, the incoming light can also be absorbed if the scatterer has

complex refractive index  $n_s$ . Similar to scattering, the energy loss from absorption can be described by an *absorption cross section*  $\sigma_{abs}$ . We can speculate the expression of  $\sigma_{abs}$  by simple unit analysis: we know that  $\sigma_s \propto V^2 \lambda^{-4}$  for small scatterers and the absorbed energy should be proportional to the scatterer volume  $V$  for small scatterers. Then, naturally, we would expect  $\sigma_{abs} \propto V \lambda^{-1}$ , which can be confirmed by a careful derivation. The total energy loss by scattering and absorption is usually termed *extinction*, and as usual it can be characterized by an *extinction cross section*  $\sigma_{ext}$ , where  $\sigma_{ext} = \sigma_{sca} + \sigma_{abs}$  holds. People also define *efficiencies* for extinction, scattering, and absorption as  $Q = \sigma/G$ , where  $G$  is the particle cross-section area projected onto a plane perpendicular to the incident beam (e.g.,  $G = \pi a^2$  for a sphere of radius  $a$ ). Consequently,  $Q_{ext} = Q_{sca} + Q_{abs}$ .

More strictly, the conditions for Rayleigh scattering are (a) scatterer size  $\ll \lambda/2\pi$  and (b)  $|m| \cdot \text{scatterer size} \ll \lambda/2\pi$ , where  $m = n_s/n_m$  is the *relative refractive index*, meaning the ratio between scatterer refractive index  $n_s$  and medium refractive index  $n_m$ . If the scatterer is a sphere with radius  $a$ , then these conditions can be simplified to (a)  $x \ll 1$  and (b)  $|m|x \ll 1$ , where  $x = 2\pi n_m a/\lambda = ka$  is called *size parameter*. Physically, these conditions mean the scatterer size is much smaller than the wavelength inside the scatterer. Thus the scatterer can be treated as if in a uniform field and the induced dipole momentum follows the incoming field oscillation *instantly*. This condition justifies that the dipole momentum obtained in Eq. 1.7 can be obtained by the static electric field calculation. Similar theory can be applied to arbitrary shaped scatterers if they satisfy the Rayleigh scattering condition, in particular, their dipole momentum  $\mathbf{p}$

can be calculated by electrostatics theory and the (differential) scattering cross section can be obtained by Eq. 1.5 and 1.6.

When the scatterer gets larger, the scattering problem gets very complicated. First, the scatterer cannot be simplified as an electric dipole any more, because radiation from higher ordered multipoles (magnetic dipole, electric quadrupole and so on) have to be taken into account. Second, the relation between the induced charge distribution and the incident field cannot be treated as in the static case, but Maxwell's equations with boundary conditions for the particular scatterer have to be solved strictly. As a consequence of the *linearity* of Maxwell's equations and the boundary conditions, the amplitude of the scattered field is a linear function of the amplitude of the incident field. In the *far-field region*, where  $kr \gg 1$ , the scattered field  $\mathbf{E}_s$  can be decomposed into two components  $E_{s\parallel}$  and  $E_{s\perp}$ , which are parallel and perpendicular to the scattering plane. The relation between incident and scattered fields is conveniently written in matrix form as [2]

$$\begin{pmatrix} E_{s\parallel} \\ E_{s\perp} \end{pmatrix} = \frac{e^{ik(r-z)}}{-ikr} \begin{pmatrix} S_2, S_3 \\ S_4, S_1 \end{pmatrix} \begin{pmatrix} E_{i\parallel} \\ E_{i\perp} \end{pmatrix} \quad (1.9)$$

where the elements  $S_j$  ( $j = 1, 2, 3, 4$ ) of the *amplitude scattering matrix* depend, in general, on  $\theta$ , the *scattering angle*, and the azimuthal angle  $\varphi$ . One can easily see that in the general case with a non-diagonal amplitude scattering matrix, the polarization of the incident field is changed by scattering. The scattering problem is greatly simplified if the scatterer is a sphere, where  $S_3 = S_4 = 0$  and  $S_1$  and  $S_2$  depend only on  $\theta$ . Moreover,

when  $\theta = 0$ ,  $S_1 = S_2 \equiv S(0)$ , the polarization is kept in the forward direction.

In fact, the sphere is one of the few geometries whose scattered field can be analytically obtained after solving Maxwell's equations. Such a scattering problem is usually termed *Mie theory* for his famous work in 1908. We would like to skip the lengthy mathematics of Mie theory and directly use its results. Interested readers can refer to references such as [2, 3] for more details. The differential scattering cross section and total scattering cross section are given as:

$$\begin{aligned}\frac{d\sigma_s}{d\Omega} &= \frac{1}{k^2} (|S_1(\theta)|^2 \sin^2\varphi + |S_2(\theta)|^2 \cos^2\varphi) \\ \sigma_s &= \frac{2\pi}{k^2} \sum_{n=1}^{\infty} (2n+1) (|a_n|^2 + |b_n|^2)\end{aligned}\tag{1.10}$$

where

$$\begin{aligned}S_1(\theta) &= \sum_{n=1}^{\infty} \frac{2n+1}{n(n+1)} \{a_n \pi_n(\cos\theta) + b_n \tau_n(\cos\theta)\} \\ S_2(\theta) &= \sum_{n=1}^{\infty} \frac{2n+1}{n(n+1)} \{b_n \pi_n(\cos\theta) + a_n \tau_n(\cos\theta)\}\end{aligned}\tag{1.11}$$

It can be seen that the  $\theta$  dependence of the differential scattering cross section is from functions  $\pi$  and  $\tau$ , while the coefficients  $a_n$  and  $b_n$  determine the dependence on  $m$  and  $x$ . The extinction cross section  $\sigma_{ext}$  is also given here without proof:

$$\sigma_{ext} = \frac{4\pi}{k^2} \text{Re} \{S(0)\}\tag{1.12}$$

To get a flavor of Mie scattering, we calculate two cases: (1) a linear polarized plane wave ( $\lambda = 600$  nm) incident on a sphere of  $m = 2.2 + 0.01i$ , whose radius  $a$  varies from

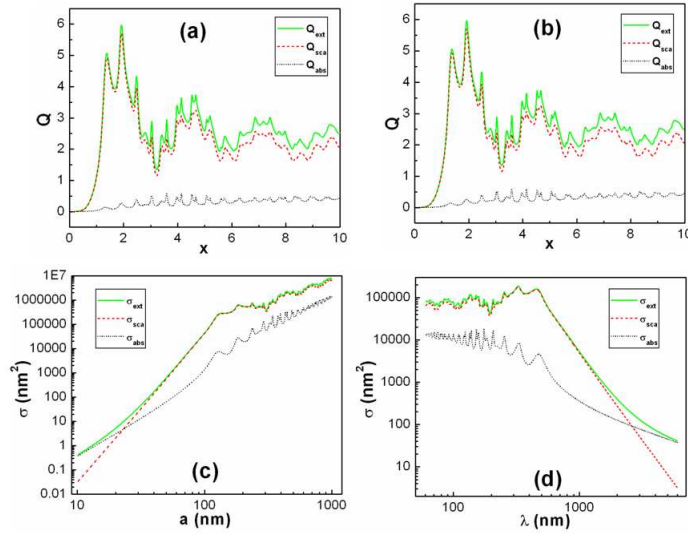


Figure 1.1: Calculated Extinction (solid lines),scattering (dashed lines) and absorption (dotted lines) efficiency  $Q$  [(a),(b)] and cross section  $\sigma$  [(c),(d)] of a sphere with  $m = 2.2 + 0.01i$  in air. (a) and (c): fixed incident wavelength  $\lambda = 600\text{nm}$ , varying sphere radius  $10\text{nm} < a < 1\mu\text{m}$ . (b) and (d): fixed sphere size  $a = 100\text{nm}$ , varying incident wavelength  $60\text{nm} < \lambda < 6\mu\text{m}$ . (a) and (b) are plotted in size parameter  $x = 2\pi a/\lambda$ .

10 nm to 1  $\mu\text{m}$ ; (2) a sphere of  $m = 2.2 + 0.01i$  with radius  $a = 100$  nm with an incident linear polarized plane wave, whose  $\lambda$  varies from 60 nm to 6  $\mu\text{m}$ . The results are shown in Fig. 1.1 (a) and (c) for case 1, while (b) and (d) for case 2. A few interesting points can be seen from the results so let us explore them one by one: (1) with the log-log plot in (c), Rayleigh scattering  $\sigma_{sca} \propto a^6$  can be clearly seen for small scatterers ( $a < 100$  nm), while absorption  $\sigma_{abs} \propto a^3$  is also shown for even smaller scatterers. (2) still in (c), for large scatterers ( $a > 500$  nm),  $\sigma_{sca}$  and  $\sigma_{abs}$  both scale with the geometric cross section of scatterers as  $a^2$  as expected from geometrical optics. (3) with the log-log plot in (d), Rayleigh scattering  $\sigma_{sca} \propto \lambda^{-4}$  can be clearly seen for long wavelength ( $\lambda > 1 \mu\text{m}$ ), while absorption  $\sigma_{abs} \propto \lambda^{-1}$  is also shown for even longer  $\lambda$ . (4) still in (d), for short

wavelength ( $\lambda < 100$  nm),  $\sigma_{sca}$  and  $\sigma_{abs}$  saturate at a certain value, which is related to the scatterer geometry cross section  $\pi a^2$  as expected from geometrical optics. (5) when we plot efficiency  $Q$  instead of  $\sigma$ , and replace  $a$  or  $\lambda$  with size parameter  $x = 2\pi a/\lambda$  for either cases, we get exactly the same result. This means when considering efficiency, neither  $a$  nor  $\lambda$  but their ratio  $a/\lambda$  matters. Mathematically, this originates from the  $x$  dependence of  $a_n$  and  $b_n$  in Equ. 1.10 and 1.12. (6) a few characteristic features are shown in the plot of  $Q$  vs.  $x$  in (a): first, there is a series of regularly spaced broad maxima and minima called the *interference structure*, which are interpreted as the interference between the incident and forward-scattered waves. The phase difference between them is  $\Delta\phi = 2ka(n_s - n_m) = 2x(m - 1)$ . The condition for their destructive interference is  $\Delta\phi = (2p + 1)\pi$  where  $p$  is an integer. Then the positions of the maxima can be determined as  $x = (2p + 1)\pi/2(m - 1)$ . Notice that the interference structure only shows in  $Q_{ext}$  and  $Q_{sca}$ , but not in  $Q_{abs}$ ; second, there is some irregular fine structure called *ripple structure*, which is explained by the electromagnetic normal modes of the sphere. They are resonant when the denominator of the scattering coefficients  $a_n$  and  $b_n$  are minima. Physically, a sphere has its own eigenmodes with complex frequencies, and under resonant conditions they can be excited by the incident field. These resonances offer the possibility to enhance scattering and absorption: with larger  $m$ , both  $Q_{sca}$  and  $Q_{abs}$  can be enhanced many times, but the linewidths of such resonances get much narrower at the same time, thus it is more difficult to hit them. (7) it seems that both  $Q_{ext}$  and  $Q_{sca}$  tend to saturate at certain values when  $x \rightarrow \infty$ . In fact, in such a limit,

$Q_{ext} \rightarrow 2$ , is *twice* as large as predicted by geometrical optics. This puzzling result is called the *extinction paradox*, which can be explained by the missed consideration of diffraction from the sphere boundary in geometrical optics.

So far we have only considered the total scattering cross section  $\sigma_{sca}$ , next let's see how the scattered light distributes in angle, which is shown by the differential scattering cross section  $d\sigma_{sca}/d\Omega$ . From Eq. 1.10 and 1.11, we can see that the angular dependence lies in the scattering matrix elements  $S_1$  and  $S_2$ . As an example, let's study the angular distribution for a sphere ( $m = 2.2 + 0.01i$ ) in an incident plane wave with  $\lambda = 600$  nm, the same case as Fig. 1.1 (a) and (c). We checked three different sizes as shown in Fig. 1.2 (a) to (c), which actually correspond to  $x = 0.4, 2.0$  and  $10.0$  respectively. From Eq. 1.9,  $S_1$  and  $S_2$  describe the scattered field perpendicular and parallel to the scattering plane separately. For small size as in (a), the scattering is just like Rayleigh scattering,  $E_{s\perp}$  is isotropic while  $E_{s\parallel}$  becomes zero at  $\theta = 90^\circ$ . With increasing sphere size, the angular distribution gets more complicated having a trend with the scattered field more and more concentrated in the forward direction as shown in (b) and (c), with more and more fine structures in their angular dependence. To characterize such a trend, the average cosine of the scattering angle, or the *asymmetry parameter*  $g$  is

$$g = \langle \cos\theta \rangle = \frac{\int_{4\pi} \frac{d\sigma_{sca}}{d\Omega} \cos\theta d\Omega}{\int_{4\pi} \frac{d\sigma_{sca}}{d\Omega} d\Omega} \quad (1.13)$$

For our dielectric sphere with three sizes shown in Fig. 1.2 (a) to (c),  $g$  is calculated to be 0.045, 0.493, and 0.662. Clearly, with  $a$  increasing, the scattered field concentrates

more and more in the forward direction and  $g$  gradually increases from 0 to 1.

Two particular angles need special attention, forward scattering  $\theta = 0^\circ$  and backward scattering  $\theta = 180^\circ$ , where  $|S_1| = |S_2| \equiv |S|$ . With increasing  $a$ , it can be seen that  $|S(0^\circ)| / |S(180^\circ)|$  keeps increasing from (a) to (c), which is consistent with the scattered field concentrating in the forward direction. We calculate the backscattering cross section  $\sigma_{back} = |S(180^\circ)|^2 / k^2$  and forward scattering cross section  $\sigma_{forw} = |S(0^\circ)|^2 / k^2$ , and the results, as well as their ratio, are plotted in Fig. 1.2 (d). Interestingly, their ratio has a resonant peak around  $a = 300$  nm, instead of a monotonic change as one may expect.

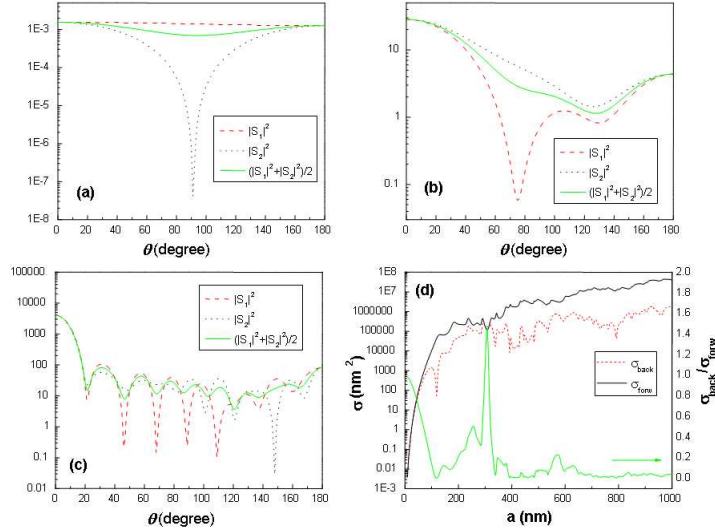


Figure 1.2: Calculated  $|S_1|^2$  (dashed lines),  $|S_2|^2$  (dotted lines) and average  $(|S_1|^2 + |S_2|^2)/2$  (solid lines) as functions of scattering angle  $\theta$  from spheres ( $m = 2.2 + 0.01i$ ) of different radius  $a$ : (a) 38.2 nm, (b) 191 nm (c) 955 nm under a linearly polarized incident plane wave with  $\lambda = 600$  nm. (d) backscattering cross section  $\sigma_{back}$  (dashed lines) and forward scattering cross section  $\sigma_{forw}$  (solid lines), as well as their ratio for scattering from a sphere ( $m = 2.2 + 0.01i$ ,  $\lambda = 600$  nm) of changing radius  $a$ .

We have to point out that though the relative refractive index  $m$  and size parameter  $x$  are treated as independent *mathematical* variables in Mie theory, they are not *physically*

independent because of the dispersion of  $m$ , which should be  $m(\lambda)$  instead. Then, though the plots in Fig. 1.1 (a) and (b) are the same, it better be understood as the first case: fixed  $\lambda$  with varying  $a$ . The particular  $m = 2.2 + 0.01i$  we chose is similar to ZnO in the visible light frequency range, but it definitely changes when  $\lambda$  varies from 60 nm to 6  $\mu\text{m}$ . When considering the scattering of a fixed sized scatterer with different incident  $\lambda$ , dispersion has to be taken into account and the real cases of (a) and (b) are surely different.

In fact, such a dispersion relation can have a more dramatic influence on scattering and absorption. For example, let's look back to Equ. 1.7, where we have the  $(\epsilon_r - 1)/(\epsilon_r + 2)$  expression for the polarization of a small sphere. Such polarization affects the scattering cross section and absorption cross section as shown in Equ. 1.8. Because of the frequency dependence of  $\epsilon_r$ , there exists some resonance frequency where  $\epsilon_r + 2$  vanishes, where both  $\sigma_{sca}$  and  $\sigma_{abs}$  are greatly enhanced. For small scatterers ( $mx \ll 1$ ), we derived that  $\sigma_{sca} \propto \lambda^{-4}$  and  $\sigma_{abs} \propto \lambda^{-1}$  without considering dispersion. Now with the  $\lambda$  dependence of  $m$ , such conclusions are not accurate. A good example is the scattering from metal nanoparticles like silver or gold, whose resonance occur in the visible light frequency range where the  $\lambda^{-4}$  dependence of  $\sigma_{sca}$  and  $\lambda^{-1}$  dependence of  $\sigma_{abs}$  are broken. The other consequence of the strong dispersion of metal is that both scattering and absorption are shape sensitive, even for very small scatterers. Because of the different expressions of the polarization parameter, their resonance frequencies can be quite different, as well as the resonant peak amplitudes.

In summary, we mainly discussed scattering from a single scatterer in this section. It was shown that scattering can be enhanced by resonances caused by (1) interference structure (2) normal modes (3) polarizability, which are all determined by scatterer shape, size, and refractive index. However, absorption is also enhanced by the latter two types of resonance, and for small scatterers, because  $\sigma_{sca} \propto V^2$  and  $\sigma_{abs} \propto V$ , absorption can even dominate over scattering.

### 1.1.2 *Multiple Scattering*

Following the consideration for single scattering in the previous section, it's natural to study scattering from a collection of scatterers. In this case, every scatterer is not only in the external incident field and its own scattered field, but also in the scattered fields from all other scatterers in the system. Strictly speaking, such a multiple scattering problem can also be solved by finding the solutions to Maxwell's equations satisfying all the boundary conditions at each scatterer. However, the number of equations increases linearly with the number of scatterers, and for a random system including thousands of scatterers which we encounter frequently in real life, finding such exact solutions is impractical even with our current computation power. Only under certain conditions (e.g. all the scatterers are the same and placed periodically in space), can the scattered field be obtained exactly. On the other hand, in many cases, we do not need to know the detail of the EM field inside the system, but only be concerned with the transportation behavior such as transmission or reflection from a slab shaped random sample. Such

behavior can be well characterized by introducing some statistical parameters of the random system, which will be briefly discussed in this section.

A simple but important assumption is made in this section: *independent scattering* occurs, which means the density of scatterers is so dilute that the incident light is only scattered once by each scatterer before leaving the system. In other words, the total scattered field is the sum of all the scattered fields from each scatterer. Since the scatterers are randomly distributed in space, the phase relation between all the scattered fields is also randomized, then the scattering cross section of the system is the sum of scattering cross sections  $\sigma_s$  from each scatterer. Now we introduce the important concept of *mean free path* in multiple scattering. A mean free path is a characteristic length scale describing the scattering process. For instance, the *scattering mean free path*  $l_s$  is defined as the average distance between two successive scattering events. For a random system composed of monodisperse scatterers with density  $\rho$ , the scattering mean free path is

$$l_s = \frac{1}{\rho\sigma_s} \quad (1.14)$$

where  $\sigma_s$  is the scattering cross section of each scatterer. Another important mean free path is the *transport mean free path*  $l_t$ , which is defined as the average distance after which the momentum of incident wave is randomized, which is given by:

$$l_t = \frac{l_s}{1 - \langle \cos\theta \rangle} = \frac{1}{\rho\sigma_s(1 - \langle \cos\theta \rangle)} \quad (1.15)$$

where  $\langle \cos\theta \rangle$  is the asymmetry parameter of each scatterer as we introduced in the single scattering section. The characteristic length scale relevant for absorption is the *inelastic mean free path*  $l_i$ , which is defined as the traveled length over which the intensity is reduced by a factor  $e^{-1}$  due to absorption by scatterers.

There are two other relevant length scales: the size of the system  $L$  and the wavelength  $\lambda$ . Typically,  $L \gg \lambda$  is satisfied when dealing with multiple scattering problems. By comparing  $l_t$  with  $\lambda$  and  $L$ , we can divide the random system into a few different regimes: (1)  $L \ll l_t$ : the system is optically thin in this region and the interaction with light is small, such a system is sometimes referred to as being in the *ballistic regime*. (2)  $\lambda \ll l_t \ll L$ : light propagation in such a system is diffusive and the transport can be considered as a random walk of photons with a step length equal to the scattering mean free path. This region is called the *diffusive regime*. (3)  $l_t < \lambda$ : light interacts with scatterers within one wavelength of propagation and the transport behavior is completely changed. It is believed that the interference between the scattered waves could make the propagation stop and light is localized spatially. This region is called the *localization regime*.

Multiple light scattering mainly occurs in regimes (2) and (3). In this section we will consider regime (2), leaving regime (3) to a later section. In the diffusive regime, the electromagnetic wave propagation is modeled by the random walk of photons, and interference is neglected due to the low probability for scattered light to return to its starting coherent volume. Thus, photon propagation can be described by the diffusion

equation for the photon density,  $n(\mathbf{r}, \mathbf{t})$ ,

$$\frac{\partial n(\mathbf{r}, \mathbf{t})}{\partial t} = D\nabla^2 n(\mathbf{r}, \mathbf{t}) - \frac{\mathbf{v}}{l_i} \mathbf{n}(\mathbf{r}, \mathbf{t}) \quad (1.16)$$

where  $D = l_t v/3$  is the diffusion coefficient and  $v$  is the transport velocity for the light inside the medium. Here we consider the case without any source term, otherwise, a source term needs to be added to the right hand side of the equation. The diffusion equation is a second order partial differential equation and accordingly it needs boundary conditions before it can be solved. As an example, a slab shaped sample with thickness  $L$  is treated following Ref. [4]: For a thick slab with  $L \gg l_t$ , the maximum diffuse photon density,  $n'$ , due to a collimated beam of photon flux  $j_{in}$  incident normal to the surface at  $x = 0$ , occurs within a few mean free paths of the surface and has a magnitude calculated from transport theory of  $n' = 5j_{in}/v$ . With the boundary conditions  $n(0) = n'$  and  $n(L) = 0$ , the steady-state solution for Equ. 1.16 is  $n(x) = n' \sinh[\alpha(L-x)] / \sinh(\alpha L)$  with  $\alpha = (Dl_i/v)^{-1/2}$ . The photon current density is given by

$$j(x, t) = -D \frac{\partial n(x, t)}{\partial x}, \quad (1.17)$$

and thus, the the current density at the exit plane is  $j(L) = n' \sinh(\alpha D) / \sinh(\alpha L)$ . The normalized transmission,  $T(L) = j(L)/j_{in}$ , can therefore be written as

$$T(L) = \frac{10\alpha D/v}{e^{\alpha L} - e^{-\alpha L}} \quad (1.18)$$

Let's consider two limiting cases: (1)  $\alpha L \ll 1$ , then  $T(L) = 5D/vL$  (2)  $\alpha L \gg 1$ , then  $T(L) = (10\alpha D/v)\exp(-\alpha L)$ . Using the relation  $D = vl_t/3$  in case (1), we get

$$T(L) = 5l_t/3L. \quad (1.19)$$

The average distance between beginning and ending points of a trajectory traveled in time  $t$  is  $\sqrt{Dt}$ , while the length of such a trajectory is  $vt$ . Thus, the *diffusive absorption length*  $L_a$  (the RMS average of  $l_i$ ) which describes the penetration depth of light in an absorbing multiple scattering medium is  $\sqrt{Dt_a} = \sqrt{vl_t/3 \times l_i/v} = \sqrt{l_t l_i/3}$ . So it is clear that  $\alpha = 1/L_a$  and  $\alpha L \ll 1$  means the system size  $L$  is much smaller than the diffusive absorption length  $L_a$ . In such conditions, the absorption can be neglected and the diffusive total transmission is  $T \propto l_t/L$ . And for case (2), where  $L \gg L_a$ , absorption cannot be neglected. In fact, for a large system the transmission exponentially decreases with system size  $L$  due to absorption.

In summary, we introduced three important length scales in a multiple light scattering system: scattering mean free path  $l_s$ , transport mean free path  $l_t$  and diffusive absorption length  $L_a$ . By comparing wavelength  $\lambda$ , transport mean free path  $l_t$  and system size  $L$ , we introduced the diffusive region where multiple light scattering is described by the diffusion equation and the important relation between total transmission and  $l_t$  as well as  $L$  is given:  $T \propto l_t/L$ . The scattering strength of a random system can be described by either  $l_t$  or the diffusion coefficient  $D$ . The smaller  $l_t$  is, the stronger the system scatters. Though not explicitly shown,  $l_s$  and  $l_t$  are obviously frequency dependent. One point we

need to mention: the independent scattering approximation can only be justified with very dilute scatterer densities, because with a high scatterer density, their scattering cross sections start to overlap and the total scattering will decrease. In particular, Eq. 1.14 and 1.15 hold only for low scatterer densities with a filling fraction  $f \leq 0.1$ . [5] For higher densities  $0.1 \leq f \leq 0.6$ , the scattering cross section  $\sigma_s$  must be rescaled as  $\sigma_s \rightarrow \sigma_s(1 - f)$  [6], while for  $f \geq 0.6$ , a more complicated rescaling parameter needs to be used [7]. Though determining  $l_t$  theoretically is not very easy for high scatterer densities, coherent backscattering offers us a simple way to get  $l_t$  experimentally, as we will discuss in next section.

### 1.1.3 Coherent Backscattering

In the last section, multiple light scattering was described by the photon density (or light intensity) diffusion equation (Equ. 1.16) when  $\lambda \ll l_t \ll L$ . This diffusion model, though describing many experimental phenomena well (e.g. transmission), ignored the interference effect. However, interference can definitely survive multiple scattering, one good example is the speckle pattern we often observe in the transmission or reflection of a coherent laser light beam from random media. If the scatterers are allowed to move over distances on the order of the wavelength of the light or more at the time scale of the measurement, the spatial distribution of the scattered intensity will be the average of a rapidly changing speckle pattern and therefore essentially flat. Liquid random samples in which the scatterers are subject to Brownian motion, or rigid random samples that

are spun, yield scattered flat intensity patterns as if interference between light paths did not exist. One type of interference, however, survives. In the exact backward direction of the incident light, the waves that travel along the same light path in opposite directions (time-reversed paths) will always have the same phase and interfere constructively. Moving away from this direction, a difference in phase develops, and the summation of scattered waves from different paths eventually get incoherent. As a measurable consequence, the intensity of scattered light in the backwards direction would be *twice* that of the intensity in other directions. This phenomenon is called *coherent backscattering* (CBS). A more quantitative picture of CBS in real space is quoted from Ref. [8]: Consider

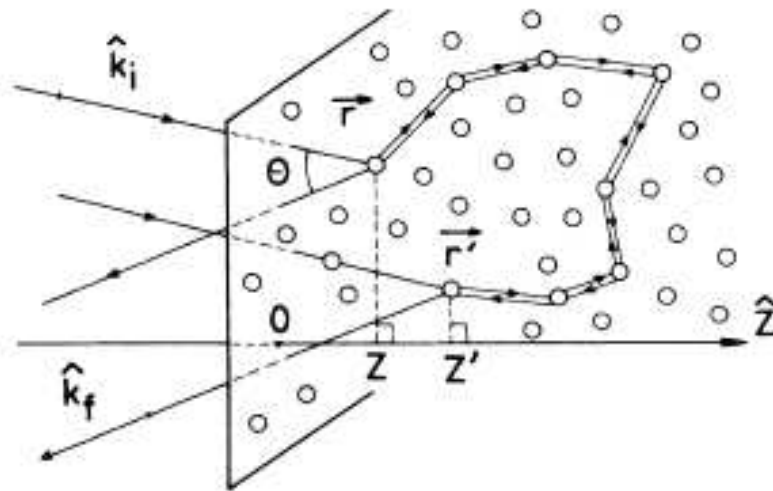


Figure 1.3: Geometry used for the calculation of the coherent albedo, showing two interfering light paths. Cited from Ref. [8].

a plane wave of wave vector  $\mathbf{k}_i$  (wavelength  $\lambda$ ) experiencing a series of elastic scattering events characterized by the wave vectors  $\mathbf{k}_i, \mathbf{k}_1, \dots, \mathbf{k}_n = \mathbf{k}_f$ , where  $\mathbf{k}_j$  is the wave vector after the  $j^{\text{th}}$  scattering event and  $\mathbf{k}_f$  stands for the final wave vector. In classical

transport theory all  $n$ -order sequences are assumed to be uncorrelated as a result of the random nature of the distribution of scatterers. However, any given sequence and its time reversed counterpart  $\mathbf{k}_i, -\mathbf{k}_{n-1}, -\mathbf{k}_{n-2}, \dots, -\mathbf{k}_1, \mathbf{k}_f$ , where the light is scattered by the same centers but in opposite order, can interfere constructively for a special choice of  $\mathbf{k}_f$  relative to  $\mathbf{k}_i$ . The total phase shift  $\Delta\phi$  between the two corresponding partial waves is

$$\Delta\phi = (\mathbf{k}_f \cdot \mathbf{r}_1 - \mathbf{k}_i \cdot \mathbf{r}_n) - (\mathbf{k}_f \cdot \mathbf{r}_n - \mathbf{k}_i \cdot \mathbf{r}_1) = (\mathbf{k}_i + \mathbf{k}_f) \cdot (\mathbf{r}_1 - \mathbf{r}_n) = \frac{4\pi}{\lambda} \sin\left(\frac{\theta}{2}\right) |\mathbf{r}_1 - \mathbf{r}_n|, \quad (1.20)$$

where  $\mathbf{r}_1$  and  $\mathbf{r}_n$  are the positions of the first and last scattering centers, and  $\theta$  is the angle between  $\mathbf{k}_i$  and  $\mathbf{k}_f$  as shown in Fig. 1.3. With increasing  $\theta$ , the interference for an individual light path will oscillate with the period determined by  $|\mathbf{r}_1 - \mathbf{r}_n|$ . With increasing  $|\mathbf{r}_1 - \mathbf{r}_n|$ , the oscillation period gets smaller and smaller. The total scattered field is the sum of all the partial waves from time reversed pairs like  $\mathbf{r}_1$  and  $\mathbf{r}_n$ . Thus, at backscattering direction ( $\theta = 0$ ), all pairs interfere constructively, and at large  $\theta$ , the interference is averaged out by different pairs and the summation is incoherent. Thus, within a certain solid angle around the direction of exact backscattering there will be an enhanced intensity cone. Since the average value of  $|\mathbf{r}_1 - \mathbf{r}_n|$  is  $\sqrt{D\tau}$ , where  $\tau$  is the time period the photon stays inside the sample and  $D = l_t v/3$  is the diffusion coefficient. For the shortest sequence ( $n = 2$ ) the mean distance between two scattering events is the scattering mean free path  $l_s$ , thus the CBS cone width is expected to be proportional to  $\lambda/\sqrt{l_t l_s}$ . Since  $l_t$  and  $l_s$  are proportional, it is usually said that the CBS cone width is

expected to be proportional to  $\lambda/l$  where  $l$  is the mean free path.

The above discussion is surely a coarse estimation with many approximations. First, the vector property of the EM wave is ignored and the field is treated as a scalar. Experiments have been performed to study CBS in both the polarization conserved and polarization crossed channels. For linearly polarized incident light, this is realized by detecting the scattered field after it passes through a linear polarizer either parallel or perpendicular to that of the incident light. It is shown that a CBS cone with a peak height close to 2 is only observed in the parallel channel, while in the perpendicular channel, a much smaller peak is observed. This is explained as following: the polarization of the scattered field is, in general, different from the polarization of the incident field. For the two inverse scattering loop drawn in Fig. 1.3, however, the polarization component parallel to the incident polarization is the same. Thus, full coherence between both loops is maintained in the parallel channel and a CBS cone is seen. In the other channel, the polarization component is different for the two loops and coherence is lost so no strong CBS cone should be observed. This discussion also justifies the scalar theory for the CBS in the parallel channel.

The predicted factor of 2 is difficult to obtain experimentally for a few reasons. The first reason is the single scattering events at the sample surface, which are ignored in the theoretical consideration. The sum of all the single scattering events does not provide the enhanced backscattering cone, therefore it reduces the enhancement factor. This drawback can be fixed by using a circular-polarized incident field in stead of a linearly polarized

one, so the scattered field measurement is only for the helicity conserved component. Because single scattering of a circular-polarized wave changes its helicity, its contribution to the scattered field is removed automatically. Indeed, for a circular-polarized incident field, a CBS cone closer to 2 was obtained in the helicity conserved channel, and in the helicity reversed channel the scattered light was more isotropic and the CBS cone was closer to 1. The other ignored factor is the recurrent scattering, where  $\mathbf{r}_n = \mathbf{r}_1$ . In such closed scattering loops, the two reversed scattering sequences will give constructive interference in any  $\mathbf{k}_i$  and  $\mathbf{k}_f$ , thus there is no CBS cone in such cases. However, the probability for occurrence of recurrent scattering is quite small when  $\lambda \ll l_s$ , thus this effect is not as strong as single scattering events. But when scattering gets stronger, the recurrent scattering events cannot be ignored, which we will discuss in the next section.

The detailed derivation of the CBS albedo was given in Ref. [9] which we will not discuss here. However, to understand the physical meaning of such an albedo, we cite Equation (1) in Ref. [9]:

$$\alpha(\mathbf{k}_0, \mathbf{k}, \mathbf{t}, \mathbf{t}') \propto \sum_{\mathbf{i}, \mathbf{j}, \mathbf{l}, \mathbf{m}} \mathbf{A}(\mathbf{r}_i, \mathbf{t}; \mathbf{r}_j, \mathbf{t}') \times \mathbf{A}^*(\mathbf{r}_l, \mathbf{t}; \mathbf{r}_m, \mathbf{t}') e^{i\mathbf{k}_0 \cdot (\mathbf{r}_i - \mathbf{r}_l) + i\mathbf{k} \cdot (\mathbf{r}_m - \mathbf{r}_j)} \quad (1.21)$$

The definition of all the variables are as follows:  $A(\mathbf{r}_i, \mathbf{t}; \mathbf{r}_j, \mathbf{t}')$  is the complex amplitude of the field at  $(\mathbf{r}_j, \mathbf{t}')$  from an impulse point source at  $(\mathbf{r}_i, \mathbf{t})$ ;  $\mathbf{k}_0$  and  $\mathbf{k}$  are the incident and scattered wave vectors. The scattered intensity  $\alpha$  from the medium is obtained from the product of  $A$  and  $A^*$ , weighted by the external phase factors of the incoming and outgoing waves summed over the coordinates of the initial and final points of the

scattering sequences. For coherent backscattering, we only need to consider the coherent part of  $AA^*$ , where  $\mathbf{r}_i = \mathbf{r}_l$  and  $\mathbf{r}_j = \mathbf{r}_m$ . It can be seen that the scattered albedo is nothing but the Fourier transform of the product of  $A$  and  $A^*$ , which can be viewed as the intensity of the light scattered from  $\mathbf{r}_i$  to  $\mathbf{r}_j$ . Therefore, a smaller angle  $\theta$  corresponds to a longer path from  $\mathbf{r}_i$  to  $\mathbf{r}_j$ . In other words, closer to the backscattering direction, the more contribution there is from the longer paths inside the sample.

The above idea can be experimentally tested by studying the CBS albedo change as we control the contribution from different path lengths inside the sample. The first way to change the contribution is via the geometry confinement, in particular, by gradually reducing the sample thickness so that more and more long paths will be terminated. It was shown that thinner samples did show the decrease of the cone height, which confirmed the idea that enhancement near the backscattering direction is mainly from long light paths inside the sample [10, 11]. An alternative way to reduce the contribution of long paths is by introducing absorption into the sample. Due to the exponential decrease of the scattered light intensity with path length induced by absorption, the contributions from long paths are reduced to the CBS albedo outside the sample. This idea was also tested experimentally and indeed the albedo peak decreased when absorption was introduced into the sample [11]. A subtle difference exists in the results of these two methods: geometry confinement only truncates the longer paths without affecting the short paths while absorption reduces both long and short paths. Such a difference causes different changes to the CBS albedo: in the former case the wings of the backscattering peak are

completely unaffected, whereas in the latter case there is a slight decrease of the albedo even in the wing part [11]. Instead of reducing the contribution from the longer paths, one can also enhance it by introducing gain into the sample. Because the scattered field is exponentially amplified with path length, longer paths dominate over the short ones in their contribution to the scattered field and a narrowing of the CBS cone would be expected. Such an idea was proposed in theory [12] and realized in experiment [13].

With the development of measurement techniques, high angular resolution has been obtained which facilitates the better study of coherent backscattering phenomenon. Using circular-polarized incident light, a CBS albedo with an enhancement factor very close to 2 has been realized in the helicity conserved channel. With good fitting to theory, the transport mean free path  $l_t$  can be derived very precisely. We know that  $l_t$  is a very important parameter to describe a random system, so experimental determination of  $l_t$  is crucial. Besides coherent backscattering, dynamic transmission measurement is also used frequently to determine the diffusion coefficient  $D$ , from which  $l_t$  is derived. However, in the latter cases, the scattered light propagation speed  $v$  has to be carefully determined before a reliable  $l_t$  can be obtained.

#### 1.1.4 *Photon Localization*

In the last section, we discussed the coherent backscattering of light in random samples, which is actually also termed *weak localization* of light. It is often referred to as the precursor of *strong* localization of light. The backscattered intensity is enhanced within the

CBS cone, whose width is proportional to  $\lambda/l_t$ . When scattering gets stronger inside the sample,  $l_t$  gets smaller and the CBS cone gets wider, thus more light is scattered backwards. The increase of backscattered light means the decrease of transmission, and hence of the optical diffusion coefficient  $D$ . For sufficiently strong scattering,  $D$  approaches zero and the diffusive propagation stops, which is called strong localization of light.

The idea of localization was first brought up by Anderson when he originally considered electron transportation in a random potential [14]. Later a scaling theory of localization was developed by Edwards and Thouless, who proposed a criterion for localization basing on the sensitivity of electrons to the boundary of the sample [15]. Physically, it predicted localization may happen when the "boundary leakage induced energy shift"  $\Delta E$  is less than the average energy level spacing between states of the sample  $dE/dN$ . Furthermore, it was argued that the parameter,  $\Delta E/(dE/dN)$ , is directly related to electronic transport in the sample, since it can be identified with the dimensionless conductance  $g$ . Abrahams and co-workers further developed a scaling theory and concluded that for infinite one and two dimensional systems, an arbitrary small disorder can make all the states be localized; while for systems of higher dimension, there exists a mobility edge separating extended and localized states [16]. The mobility edge was believed to be the Ioffe-Regel criterion  $kl \approx 1$  where  $k$  is the electron wave number and  $l$  is the mean free path in the random system [17]. However, an unequivocal experimental test of the scaling theory was hampered by the nearly inescapable presence of electron-electron interactions and electron-phonon scatterings in real materials. The request to avoid such

drawbacks urged people to look for localization of electromagnetic waves propagating in strongly scattering dielectric structures [18, 19]. It is interesting that, even though the wave behavior of photons was known much earlier than electrons, the localization behavior, which is regarded as a general interference consequence for any wave in random media, was proposed for light later than for electrons.

There are interesting similarities between the propagation of light in a disordered dielectric and electrons in, for example, a disordered semiconductor or metal. If we write the wave equation of light in the format of the Schrödinger equation for an electron, we get the frequency dependent *potential* for light

$$V(\mathbf{r}, \omega) = -\frac{\omega^2}{c^2}(\epsilon(\mathbf{r}) - 1) \quad (1.22)$$

with  $\epsilon(\mathbf{r})$  being the dielectric constant of the medium. This frequency dependent potential makes light scattering different from electron-impurity scattering. Though Anderson localization of electrons was expected to occur at low energy, this is not true for photons. A generally accepted condition for Anderson localization of light in three dimensional systems is the Ioffe-Regel criterion  $k_e l_s \leq 1$ . This criterion was originally put forward in 1960 by Ioffe and Regel who argued that  $k_w l_s$  must necessarily be greater than unity (in fact  $2\pi$  in their original paper) since a mean free path less than wavelength is no longer compatible with the idea of a traveling wave. The  $\omega^2$  dependence of the potential in the Rayleigh scattering regime (i.e. in the limit  $\omega \rightarrow 0$ ), leads to the  $\omega^4$  dependence of the scattering cross section. Consequently  $l_s \propto \omega^{-4}$  at small frequencies, which causes

$kl_s \propto \omega^{-3} \rightarrow \infty$  as  $\omega \rightarrow 0$ . For the other limit  $\omega \rightarrow \infty$ , one enters the geometrical optics regime where the scattering cross section equals twice that of the geometrical cross section for non absorbing scatterers, then  $l_s$  is independent of  $\omega$ , which causes  $kl_s \propto \omega \rightarrow \infty$  as  $\omega \rightarrow \infty$ . So the Ioffe-Regel criterion cannot be satisfied in both low and high frequency limits. As a result, localization of light, if possible, can only be obtained at the intermediate frequencies.

The intermediate frequency regime is the resonant scattering regime, where the scattering cross section is indeed large at resonances, and the mean free path  $l_s$  is expected to be small. The existence of such a frequency window has been predicted and the localization length has been calculated [20]. It was concluded that localization should occur in a two-component composite when the refractive index contrast exceeds a certain minimum value that is in the range of 2.1-2.5. Moreover, the optimal filling fraction of the high index component for the observation of localization was found to be 0.35-0.45. However, this optimistic calculation is based upon the extrapolation of results obtained in the low-density limit, and such an extrapolation might not be justified. In particular, we made use of the independent scattering approximation to get  $l_s = 1/\rho\sigma_s$ , which does not hold for a higher density  $\rho$ . At higher  $\rho$ , the scattering cross section from each scatterer starts to overlap and dependent scattering happens, which tends to decrease the collective scattering efficiency, thereby make it more difficult to realize localization of light. An alternative way to realize light localization was proposed by John [21] to utilize the low density of states in the photonic band gap. He showed that the wavenumber

in the Ioffe-Regel criterion is replaced by the crystal momentum, which vanishes at the Brillouin-zone boundary to make  $k_{cryst}l_s \leq 1$ . Thus, localization might be achieved with relative ease near a (pseudo-) gap of such a crystal.

After discussion of the possibility for existence of strong localization of light, the question comes: how can we deduce the existence of Anderson localization experimentally? The scaling theory of localization [16] is an attempt to answer this question. According to the scaling theory of localization, the energy leakage of a *localized* state from the boundary can be expressed by a scale-dependent transport mean free path  $l_t(L) \propto L^{-1}$ . Therefore, the transmission is expected to behave as  $T \propto L^{-2}$  rather than  $T \propto L^{-1}$  as in the diffusive regime. Such rescaling phenomenon was indeed observed for microwaves within a particular frequency window around  $\nu = 19$  GHz for strong scattering metallic spheres [22]. In 1997, Wiersma and co-workers showed the similar super linear dependence of transmission on sample length in GaAs powders samples for light with  $\lambda = 1064$  nm [23]. However, their results were questioned for the absorption effect in their samples [24,25]. In 1999, Schuurmans and co-workers studied the coherent backscattering from strong scattering GaP samples, they attributed the rounding of the CBS cone to the onset of Anderson localization by excluding both finite sample size and absorption effects [26]. Chabanov and co-workers proposed a different way to characterize photon localization by measuring the relative fluctuation of a certain transmission quantity  $var(s_a)$  [27], and they experimentally demonstrated the localization of microwaves by resonant scatterers under such criterion [28]. Very recently, Storzer and co-workers

showed the time resolved transmission of 590 nm light through strongly scattering TiO<sub>2</sub> samples, and observed deviation from diffusion which cannot be explained by absorption, sample geometry, or reduction in transport velocity [29]. Following the proposal by John [21], some experiments also have been conducted to explore light localization in photonic crystals with certain disorder [30,31].

## 1.2 Lasing in Multiple Light Scattering Systems

As the main purpose of this thesis, lasing phenomena are studied in multiple light scattering systems. Depending on the amount of randomness, all systems can be divided into three different regimes: (i) strongly periodic structures, (ii) strongly random structures, (iii) partial-periodic and partial-random structures. In the first regime, periodic structures are often called *photonic crystals*, whose density of states distribution is strongly modulated by the spatial periodicity of the dielectric constant. Partial or complete gaps can be formed in their dispersion and lasing from both defect states in the gap and bandedge states outside the gap have been extensively studied both theoretically and experimentally. In the second regime, strong dielectric constant fluctuation scatters light severely and the dwell time of photons inside the sample is enhanced dramatically. As we discussed in previous sections, photons go through diffusive propagation when  $\lambda \ll l_t \ll L$  with small probability for the occurrence of recurrent scattering events. With scattering strength increased,  $l_t$  is decreased and recurrent scattering becomes more frequent. Eventually, when  $kl_t \rightarrow 1$ , diffusion is completely stopped and photon localiza-

tion is achieved by interference between all the recurrent scattered partial waves. In other words, localized modes are formed whose wave function exponentially decays spatially. With gain introduced into the system, those localized modes can start to lase when their loss is compensated by amplification. This phenomenon is called *random lasing* to differentiate from the conventional laser cavity with mirrors. In this sense, random lasing is closely related to photon localization and provides an important tool to experimentally study those localized modes. The third regime is the intermediate regime between the first two, and it can be treated as either periodic structures with random defects (disordered photonic crystal) or random structures with short or long range orders (correlated random structure). Lasing in this regime is thus often extrapolated from either photonic crystal lasers or random lasers study.

### 1.2.1 *Random Lasers*

In order to facilitate a comparison between the laser systems analyzed in this thesis, we first present a succinct overview of the physical principles behind conventional lasers.

The word *laser* stands for Light Amplification by Stimulated Emission of Radiation (LASER). A laser system includes two parts: an oscillator, which supplies optical feedback, and an amplifier which coherently amplifies the light. The oscillator and amplifier can be separated or combined into one resonator cavity. The amplification is achieved by the gain medium, which is placed inside the cavity. Three kinds of interactions between light and gain material happen during lasing: spontaneous emission, stimulated emission

and absorption. In the spontaneous emission process, there is no definite phase relation among all the photons emitted from different atoms and they can be emitted into any direction. In the stimulated emission process, an incident photon triggers the emission of many identical photons, which combine coherently with the incident photon. By absorption process, we only mean the absorption of pump light by the gain medium to excite it to higher energy levels. In a laser resonator, the photons spontaneously emitted along the cavity axis are reflected back into the gain medium by mirrors and amplified through stimulated emission on each passage through the gain medium. Lasing occurs when the gain in a round trip exceeds the loss for the frequencies satisfying the phase condition of oscillation. The loss can be output coupling loss, scattering loss during the passage inside the cavity, or reabsorption loss inside the cavity.

In a conventional laser cavity, scattering is detrimental since it increases the loss and hence the threshold gain. However, in a strongly scattering gain medium, light scattering plays a positive role: (i) multiple scattering increases the path length or dwell time of light in the gain medium, thus enhancing light amplification by stimulated emission; (ii) recurrent light scattering provides coherent feedback for lasing oscillation. Therefore, under suitable conditions, the combination of *optical coherent amplification* and *multiple light scattering* in active random media leads to *random laser* action. In other words, the random laser represents the process of light amplification by stimulated emission with feedback provided by disorder-induced scattering. There are two kinds of feedback: one is *intensity* or *energy* feedback; the other is *field* or *amplitude* feedback. The former

feedback is incoherent and non-resonant, the latter is coherent and resonant. Based on the feedback mechanisms, random lasers are classified into two categories: (1) random lasers with incoherent (or non-resonant) feedback, also called incoherent random lasers, (2) random lasers with coherent (or resonant) feedback, also called coherent random lasers.

There has been tremendous interest in various types of random lasers since the invention of cavity lasers. For a good review of both experimental and theoretical work on random lasers, readers can refer to Ref. [32,33]. Here, we will only give a brief historical introduction. In 1968, Letokhov proposed self-generation of light in an active medium filled with scatterers [34]. From the discussion in previous sections, we know that when  $\lambda \ll l_t \ll L$ , the propagation of photons is diffusive with a diffusion coefficient  $D$ . From the second limit  $\alpha L \gg 1$  of Eq. 1.18, the transmission  $T$  decays exponentially with system size  $L$  having a coefficient  $\alpha = L_a^{-1} = (l_t l_i / 3)^{-1/2}$ .  $L_a$  is the diffusive absorption length and  $l_i$  is the inelastic mean free path. Now considering an active system with gain instead of absorption, we can define the gain length  $l_g$  similarly as  $l_i$ , over which the intensity is increased by a factor of  $e$ . Similarly, diffusive gain length can be defined as  $L_g = (l_t l_g / 3)^{1/2}$ . Then, from Eq. 1.18,  $T$  will exponentially increase with  $L$  when  $L \gg L_g$ . In other words, the total transmission will diverge by increasing the system size. The critical criterion is  $L = L_g$ , at which the total transmission is equal to the total incidence. Physically, this means on average every photon generates another photon before escaping the medium. When  $L \geq L_g$ , more than one photon is generated by each

incident photon before its exit from the system thus the photon number increases with time. In reality the light intensity will not diverge because gain depletion quickly sets in and  $l_g$  increases. Since in this model the interference is ignored, it is called incoherent random lasing with energy or intensity feedback.

Experimental study of random lasers started in the 1980's with samples made from laser crystal powders [35]. They reported intense stimulated radiation over a wide range of  $Na^{3+}$ -activated scattering media. Because in such a system gain and scattering are both from the powder, the effect of multiple light scattering on emission mechanism was not clear. It would be better to separate gain and scattering and study both independently. This idea was realized experimentally in 1994 [36], with  $TiO_2$  micro particle suspensions with laser dye rhodamine 640 perchlorate as gain material, scattering and gain were controlled separately by varying particle concentration and dye molarity. A threshold was found for emission intensity increasing and emission linewidth narrowing from the solutions and the threshold depended on particle concentration, which clearly showed the feedback was provided by light scattering. These were the characteristic behaviors of a random laser with intensity feedback.

The discovery of Lawandy *et al* triggered many experimental and theoretical studies of such colloidal dye suspensions, and the incoherent random lasers were realized under various conditions. Detailed experimental studies on lasing threshold dependence, emission spectral shape, emission dynamics,  $\beta$  factor and many other properties were performed by many groups. Theoretical simulations based on the light diffusion model

were proposed to explain all the observed experimental results. Here we will only discuss one point which was ignored sometimes in these studies: the reabsorption of the emission in the solution outside of the excited region. Besides the often checked criterion  $\lambda \ll l_t \ll L$ , there is a hidden requirement for applying the diffusion model:  $l_t \ll l_i$ , which means that light diffusion can only occur when absorption is very weak. Otherwise, after the emitted photon exits the excitation region, it will be quickly absorbed even before being scattered. So we should divide the typical experimental conditions into a few different regimes: (1) the characteristic size of excitation region (or gain volume)  $L_e$  is much larger than  $l_t$ , and there is weak reabsorption outside  $l_t \ll l_i$ . In this case, emitted light will diffusively propagate both inside and outside the gain volume with an extended length  $L_a = (l_t l_i / 3)^{1/2}$ , and the diffusion model can be applied to this total system with a size of  $L_e + L_a$ . (2)  $L_e \gg l_t$  but  $l_t \geq l_i$ , then the emitted light will be strongly absorbed outside the gain volume and cannot return to it, so the diffusion model can only be applied to the gain volume of size  $L_e$ . (3)  $L_e \leq l_t$  and  $l_t \ll l_i$ , in this case the diffusion model can only be applied to the total size  $L_e + l_i$ , not just  $L_e$ . (4)  $L_e \leq l_t$  and  $l_t \geq l_i$ , in this case the diffusion model cannot be used since light will be absorbed before diffusion occurs. In all of these cases, one has to consider the relation between these different length scales:  $l_t$ ,  $l_i$ ,  $L_e$  and the total system size  $L$  when analyzing the experimental results.

The random laser with incoherent feedback, where the interference effect has been ignored, only requires that light return to the gain volume instead of to its original

scattering coherent volume. As a consequence, the characteristic of such random lasers is the smooth and narrow emission spectrum close to the frequency of maximum gain. This behavior is very similar to another well known phenomenon: amplified spontaneous emission (ASE). However, ASE can even be observed in pure gain material without scattering as long as the excitation region is large and the excitation is strong enough, while in the incoherent random laser process feedback from scattering is necessary.

The random laser with field feedback is formed by the interference of scattered waves which return to the same coherence volume via different *closed* paths. Thus scattering provides coherent (phase-sensitive) and resonant (frequency-dependent) feedback for lasing, leading to the selection of discrete lasing frequencies. The coherent random laser was first demonstrated in disordered ZnO powders and polycrystalline films by Cao in 1998 [37, 38]. When the excitation pulse energy exceeded a certain threshold, discrete narrow peaks emerged in the emission spectrum. The linewidth of these peaks was sub nanometer, which was much narrower than the typical incoherent random laser emission linewidth. The frequencies of the sharp peaks depended on the local dielectric configuration at the pumped region. The mean free path  $l_t$  was found to be close to  $\lambda$ , which indicated very strong scattering close to the localization regime in their samples. The coherence of random lasing peaks was confirmed by photon statistics measurement, which indeed showed the Poisson distribution above threshold pumping for a single lasing mode [39].

The dependence of the lasing threshold on the transport mean free path  $l_t$ , pump area

size  $L_e$  and gain length  $l_g$  for the coherent random laser was studied in detail [40]. The decrease of the lasing threshold with  $l_t$  confirmed the contribution of multiple scattering to this random laser action. Moreover, the transition from an incoherent random laser to a coherent random laser with increasing scattering was observed experimentally [41]. Such a transition can be understood by considering lasing from eigenmodes of Maxwell's equations for a random medium. Owing to the finite size of the random medium, the eigenenergies are complex numbers, whose imaginary parts represent the decay rates. Through the coupling to the outside reservoir (i.e., to the EM modes outside the random medium), the eigenmodes interact with each other. In the diffusion regime, the average decay rate of an eigenmode is larger than the mean frequency spacing of adjacent modes. Hence, the eigenmodes are spectrally overlapped, giving a continuous emission spectrum for lasing with incoherent (or non-resonant) feedback. When scattering increases, the dwell time of light in the random medium increases. The decrease of their coupling to the outside reservoir weakens the interaction among the modes. When the eigenmodes are spectrally separated, laser emission from them gives discrete peaks in the emission spectrum, which is the random laser with coherent (or resonant) feedback.

So far we discussed two types of random lasers: the incoherent random laser in the diffusion regime and the coherent random laser in the near localization regime, and the transition between them by increasing scattering has been shown. One interesting observation is that a coherent random laser can be realized in the diffusion regime with  $kl_t \gg 1$  [40, 41]. Similar phenomena were also observed by Vardeny and co-workers

with a series of experiments in many different weak scattering systems:  $\pi$ -conjugated polymer films [42, 43], organic-dye-doped gel films [44], synthetic opals infiltrated with  $\pi$ -conjugated polymers and dyes [44, 46, 47], biological tissues [48, 49]. The physical mechanism of these observations have not been clearly and different models have been proposed trying to explain such observations [50, 51]. In Chapter 2, we will discuss our study on random lasing with resonant feedback from weakly scattering colloidal solutions in detail both experimentally and theoretically.

### 1.2.2 Photonic Crystal Lasers

Photonic crystals are periodic dielectric structures which exhibit strong Bragg-scattering as well as microscopic resonance scattering of electromagnetic waves. One good example is the opal structure assembled by micro spheres in an *fcc* lattice. Under suitable circumstances, e.g., the refractive index contrast between spheres is higher than a certain value, a forbidden frequency range, known as the photonic band gap (PBG), can develop in some direction. Within the PBG, propagation of electromagnetic radiation is forbidden along this direction. The concept of a complete PBG in photonic crystal was proposed independently by Yablonovitch for controlling spontaneous emission [52], and John for achieving photon localization [21] in 1987. The ability to tailor electromagnetic dispersion relations and the associated photonic mode structures in photonic crystals facilitates new approaches to low threshold micro-lasers [53, 54]. Actually, the study of electromagnetic wave propagation in periodic structures was studied a long time ago in one dimensional

systems, and mirrorless lasing with distributed feedback in such structures was proposed in the early 1970s [55, 56].

There has been tremendous study done on photonic crystals both experimentally and theoretically for the past two decades. Low threshold micro lasers made from such structures with gain has been a field of intense interest and effort. In general, there are two types of lasers associated with photonic crystals. The first is the *bandedge state laser*, in which the light emission occurs at the photonic band edge. The second is the *defect mode laser*, which utilizes a localized defect mode as a laser cavity. At a photonic band edge, strong coupling between light emitters and electromagnetic modes arises from small group velocity and high density of states. The slow group velocity makes the coupling time much longer and the high density of states makes the coupling more efficient. Mirrorless, low-threshold laser action at photonic band edges has been demonstrated for one-dimensional [57], two-dimensional [58], and three dimensional photonic crystals.

While the threshold can be low, bandedge state lasers are typically not confined spatially due to the feedback from all the photonic lattices. To achieve both low threshold and small mode volume, defect mode lasers are proposed. The spontaneous emission can be suppressed when the emission frequency falls within the photonic band gap. Thus, if a small defect is introduced in the photonic crystal (by adding extra material, or removing some of the dielectric material), a localized electromagnetic mode can be created within the structure at a frequency inside the gap. In this case, the spontaneous emission occurs preferentially into this localized mode, making it act as a micro-cavity with a very high

quality factor. Such single defect cavities are expected to realize nearly thresholdless lasers, and its volume is confined in the structure defect, which can be on the scale of  $\lambda^3$ . Laser action in a micro-cavity formed from a single defect in two dimensional photonic crystals has already been demonstrated [59].

The photonic crystal laser cavity with the highest quality factor is expected to be the defect mode laser in three dimensional photonic crystals where light is confined in all directions. However, the fabrication of three dimensional structures is very complicated, and introducing a well controlled defect into such a structure is very challenging as well. To meet the fabrication challenge, a hybrid structure, the *photonic crystal slab* (PhCS) is introduced. A photonic crystal slab is a slab with photonic crystal structures in plane, thus the light is confined in plane by PBG effect, while confinement in the vertical direction is realized by index guiding. Such structures can be fabricated easily due to the mature 2D fabrication techniques and both bandedge state lasers and defect mode lasers have been demonstrated in such structures.

### 1.3 Outline of This Thesis

This thesis includes experimental and numerical studies on lasing in random and periodic structures.

In Chapter 2, we study random lasing with resonant feedback from the weakly scattering colloidal laser dye solutions in detail. With a special cone shaped excitation geometry, we illustrate the difference between the quasimodes of the passive system and

lasing modes under spatially inhomogeneous gain. The study is extended to investigate the relation between quasimodes of a random structure and its lasing modes under both global and local excitations, which is performed numerically in two dimensional systems by using the finite difference time domain method and one dimensional systems by using the transfer matrix method. Both experimental and numerical studies reveal the similarity and difference between quasimodes and lasing modes, which successfully answer many important questions people have for random lasers in weakly scattering systems. Moreover, based on the same experiment, a systematic study on statistical properties of the random lasing peaks is conducted. Compared with the same measurement for amplified spontaneous emission spikes, we clarify the two distinct physical processes which share a similar discrete spiky single shot emission spectrum.

In Chapter 3, we utilize closely packed resonant scatterers to study lasing in strongly scattering random media. The active, monodisperse, resonant spherical scatterers are successfully synthesized by a two step chemical reaction process developed by us, and the multiple scattering random samples are prepared by closely packing the spheres with a cold press method. Scattering from a single sphere is calculated using Mie's theory, where the refractive index of the sphere is determined by the photonic band gap effect measurement on self-assembled opal structures. The scattering strength of the random samples is calibrated by coherent backscattering measurement, from which the transport mean free path is derived. The experimental result deviates from that predicted by Mie theory under the independent scattering approximation, and the discrepancy is

successfully explained by a dependent multiple Mie scattering simulation. Lasing from the random samples under optical excitation is measured, and the threshold is found to be closely related to the mean free path. The fluctuation of the lasing threshold is also measured and the result, as well as the average threshold behavior, is simulated by a polarization dependent finite difference time domain calculation.

In Chapter 4, we study ZnO photonic crystal slab lasers where three dimensional light confinement is achieved by the in-plane band gap effect and waveguiding in the vertical direction. We first design the structure with air cylinders in a triangular latticed with the dispersion relation calculation done using the plane wave expansion method. To overcome the vertical asymmetry presented in our samples, a supercell scheme is utilized and symmetry dependent mode selection is checked to provide the correct band structure. By varying the in-plane lattice constant, the air cylinder radius, and the ZnO slab thickness, we obtain the optimum structure parameters for the largest in-plane band gap overlapping with the ZnO spectral gain. This structure is successfully fabricated with a focused ion beam etching technique, and a single mode laser is realized at room temperature under optical excitation. Moreover, single mode lasers with frequencies across the whole spectral range of ZnO gain are obtained by fine-tuning the lattice constant. The lasing mode varies from sample to sample, which indicates the crucial role played by defects introduced during the fabrication procedure. The effect of disorder on photonic crystal lasers, both the defect mode laser and the bandedge state laser, is studied numerically. It is shown that the disorder tends to balance the vertical and lateral loss of a photonic

crystal slab laser, which may facilitate the lasing process.

Finally, in chapter 5, we present concluding remarks and possible future works which can be done based on current studies presented in this thesis.

## CHAPTER 2

# COHERENT RANDOM LASERS IN WEAKLY SCATTERING COLLOIDAL DYE SOLUTIONS

### 2.1 Motivation

Random lasers have attracted much interest and many studies over the past few years [32]. One important subject is the nature of random lasing modes, which was not fully understood. For random systems in or close to the localization regime, lasing oscillation occurs in the eigenmodes of Maxwell's equations (also called quasimodes for the open system) [60–62]. The formation of quasimodes or lasing modes relies on the interference of scattered waves which return to the same coherence volume via different *closed* paths. Thus scattering provides coherent (phase-sensitive) and resonant (frequency-dependent) feedback for lasing, leading to the selection of discrete lasing frequencies [38]. Surprisingly, random lasing with resonant feedback was also realized in diffusive or even ballistic systems, even though the coherent interference effect was expected to be negligibly small [40, 42, 49, 63]. The lasing modes were considered to be the quasimodes with small decay rates [50, 64–68]. However, recent theoretical studies suggested that the quasimodes of a passive random system may not be the genuine normal modes of the same system with gain [69, 70].

Another puzzle is that, experimentally, tight focusing of the pump beam is necessary to observe discrete lasing peaks [40,42]. In diffusive or ballistic systems, the quasimodes are spatially extended across the entire volume, thus they should all be excited more or less equally under local pumping. Shrinking the gain volume should not decrease the number of potential lasing modes, but only increase their lasing threshold. Such expectations contradicted the experimental observations. Several models were proposed to resolve this issue, for example, the rare anomalously localized modes [50] or the absorption-induced confinement of lasing modes in the pumped region [51]. The problem with the former is that the lasing modes are not as rare as expected, while the latter no longer applies when the absorption outside the pumped region is negligible.

In addition to the lasing peaks, sharp random spikes were observed in the single-shot spectra of amplified spontaneous emission (ASE) from colloidal solutions over a wide range of scattering strength [71]. The spikes were stochastic and varied from shot to shot. They were attributed to single spontaneous emission events which happened to take long *open* paths inside the amplifying random medium and picked up large gain. Thus the emergence of ASE spikes did not rely on resonant feedback or coherent interference. However, a clear distinction between the stochastic ASE spikes and coherent random laser modes is still missing.

We will attempt to answer the above questions by our experimental and numerical studies presented in this chapter.

## 2.2 Lasing Experiments in Colloidal Dye Solutions

We performed experiments on several weakly scattering systems which consisted of passive scatterers embedded in active homogeneous media. The scatterers included  $\text{TiO}_2$  particles of radius 200 nm,  $\text{ZnO}$  particles of radius 38 nm, and  $\text{SiO}_2$  particles of radius 220 nm. The nanoparticles were suspended in a laser dye solution—e.g., rhodamine 640 perchlorate, stilbene 420, or LDS 722 in diethylene glycol (DEG) or methanol. The experimental results obtained with different particles, dyes and solvents were qualitatively similar. As an example, we will demonstrate the lasing phenomena with colloidal suspensions of  $\text{TiO}_2$  particles in DEG with rhodamine 640.

A small amount of  $\text{TiO}_2$  (rutile) particles, with an average radius of 200 nm, were dissolved in the DEG solution of rhodamine 640 perchlorate dye. To prevent flocculation, the  $\text{TiO}_2$  particles were coated with a thin layer of  $\text{Al}_2\text{O}_3$ . DEG was chosen as the solvent instead of the widely used methanol because of the facts that (i) the windows of the quartz cuvette that contained the methanol solution were coated with a layer of  $\text{TiO}_2$  particles, whereas such coating was not observed for the DEG solution, and (ii) the viscosity of DEG was about 30 times larger than methanol; thus the sedimentation of  $\text{TiO}_2$  particles in DEG was much slower. In our experiment, the particle density  $\rho$  ranged from  $1.87 \times 10^8 \text{ cm}^{-3}$  to  $5.6 \times 10^{10} \text{ cm}^{-3}$ . The scattering mean free path was estimated by  $l_s = 1/\rho\sigma_s$ , where  $\sigma_s$  is the scattering cross section of a  $\text{TiO}_2$  spherical particle with radius 200 nm. The value of  $l_s$  varied from 1.07 cm to 35  $\mu\text{m}$ . The dye molarity  $M$  also changed from 3 to 10 mM. Right before the lasing experiment, the suspension was placed

in an ultrasonic bath for 30 min to prevent sedimentation of the particles. During the experiment, the solution was contained in a quartz cuvette that was 1.0 cm long, 1.0 cm wide, and 4.5 cm high. The dye molecules in the solution were optically pumped by the frequency-doubled output ( $\lambda_p = 532$  nm) of a mode-locked Nd:YAG laser (25 ps pulse width, 10 Hz repetition rate). The pump beam was focused by a lens into the solution through the front window of the cuvette. The radius of the pump spot at the entrance to the solution was about 20  $\mu\text{m}$ . The experimental setup is shown schematically in the inset of Fig. 2.1. The emission from the solution was collected in the backwards direction of the incident pump beam. A second lens focused the emission into a fiber bundle (FB) which was connected to the entrance slit of a spectrometer with a cooled CCD array detector. The spectral resolution was 0.6  $\text{\AA}$ .

We started the experiment with a sample of  $M = 5$  mM and  $\rho = 3.0 \times 10^9$   $\text{cm}^{-3}$ . At a low pumping level, the emission spectrum featured the broad spontaneous emission band of rhodamine 640 molecules. Above a threshold pump intensity, discrete narrow peaks emerged in the emission spectrum and their intensities grew rapidly with increased pumping. This behavior corresponded to the onset of lasing. The lasing peaks could be as narrow as 0.12 nm. Their frequencies changed from pulse to pulse (shot). We repeated the experiment with samples of different particle densities but the same dye concentration. Lasing was observed only within a certain range of particle density. Figure 1 shows the spectra of emission from five samples taken at the same incident pump pulse energy 0.4  $\mu\text{J}$ . Each spectrum was integrated over 25 shots. Only a relatively broad ASE peak was

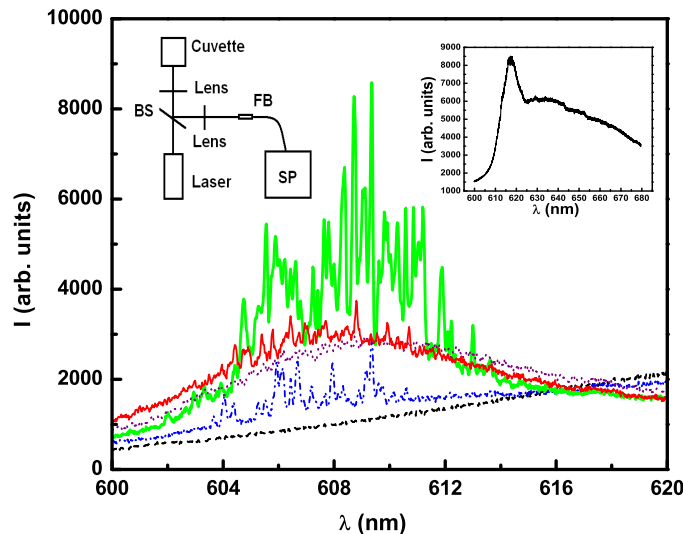


Figure 2.1: Spectra of emission from DEG solutions of Rhodamine 640 (5 mM) and  $\text{TiO}_2$  particles. The particle densities are (1)  $\rho = 0$  (dotted curve), (2)  $1.87 \times 10^8 \text{ cm}^{-3}$  (thin solid curve), (3)  $1.87 \times 10^9 \text{ cm}^{-3}$  (thick solid curve), (4)  $1.3 \times 10^{10} \text{ cm}^{-3}$  (dot-dot-dashed curve), (5)  $5.0 \times 10^{10} \text{ cm}^{-3}$  (dashed curve). All spectra were taken at the same pump pulse energy  $0.4 \mu\text{J}$ . Each spectrum was integrated over 25 shots. Left inset is our experimental setup, BS: beam splitter, SP: spectrometer, FB: fiber bundle. Right inset is the emission spectrum shows the ASE peak.  $\rho = 5.0 \times 10^{10} \text{ cm}^{-3}$ . The pump pulse energy is  $1.2 \mu\text{J}$ .

observed for the neat dye solution, whereas a few discrete lasing peaks emerged on top of the ASE spectrum at small particle concentration  $\rho = 1.87 \times 10^8 \text{ cm}^{-3}$ . Increasing the particle density to  $1.87 \times 10^9 \text{ cm}^{-3}$  led to an increase in the number of lasing peaks and the peak intensity. However, when  $\rho$  increased further to  $1.3 \times 10^{10} \text{ cm}^{-3}$ , the lasing emission started to decrease. Eventually at  $\rho = 5.0 \times 10^{10} \text{ cm}^{-3}$  lasing peaks disappeared. A further increase of the incident pump pulse energy to  $1.2 \mu\text{J}$  resulted in an ASE peak at a longer wavelength, shown in the right inset of Fig. 2.1. The redshift of the ASE peak might be caused by the surface effect on the emission frequency of rhodamine 640

molecules adsorbed on the TiO<sub>2</sub> particles. One support for this explanation was that the emission frequency was blueshifted when we replaced the TiO<sub>2</sub> particles by SiO<sub>2</sub> particles.

In Fig. 2.2, the incident pump pulse energy at the lasing threshold  $P_t$  is plotted against the particle density  $\rho$ . At the lasing threshold, the slope of the emission intensity versus pump pulse energy exhibited a sudden increase (inset of Fig. 2.2). At  $\rho = 3.8 \times 10^8 \text{ cm}^{-3}$ , lasing started at  $0.21 \mu\text{J}$ . As  $\rho$  increased to  $1.5 \times 10^9 \text{ cm}^{-3}$ ,  $P_t$  decreased gradually to  $0.12 \mu\text{J}$ . Then it remained nearly constant with a further increase of  $\rho$ . The threshold started to rise at  $\rho = 1.9 \times 10^{10} \text{ cm}^{-3}$ , then went up quickly with  $\rho$ . At  $\rho = 5.6 \times 10^{10} \text{ cm}^{-3}$ , no lasing peaks were observed up to the maximum pump pulse energy of  $2.0 \mu\text{J}$  we used, although at  $1.0 \mu\text{J}$  an ASE peak appeared at a longer wavelength.

The particles played an essential role in the lasing process in our suspensions because lasing did not happen in the neat dye solution. One possibility was lasing within individual particles that served as laser resonators. It contradicted two experimental observations: (i) the lasing threshold depended on the particle density (Fig. 2.2); (ii) the laser output was highly directional (shown next). The left inset of Fig. 2.3 is a sketch of our directionality measurement setup. A fiber bundle was placed at the focal plane of the lens. It was scanned with fine steps parallel to the focal plane. At each step, the spectrum of emission into a particular direction was recorded. The output angle  $\theta$  was computed from the fiber bundle position. Its range was limited by the diameter of the lens to about  $14^\circ$ .  $\theta = 0$  corresponded to the backward direction of the incident pump beam. In each

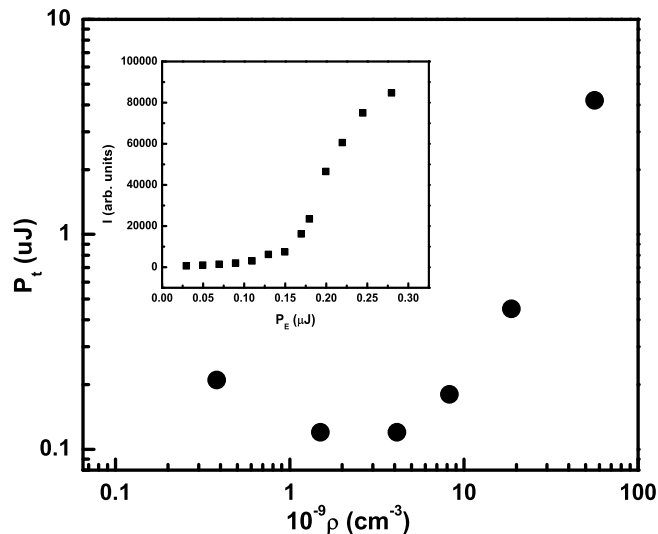


Figure 2.2: The threshold pump pulse energy  $P_t$  as a function of the  $\text{TiO}_2$  particle density  $\rho$ . The concentration of Rhodamine 640 in DEG is 5 mM. The inset is a plot of the emission intensity  $I$  versus the pump pulse energy  $P_E$  for the suspension with  $\rho = 3.0 \times 10^9 \text{ cm}^{-3}$ .

spectrum, the emission intensity was integrated over the wavelength range of 604-612 nm in which the lasing peaks were located. Figure 2.3 is a plot of the integrated emission intensity versus the output angle  $\theta$  at  $\rho = 3.0 \times 10^9 \text{ cm}^{-3}$ . Although the spontaneous emission at low pumping was isotropic, the lasing emission was strongly confined to the backward direction of the incident pump beam. The divergence angle  $\Delta\theta$  of the output laser beam was merely  $4^\circ$ . To check the effect of reflection by the front window of the cuvette on lasing, we rotated the cuvette around the vertical axis and repeated the measurement. As shown in the right inset of Fig. 2.3,  $\phi$  represented the angle between the incident pump beam and the normal of the front window. Similar lasing phenomena were observed except for a small increase of the lasing threshold. The lasing emission

was always confined to the backward direction of the pump beam even when  $\phi$  was much larger than the divergence angle of the focused pump beam, which was about  $4^\circ$ . This result demonstrated that the front window of the cuvette was not indispensable to the lasing process. Figure 3 also shows the angular distribution of ASE from a sample of higher particle density ( $\rho = 5 \times 10^{10} \text{ cm}^{-3}$ ). The integrated intensity of ASE (at longer wavelength) was nearly constant over the angular range of detection. To understand

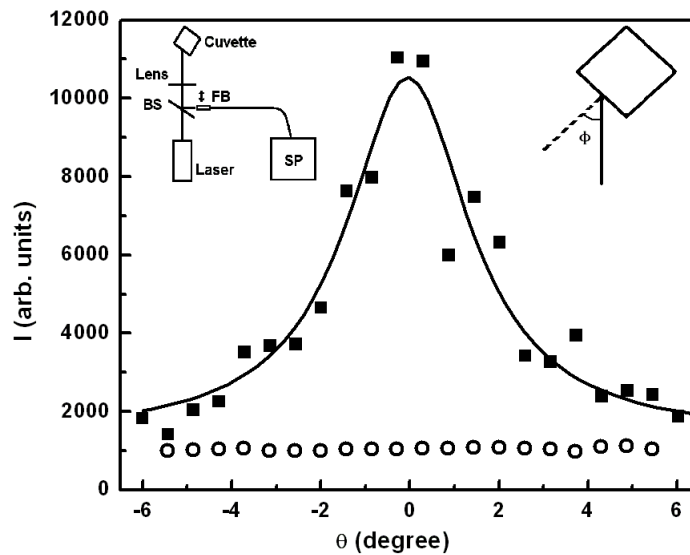


Figure 2.3: The angular distribution of output emission intensity from DEG solutions of 5 mM Rhodamine 640 and  $3.0 \times 10^9 \text{ cm}^{-3}$  (solid square) or  $5.0 \times 10^{10} \text{ cm}^{-3}$  (open circle)  $\text{TiO}_2$  particles. The solid line is a Gaussian fit of output laser beam.  $\theta = 0$  corresponds to the backward direction of pump beam. Left inset is a sketch of experimental setup, BS: beam splitter, SP: spectrometer, FB: fiber bundle. Right inset shows the angle  $\phi$  between the pump beam and the normal to the front window of the cuvette.

the directionality of lasing emission from the dilute suspension, the pumped region was imaged through a side window of the cuvette. The measurement setup is sketched in the inset of Fig. 2.4(a). Emission from the excited region was collected through the side

window by a  $5\times$  objective lens and imaged onto a CCD camera by integrating multiple pulses. The spectrum was taken simultaneously by partitioning the signal with a beam splitter (BS). Figure 2.4(a) compares the spectrum of emission through the side window to that through the front window of the cuvette from the same sample ( $\rho = 3 \times 10^9 \text{ cm}^{-3}$ ,  $M = 5 \text{ mM}$ ) under identical pumping conditions. The spectrum of emission from the front window exhibited large lasing peaks. However, only spontaneous emission was observed through the side window, and it shifted to longer wavelength as a result of reabsorption in the unpumped solution between the excited region and side window. To calibrate the reabsorption, we measured the spontaneous emission spectra at low pump intensity from both front and side windows. The magnitude of reabsorption was estimated from the intensity ratio of emission through the side window to that through the front. Based on this estimation, we concluded that the reabsorption was not strong enough to make the lasing peaks, which emerged in the front emission spectrum at high pump intensity, disappear in the side emission spectrum. This conclusion confirmed the result of the lasing directionality measurement in Fig. 2.3. More importantly, the image of spontaneous emission intensity distribution taken through the side window exhibited the shape of the excited region in the sample. As shown in Fig. 2.4(b), the excited volume at low particle density had a cone shape. The length of the cone was much larger than its base diameter. Unfortunately, we could not get the exact length of the cone from the image, because near its end the spontaneous emission was too weak to be recorded by the CCD camera. At high particle density, the shape of excited volume changed to a

hemisphere as shown in Fig. 2.4(c) at a higher pumping power. This change was caused by increased scattering of pump light. In Fig. 2.4(b),  $\rho = 3.0 \times 10^9 \text{ cm}^{-3}$ ; the scattering mean free path  $l_s$  at the pump wavelength  $\lambda_p = 532 \text{ nm}$  was estimated to be  $800 \mu\text{m}$ . The (linear) absorption length  $l_a$ , obtained from the transmission measurement of the neat dye solution, was about  $50 \mu\text{m}$  at  $\lambda_p = 532 \text{ nm}$ . Strong pumping in the lasing experiment could saturate the absorption of dye molecules, leading to an increase of  $l_a$ . Since the shape of the excited volume shown in Fig. 2.4(b) was nearly identical to that in the neat dye solution, the scattering of pump light must be much weaker than absorption; i.e.,  $l_a$  was still shorter than  $l_s$ . In Fig. 2.4(c),  $\rho = 5.0 \times 10^{10} \text{ cm}^{-3}$ ;  $l_s$  was shortened to  $53 \mu\text{m}$ . Scattering of pump light became much stronger. As a result of multiple scattering, the cone was replaced by a hemisphere. The image of excited volume provided some clue to the high directionality of lasing emission at small  $\rho$  and nondirectionality of ASE at large  $\rho$  in Fig. 2.3. At low particle density, stimulated emission in the cone-shaped gain volume was the strongest along the cone due to the longest path length. Since the cone was parallel to the incident pump beam, lasing was confined to the direction parallel to the pump beam. The divergence angle  $\Delta\theta$  of laser output was determined by the aspect ratio of the excited cone: namely,  $\Delta\theta \sim 2r_p/L_p$ , where  $L_p$  is the cone length and  $r_p$  is the base radius. At large  $\rho$ , emitted photons experienced multiple scattering while being amplified in the hemisphere-shaped gain volume. Hence, the ASE was nearly isotropic.

Therefore, the shape of the gain volume determined the lasing directionality; i.e., lasing occurred along the direction in which the gain volume was most extended. However,

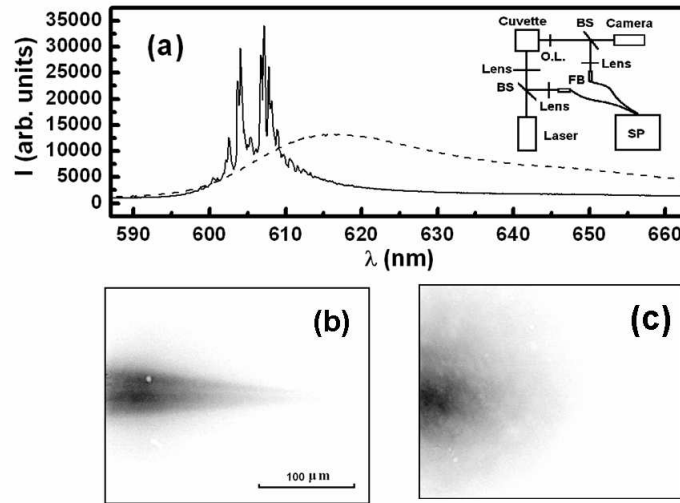


Figure 2.4: (a): Spectra of emission through the side window (dashed curve) and front window (solid curve) of the cuvette. The inset is a sketch of the experimental setup, BS: beam splitter, SP: spectrometer, FB: fiber bundle. (b): Side image of excited region in DEG solution of 5 mM Rhodamine 640 and  $3.0 \times 10^9 \text{ cm}^{-3}$   $\text{TiO}_2$  particles. The pump pulse energy is  $0.2 \mu\text{J}$ . (c): Side image of excited region in DEG solution of 5 mM Rhodamine 640 and  $5.0 \times 10^{10} \text{ cm}^{-3}$   $\text{TiO}_2$  particles. The pump pulse energy is  $1.2 \mu\text{J}$ .

it was still not clear how the laser cavities were formed in the dilute suspension. We examined the lasing spectra more carefully by taking single-shot emission spectra with the setup shown in the inset of Fig. 2.1. Surprisingly, in most single-shot spectra the spectral spacing of the lasing peaks was close to a constant. Figure 2.5(a) is an example of a single-shot emission spectrum taken from the sample of  $\rho = 1.87 \times 10^9 \text{ cm}^{-3}$  and  $M = 5 \text{ mM}$ . The spectral correlation function  $C(d\lambda) \equiv \langle I(\lambda)I(\lambda + d\lambda) \rangle / \langle I(\lambda)^2 \rangle$  was computed for the spectrum in Fig. 2.5(a) and plotted in Fig. 2.5(b). The almost regularly spaced correlation peaks revealed the periodicity of lasing peaks. Despite the fact that the lasing peaks completely changed from shot to shot, the peak spacing was nearly the same. In the spectrum taken over many shots, the periodicity was smeared out due to random

(uncorrelated) peak positions in different shots. As an example, in Fig. 1 the solid thick curve represents the lasing spectrum integrated over 25 pulses and the lasing peaks did not exhibit clear periodicity. We also noticed that the periodicity was less obvious at higher particle density. We would like to point out that the lasing peaks in the dilute

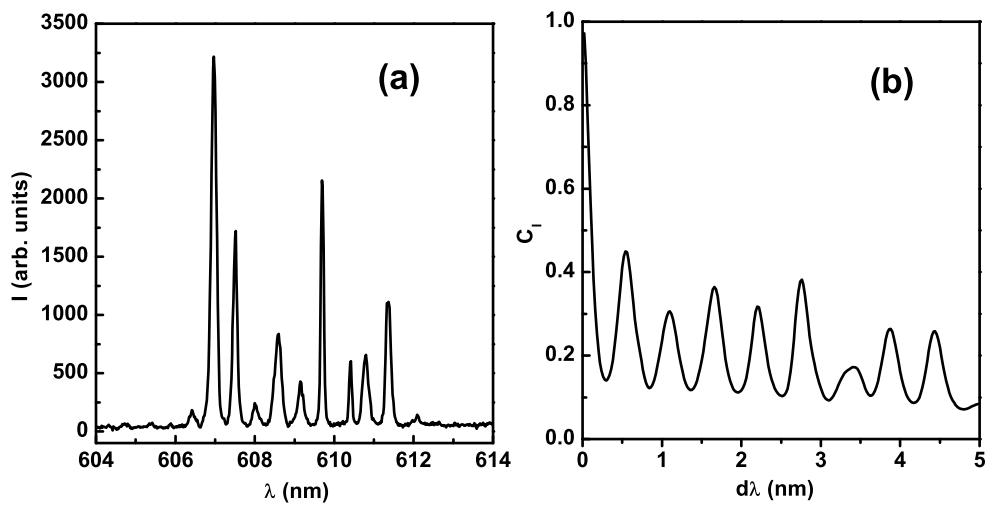


Figure 2.5: (a): A single shot emission spectrum from DEG solution of 5 mM Rhodamine 640 and  $1.87 \times 10^9 \text{ cm}^{-3}$   $\text{TiO}_2$  particles. The pump pulse energy is  $0.2 \mu\text{J}$  pumping. (b): Spectral correlation function computed for the spectrum in (a).

suspension of particles are fundamentally different from the stochastic ASE spikes that could be observed also in the neat dye solution. Figure 2.6 shows a single-shot spectrum of emission from the DEG solution of 5 mM rhodamine 640 without any particles. The spectrum was taken under the same condition as that in Fig. 2.5. At a high pumping level, stochastic spikes appeared on top of the ASE peak. The spikes in Fig. 2.6 were denser and narrower than the lasing peaks in Fig. 2.5. They changed constantly from

shot to shot. When integrating the spectrum over subsequent shots, the spikes were quickly averaged out, leaving a smooth ASE spectrum, shown as the dotted curve in Fig. 2.1. Note that the stochastic spikes also appeared in the spectrum of emission from the dye solutions with particles. However, they were taken over by the huge lasing peaks at high pumping level. The stochastic structure of the pulsed ASE spectrum was first reported 30 years ago [72, 73]. Since then, there have been detailed experimental and theoretical studies of this phenomenon [74–77]. The spectral fluctuation originated from random spontaneous emission, which was strongly amplified as it propagated through the cone-shaped pump volume. Nonstationary interference of the partially coherent ASE not only presented a grainy spatial pattern, but also caused drastic temporal fluctuations of the intensity. The random intensity fluctuation within an ASE pulse in the time domain generated stochastic spikes in the spectral domain. According to the Fourier transformation, the width of spectral spikes was inversely proportional to the ASE pulse duration. In our case of picosecond pumping, the ASE pulse duration was of the order 25 ps. Thus the average spike width should be  $\sim 0.05$  nm, which was close to the measured value of 0.07 nm. To find out the location and size of the laser cavities in the dilute suspension, we placed a metallic rod in between the excited volume and the back window (inset of Fig. 2.7). On the one hand, the rod prevented the emission from being reflected by the back window into the gain volume. On the other hand, a Fabry-Perot cavity was formed. Lasing in this cavity produced equally spaced peaks in the emission spectrum. The peak spacing  $\Delta\lambda$  was determined by the cavity length  $d$  (the distance between the rod and the

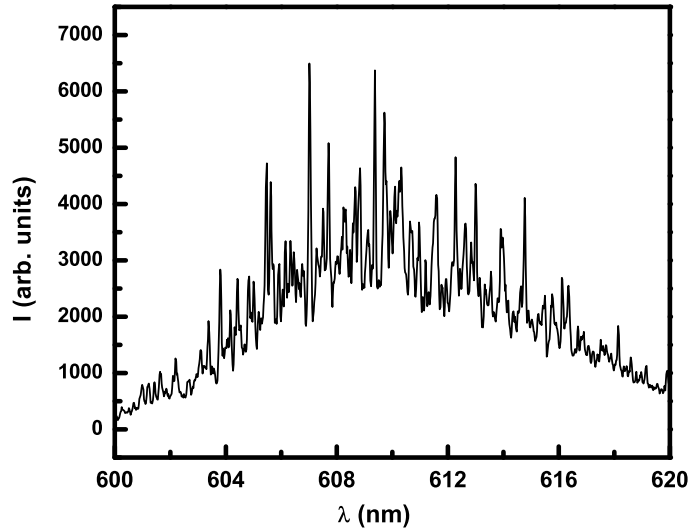


Figure 2.6: A single shot emission spectrum from the DEG solution of 5 mM Rhodamine 640 without any particles. The pump pulse energy is  $0.3 \mu\text{J}$  pumping.

front window),  $\Delta\lambda = \lambda^2/2n_e d$ , where  $n_e$  is the effective index of suspension. As plotted in Fig. 2.7,  $\Delta\lambda$  decreased with increasing  $d$ . However, when  $d$  exceeded a critical value  $d_0 \simeq 450 \mu\text{m}$ ,  $\Delta\lambda$  jumped to a constant value and did not change with  $d$  anymore (Fig. 2.7). The lasing spectrum and peak spacing at  $d > d_0$  were identical to those from the same sample without the metallic rod. This result demonstrated that the laser cavity in the colloidal solution was located within  $450 \mu\text{m}$  from the front window—i.e., in the vicinity of excited cone. Despite the scattering mean free path  $l_s$  ( $\sim 800 \mu\text{m}$ ) being much longer than the wavelength, the laser cavity was not extended over the entire sample, but confined to a region of dimension less than  $l_s$ . This could be explained by the reabsorption of laser emission in the unpumped part of sample. Our white-light absorption measurement and photoluminescence measurement of the neat dye solution showed that

rhodamine 640 molecules in DEG had significant overlap between the absorption band and emission band. At the dye concentration  $M = 5$  mM, the absorption length  $l_e$  at the emission wavelength  $\lambda_e \sim 610$  nm was about  $300 \mu\text{m}$ . At low density of  $\text{TiO}_2$  particles in the solution, the absorption length of emitted photons in the unpumped region was shorter than the scattering length. If the emitted light traveled beyond one absorption length from the pumped region, its chance of returning to the pumped region was extremely low. Therefore, the reabsorption of emission suppressed the feedback from the unpumped region of the system and effectively reduced the system (or cavity) size [51].

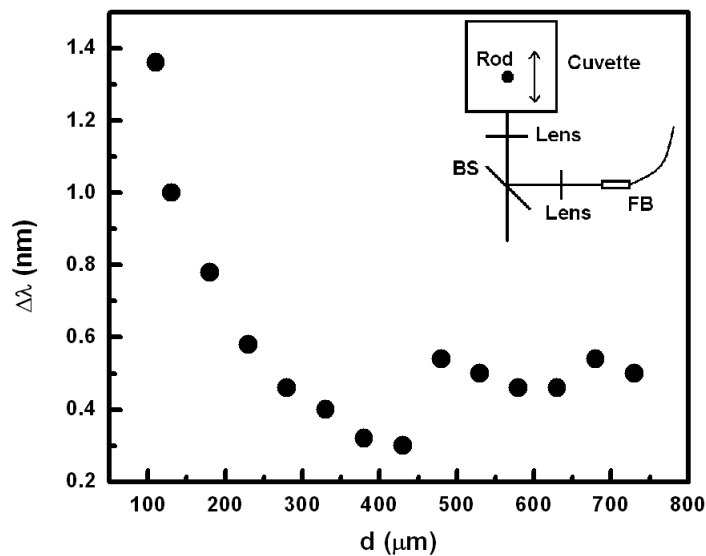


Figure 2.7: The wavelength spacing  $\Delta\lambda$  of lasing modes as a function of the distance  $d$  between the metallic rod and the cuvette front window. The concentration of Rhodamine 640 in DEG is 5 mM, and the  $\text{TiO}_2$  particle density is  $3.0 \times 10^9 \text{ cm}^{-3}$ . The pump pulse energy is  $0.2 \mu\text{J}$ . The inset is a sketch of experimental setup. BS: beam splitter, FB: fiber bundle.

The above experiment illustrated that the laser cavity was confined in the vicinity of

the excited region. The directionality of laser output suggested that the laser cavity was oriented along the excited cone. The nearly constant spectral spacing of lasing modes resembled that of a Fabry-Perot cavity. Using the formula of a Fabry-Perot cavity, we derived the cavity length  $L_c$  from the average wavelength spacing  $\Delta\lambda$  of the lasing peaks,  $L_c = \lambda^2/2n_e\Delta\lambda \sim 200 - 300 \mu\text{m}$ . The estimated cavity length was close to the length of the excited cone observed from the side images. The cone length was determined by the penetration depth  $L_p$  of pump light into the suspension. When the scattering mean free path  $l_s$  was much larger than the absorption length at the pump wavelength,  $L_p$  was determined solely by absorption of pump light. This could explain the experimental observation that the averaging spacing of lasing peaks barely changed when the scattering mean free path  $l_s$  was varied by more than one order of magnitude. The cavity length  $L_c$  (or the penetration depth  $L_p$ ) did not depend on  $l_s$  as long as  $l_s$  exceeded the absorption length. This result was confirmed by the side images of excited cones.

In the case of linear absorption,  $L_p$  should be on the order of the (linear) absorption length  $l_a$ . However, the pumping in the lasing experiment was so intense that it saturated the absorption of dye molecules. The saturation photon flux density  $I_s = 1/\sigma_f\tau_f$ , where  $\sigma_f$  is the fluorescence cross section and  $\tau_f$  is the lifetime of dye molecules in the excited state. For rhodamine 640 molecules,  $\sigma_f$  is of the order  $10^{-16} \text{ cm}^2$  and  $\tau_f$  of the order of  $10^{-9} \text{ s}$ . Thus,  $I_s \sim 10^{25} \text{ cm}^{-2}\text{s}^{-1}$ . The typical pump pulse energy at the lasing threshold was  $\sim 0.1 \mu\text{J}$ . From the pump pulse duration and pump spot size, we estimated that the incident pump photon flux density  $I_p \sim 10^{27} \text{ cm}^{-2}\text{s}^{-1}$ , which was two orders of

magnitude higher than  $I_s$ . Hence, at the lasing threshold the absorption of dye molecules near the front window of the cuvette was strongly saturated, and the penetration depth  $L_p$  was much longer than the linear absorption length  $l_a$ .

To confirm  $L_c \sim L_p$ , we changed  $L_p$  by varying the dye concentration. The higher the dye concentration, the shorter the penetration depth. If  $L_c \sim L_p$ , the spacing of lasing peaks  $\Delta\lambda$  should increase. Figure 2.8(a) shows the single-shot lasing spectra from three solutions of  $M = 3, 5, 10$  mM. The particle density  $\rho$  was fixed at  $3 \times 10^9 \text{ cm}^{-3}$ . It was evident that the spacing of lasing peaks increased at higher dye concentration. Images of the excited cones in the inset of Fig. 2.8(b) directly show that the excited cone was longer in the solution of lower dye concentration. Figure 2.8(b) plots the spectral correlation functions for the three spectra in Fig. 2.8(a). From them we extracted the average wavelength spacing  $\Delta\lambda = 0.34, 0.48, 0.96$  nm for  $M = 3, 5, 10$  mM. This result confirmed that the laser cavity length was determined by the pump penetration depth. Hence, the laser cavity was located in the excited cone and the cavity length was approximately equal to the cone length.

Although the lasing phenomenon in the weakly scattering dye solution seemed to resemble that in a Fabry-Perot cavity with the “mirrors” at the tip and base of the excited cone, the question remained as to what made the mirrors in the dilute colloidal suspension. The experiments presented earlier in this section already ruled out the front and back windows of the cuvette as the mirrors. The mirrors could not be formed by the nonlinear change of refractive index (both its real and imaginary parts) of the dye

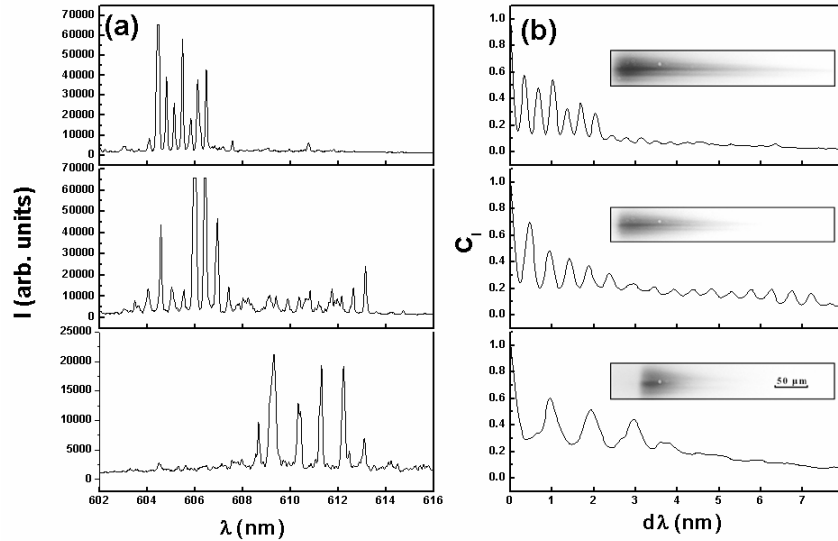


Figure 2.8: (a): Single shot emission spectra from colloidal solution of  $3.0 \times 10^9 \text{ cm}^{-3}$   $\text{TiO}_2$  particles. The molarity of Rhodamine 640 in DEG is (from top to bottom) 3 mM, 5 mM, and 10 mM. (b) Spectral correlation functions of the single shot emission spectra in (a). Insets are side images of pumped region for in each solution.

solution under intense pumping; otherwise, lasing would have occurred also in the neat dye solution without particles. Another possibility is that the particles aggregated in the solution to form large clusters that served as mirrors. We monitored the solution during the experiment by imaging it onto a CCD camera through a side window of the cuvette. No clusters of size larger than  $1 \mu\text{m}$  were observed in the pumped solution. We removed the clusters smaller than  $1 \mu\text{m}$  by filtering the solution. After the filtering, the lasing phenomena remained the same. We also tried other suspensions such as ZnO in DEG and  $\text{SiO}_2$  in methanol. Our previous studies confirmed the absence of particle aggregation in these suspensions, but we still observed a similar lasing phenomenon. Therefore, the “mirrors” were not clusters of particles. Another candidate was bubbles or shock

waves that were generated by the pump pulse [78–80]. We indeed observed bubbles in the solution when the pump beam was very strong and its focal spot was close to the front window of the cuvette. When the bubbles were large enough to be seen with our imaging apparatus, the lasing peaks disappeared. Hence, large bubbles did not facilitate lasing. Small bubbles, which were invisible, might be generated when the pumping was not very high. Such bubbles were usually generated at the focal spot of the pump beam where the pump intensity was the highest. Thus bubble formation should be sensitive to the distance between the focal spot and the front window, which affected the pump intensity at the focal spot due to absorption in the solution. When we shifted the focal spot by moving the lens, the lasing behavior remained the same. This result eliminated the possibility of small bubbles contributing to lasing. All the experimental results led us to the conclusion that the coherent feedback for lasing came from the particles in the solution—more specifically, from the particles located near the tip and base of the excited cone. However, there were many particles inside the pumped volume; e.g., at  $\rho = 3 \times 10^9 \text{ cm}^{-3}$  the number of particles inside the excited cone was about 400. Why did the feedback from the particles near the two ends of the cone dominate over that from the particles inside the cone? To understand this phenomenon, we performed numerical calculations, to be presented in the next section.

Our experimental studies demonstrated lasing with field feedback in weakly scattering samples. The focused pump beam created a cone-shaped gain volume in the dye solution containing a small amount of nanoparticles. The cone length was determined by the

absorption of dye molecules since optical scattering was much weaker than absorption. When the scattering mean free path exceeded the size of gain volume, lasing oscillation built up in the direction of strongest amplification—i.e., the direction in which the gain volume was most extended. This behavior was similar to that of amplified spontaneous emission in the weakly scattering regime [81]. The fundamental difference from ASE was, however, the existence of feedback that originated from the backscattered light. As pointed out by Krasad *et al* [82], the statistically rare sub-mean-free-path scattering could be made effective by strong amplification. In our experiment, the extreme weakness of feedback was compensated by high optical gain due to intense pumping. The interference of the backscattered light was greatly enhanced, leading to coherent and resonant feedback for lasing.

It is also important to note that the discrete lasing peaks were distinct from the stochastic ASE spikes. The latter originated from random spontaneous emission, which was significantly amplified in the presence of large gain. Such spectral fluctuations also existed in ASE from the homogeneous media (without scattering). Hence, scattering was not indispensable to the existence of ASE spikes, although the fluctuations could be enhanced by scattering which stretched the path length of photons inside the gain volume. In contrast, the presence of scatterers in the gain media was essential to the emergence of lasing peaks, indicating that the lasing process relied on the feedback supplied by scattering. This difference will be studied in more details in another future section.

## 2.3 FDTD Simulation of Random Lasing in 2D Weakly Scattering Systems

Several models were set up in the theoretical studies of the stimulated emission in active random media—e.g., the diffusion equation with gain [83,84] and the Monte Carlo simulation [71,85]. These models calculated the light intensity instead of the electromagnetic field; thus, they ignored the interference effect. Although it is usually weak in the diffusive regime, the interference effect is not always negligible. One example is coherent backscattering; namely, the interference between the counterpropagating light enhances the backscattered intensity by a factor of 2. The experimental results in the last section illustrated that the interference effect was significant in weakly scattering samples with gain, leading to lasing with resonant feedback. In the dilute suspensions of particles in which lasing could be realized, the gain volume had a cone shape and the cone length was shorter than the scattering mean free path. If we considered only one photon, it most likely would not be scattered as it traveled from one end of the cone to the other. However, the intense pumping generated a huge number of emitted photons. Despite the low probability of *one* photon being scattered, a significant number of emitted photons were scattered by the particles in the excited cone. Some of them were scattered backwards, providing feedback for lasing along the cone. Such weak feedback was greatly amplified as the backscattered light propagated along the cone. The interference of the backscattered light determined the lasing frequencies.

Therefore, in the presence of large gain, the interference of scattered light is not neg-

ligible even in weakly scattering samples. To include the interference effect, we directly calculated the electromagnetic field in a random medium by solving Maxwell's equations using the finite-difference time-domain (FDTD) method [86]. The optical gain was modeled as a negative conductance

$$\sigma(\omega) = -\frac{\sigma_0/2}{1 + i(\omega - \omega_0)T_2} - \frac{\sigma_0/2}{1 + i(\omega + \omega_0)T_2}. \quad (2.1)$$

$\sigma_0$  determines the gain magnitude, and  $\omega_0$  and  $1/T_2$  represents the center frequency and width of the gain spectrum, respectively. We neglected the gain saturation and limited our calculations to the regime just above the lasing threshold. A seed pulse with broad spectrum was launched at  $t = 0$  to initiate the amplification process. The lasing threshold was defined by the minimum gain coefficient ( $\sigma_0$ ) at which the electromagnetic field oscillation built up in time.

Our numerical calculations aimed not at reproducing the experimental results, but at addressing the key issues and providing physical insight into the lasing mechanism. Hence, we simulated lasing in two-dimensional systems in order to shorten the computing time. To model the elongated gain volume in the experiment, optical gain was introduced to a strip of length  $L_p$  and width  $W_p$ . The refractive index was set at 1.0 both inside and outside the strip. Dielectric cylinders of radius 100 nm and refractive index 2.0 were introduced as scattering centers. The strip dimension was much smaller than the experimental value due to the limited computing power. Consequently, the number of cylinders inside the strip was reduced to keep the system in the weak scattering regime.

The experimental results in the last section suggested that the coherent feedback for lasing resulted mainly from the particles located near the tip and base of the excited cone. In the dilute suspension of particles, there was probably only one particle located at the tip of the cone. One question was whether the backscattering of a single particle could provide enough feedback for lasing. To answer this question, we started with only two particles in the gain strip, one at each end, in the numerical simulation. The total system size was  $16 \mu\text{m} \times 8 \mu\text{m}$  and the gain strip  $8 \mu\text{m} \times 4 \mu\text{m}$ . At the system boundary, there was a perfectly matched absorbing layer. Two cylinders of radius 100 nm, placed at the two ends of the gain strip, had a separation of  $8 \mu\text{m}$ . When the gain coefficient  $\sigma_0$  was above a threshold value, we observed lasing oscillation. The spatial distribution of the lasing intensity revealed that lasing occurred along the strip with the feedback from the two particles. The emission spectrum, obtained by Fourier transform of the electric field, consisted of multiple lasing modes equally spaced in frequency. We repeated the calculation after reducing the separation between the two particles inside the gain strip while keeping the strip length constant. The frequency spacing of lasing modes scaled inversely with particle distance. These results confirmed lasing in the resonator composed of only two scatterers.

In 1998, Wilhelmi proposed a laser composed of two Rayleigh scatterers with gain medium in between [87]. We generalized the Rayleigh scatterers to Mie scatterers and

derived the lasing threshold condition

$$\frac{\sigma_b}{L_c^{m-1}} e^{g_e L_c} = 1. \quad (2.2)$$

$\sigma_b$  is the backscattering cross section of one particle, which depends on the particle size, refractive index, and light wavelength. The cavity length  $L_c$  is the separation between the two scatterers.  $m$  is the dimensionality of the scattering system.  $g_e$  is the threshold gain coefficient for lasing.  $\sigma_b/L_c^{m-1}$  describes the probability of a photon being backscattered by one particle and propagating to the other particle. The larger the  $L_c$ , the less percentage of the backscattered photons can reach the other particle. It seems to suggest that the quality factor of the two-particle cavity decreases with increasing  $L_c$ . This perception is incorrect. At the lasing threshold, the cavity loss is equal to the gain—namely, the loss per unit length  $\alpha = g_e$ . In the absence of intracavity absorption,  $\alpha$  is related to the cold cavity  $Q$  as  $\alpha = 1/Q\lambda$ . From the threshold gain coefficient  $g_e$  in Eq.(2.2), we derive the cold-cavity quality factor  $Q = L_c/(\lambda|(m-1)\ln L_c - \ln \sigma_b|)$ . As  $L_c \rightarrow \infty$ , the numerator in the expression of  $Q$  diverges faster than the denominator, thus  $Q \rightarrow \infty$ . The rise of  $Q$  with  $L_c$  is attributed to the increase of one path length of light inside the cavity. The reduction in the probability of photons backscattered by one particle then reaching the other particle in a long cavity is offset by the increase of photon travel time from one particle to the other. Hence, the lasing threshold decreases with increasing  $L_c$ . The resonator with the lowest lasing threshold is composed of two particles with the largest possible separation inside the gain volume.

Our numerical simulations also demonstrated directional lasing output from the two-scatterer cavity. The near-field to far-field transformation of the electric field gave the output laser intensity as a function of polar angle. Figure 2.9 shows the numerical data for three gain strips of length  $L_p = 4, 8, 16 \mu\text{m}$ . The strip width  $W_p$  was fixed at  $4 \mu\text{m}$ . The two scatterers were always placed at the ends of the strip. From the envelop of the far-field intensity distribution, we obtained the angular width of the output laser beam. It decreased as the aspect ratio of the gain strip,  $L_p/W_p$ , increased. Similar results were obtained when we varied  $W_p$  and kept  $L_p$  constant. These results indicated that the output from a two-particle cavity laser cannot be simply regarded as scattering of a plane wave by a single particle even if  $L_c \gg \lambda$ . It relied on both the geometry of the scatterers and the shape of the gain region. The directionality of the lasing output is a consequence of gain guiding.

Although in the dilute suspension of particles there was probably only one particle at the tip of the excited cone, there were more particles at the cone base whose dimension exceeded the average distance between the particles. For example, when the particle density  $\rho = 5 \times 10^8 \text{ cm}^{-3}$  and pump spot radius  $\sim 20 \mu\text{m}$ , there were typically ten particles near the base of the excited cone. To simulate this situation, we placed ten scatterers randomly near one end of the gain strip and only one scatterer at the other end. The lasing peaks were almost equally spaced in frequency, with the spacing close to that with only two scatterers in the strip, one on either end. It suggested that the feedback from the ten scatterers near one end of the gain strip was equivalent to that from

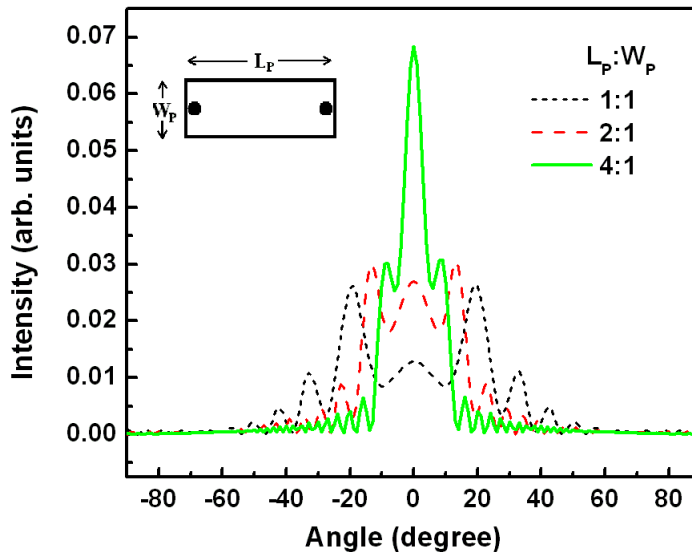


Figure 2.9: Far-field intensity of laser emission as a function of polar angle. The zero degree corresponds to the direction parallel to the gain strip. The width of gain strip  $W_p$  was fixed at  $4 \mu\text{m}$ . The strip length  $L_p = 4 \mu\text{m}$  (dotted curve),  $8 \mu\text{m}$  (dashed curve), and  $16 \mu\text{m}$  (solid curve). The inset is a sketch of the geometry of the 2D system in our numerical simulation. Two cylinders of radius  $100 \text{ nm}$  are located on both ends of the gain strip.

one located somewhere close to this end, as far as the lasing frequencies were concerned.

One question we raised at the end of the previous section is why the feedback from the particles near the two ends of the excited cone dominated over that from the particles inside the cone. One possible explanation would be that light backscattered by the particles near one end of the cone experienced the most amplification as it traveled the longest path within the gain volume to the other end of the cone. If this were the reason, it implied that the lasing modes would differ from the quasimodes of the passive system (without gain or loss). To check this conjecture, we randomly placed four cylinders inside the gain strip ( $8 \mu\text{m} \times 4 \mu\text{m}$ ) in addition to the two at the ends and compared

the lasing modes to the quasimodes of the passive system. The quasimodes were calculated with the multipole method [88, 89]. The field around each cylinder was expanded in a Fourier-Bessel series of regular and outgoing cylindrical harmonic functions. The Rayleigh identity related the regular part of the field at a particular cylinder to the waves sourced at all other scatterers. We found the quasimodes by searching in the complex wavelength plane for the poles of the scattering operator.

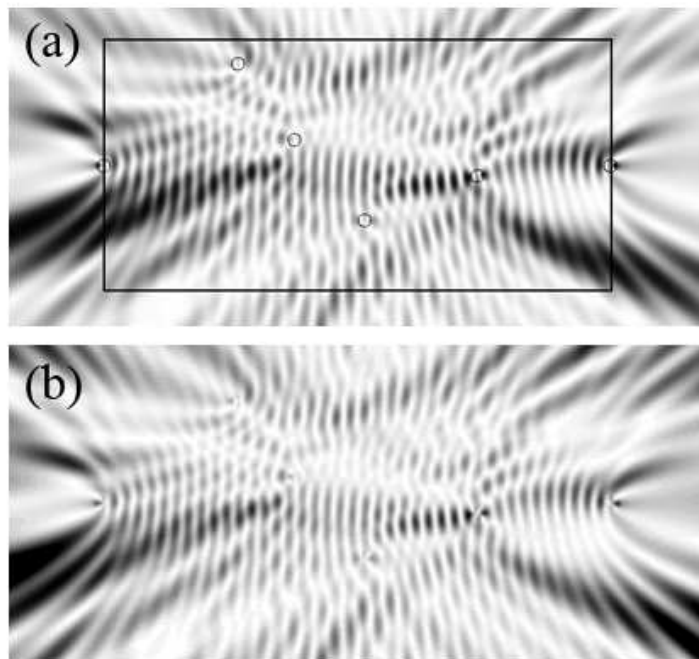


Figure 2.10: (a) Spatial intensity distribution of a lasing mode at  $\nu = 764.9$  THz in the 2D system of six dielectric cylinders inside a gain strip  $8 \mu\text{m} \times 4 \mu\text{m}$ . The circles represent the cylinders. The rectangle marks the boundary of the gain strip. (b) Spatial intensity distribution of quasimode at  $\nu = 764.5$  THz in the same system as (a) but without gain.

Our calculations revealed that despite the presence of additional scatterers, lasing still occurred in the direction parallel to the strip. Moreover, the lasing modes corresponded to the quasimodes with the quality factor relatively high among all the quasimodes within

6-particle lasing $\nu$	6-particle quasimode $\nu$	6-particle quasimode $Q$	2-particle quasimode $\nu$	2-particle quasimode $Q$
715.6	712.1	28.6	712.4	27.2
	736.6	18.7	730.5	28.2
744.0	742.2	31.0	748.5	29.3
764.9	764.5	29.4	766.5	30.5
782.9	785.1	37.7	784.1	31.8
806.9	811.7	38.5	801.7	32.8

Table 2.1: Frequencies  $\nu$  (THz) and quality factors  $Q$  of lasing modes and quasimodes.

the gain spectrum. Table 2.1 lists the frequencies  $\nu$  and quality factors  $Q$  of several lasing modes and the corresponding quasimodes. The gain spectrum was centered at 750 THz with a width of about 281 THz. The slight frequency shift of the lasing modes with respect to the quasimodes was due to the gain pulling effect. Figure 2.10 shows the intensity distributions of the lasing mode with  $\nu = 764.9$  THz and the quasimode with  $\nu = 764.5$  THz. It is evident that the lasing-mode profile within the gain strip is nearly identical to that of the quasimode. We checked several lasing modes and obtained the same result. Therefore, the lasing modes were almost the same as the quasimodes in the presence of uniform gain. In Table 2.1, we also list the frequencies and quality factors of the quasimodes in the two-particle case (without the four particles in the middle). The majority of the quasimodes in the system of six particles have frequencies similar to those of two particles. This comparison suggests in the weakly scattering system most quasimodes with relatively high  $Q$  are formed mainly by the feedback from the particles near the system boundary. The feedback from the particles in the interior of the system may slightly increase the quality factor or shift the mode frequency (see, e.g., the mode at  $\nu = 742.2$  THz). However, the feedback from these particles may also be

destructive and reduce the quality factor. As a result, the mode at  $\nu = 736.6$  THz would not lase. Because most quasimodes with relatively high  $Q$  have frequencies similar to those with only the two particles farthest apart, they, as well as the lasing modes, tend to be equally spaced in frequency. In the numerical simulation we did not place the particles outside the gain strip, because experimentally the feedback from those particles is suppressed by reabsorption. Thus the effective system size is reduced, as shown in our previous calculation [51].

The numerical simulations illustrate that the lasing modes are nearly identical to the quasimodes of the reduced system. The quasimodes are formed by distributed feedback from all the particles inside the reduced system. The conventional distributed feedback (DFB) lasers, made of periodic structures, operate either in the overcoupling regime or the undercoupling regime [56]. The random lasers, which can be regarded as randomly distributed feedback lasers, also have these two regimes of operation. In the undercoupling regime the quasimodes are formed *mainly* by the feedback from the scatterers near the system boundary, while in the overcoupling regime the feedback from the scatterers inside the system becomes important. Thus, the quasimodes of an undercoupled system, especially the ones with relatively high quality, have almost regular frequency spacing. Note that the feedback from the scatterers inside the system is weak but not negligible; e.g., it may cause a slight shift of mode frequency or modification of the quality factor. In our experiment with dilute suspensions of particles, the random lasing was in the undercoupling regime as a result of the weak scattering and small size of the reduced

system. Therefore, the dominant feedback from the particles near the cone ends resulted in nearly constant frequency spacing of the lasing peaks, which scaled inversely with the cone length. Due to weak feedback from the particles inside the cone, the lasing modes were not exactly equally spaced in frequency and some modes failed to lase as their quality factors were reduced. In the previous studies, e.g. Refs. [38, 42, 44, 45], the strong scattering or large system size make the random laser operate in the overcoupling regime. Thus the lasing peaks are randomly spaced. This point will be discussed in more details in the next section.

## 2.4 Quasimodes and Lasing Modes Calculation in 1D Random Systems

We have developed a numerical method based on the transfer matrix to compute the quasimodes of 1D passive systems. This time-independent method is also applied to the calculation of lasing modes at the threshold under a global or a local excitation. The random system is a 1D layered structure. It is composed of  $N$  dielectric layers with air gaps in between. The refractive index of the dielectric layers is  $n_d$ , and that of the air gaps is 1. Both the thickness  $d_1$  of the dielectric layers and the thickness of air gaps  $d_2$  are randomized.  $d_{1,2} = \bar{d}_{1,2}(1 + \sigma\eta)$ , where  $0 < \sigma < 1$  represents the degree of randomness, and  $\eta$  is a random number in  $[-1, 1]$ ,  $\bar{d}_1$  ( $\bar{d}_2$ ) is the average thickness of the dielectric layers (air gaps). Outside the random system the refractive index is constant and its value is equal to the average refractive index  $n_{eff}$  of the random system to eliminate the

boundary reflection.

According to the transfer matrix formula:

$$\begin{pmatrix} p_1 \\ q_1 \end{pmatrix} = M \begin{pmatrix} p_0 \\ q_0 \end{pmatrix} \quad (2.3)$$

where  $p_0$  and  $q_0$  represent the forward and the backward propagating waves on one side of the random system,  $p_1$  and  $q_1$  on the other side,  $M$  is a  $2 \times 2$  matrix that characterizes wave propagation through the random system. The eigenmode of such an open system can be defined as a “natural mode” or a “quasimode” by generalizing the concept of an eigenmode of a closed system [90]. The quasimode satisfies the boundary condition that there are no incoming waves but only outgoing waves through the system boundary; namely  $p_0 = 0$  and  $q_1 = 0$ . In a passive system (without gain or absorption, the refractive indices being real numbers), such boundary condition requires the vacuum wavevector be a complex number,  $k_0 = k_{0r} + ik_{0i}$ . Substituting the boundary condition into Eq. 2.3, we get  $M_{22} = 0$ . Since  $M_{22}$  is a complex number, both the real part and imaginary part of  $M_{22}$  are equal to 0. These two equations are solved to find  $k_{0r}$  and  $k_{0i}$ .  $k_{0r} = \omega/c$  tells the frequency  $\omega$  of a quasimode, and  $k_{0i} = -\gamma/c$  gives the decay rate  $\gamma$  of a quasimode.

After finding  $k_0$  of a quasimode, its wavefunction can be obtained by calculating the electric field distribution  $E(x)$  throughout the random system with the transfer matrix  $M(k_0)$ . The wavefunction inside the random system can be written as  $E(x) = E_+(x)e^{in(x)k_0x} + E_-(x)e^{-in(x)k_0x}$ , where  $n(x)$  is the (real part of) refractive index at

position  $x$ ,  $E_+(x)e^{in(x)k_0x}$  represents the forward-propagating field, and  $E_-(x)e^{-in(x)k_0x}$  the backward-propagating field. Since  $k_0$  is a complex number, the amplitudes of the forward and the backward propagating fields are  $E_+(x)e^{-n(x)k_{0i}x}$  and  $E_-(x)e^{n(x)k_{0i}x}$  ( $k_{0i} < 0$ ). These expressions show that there are two factors determining the wavefunction. The first is  $E_{\pm}(x)$ , which originates from the interference of multiply-scattered waves. The second is  $e^{\pm n(x)k_{0i}x}$ , which leads to an exponential growth of the wavefunction toward the system boundary. Outside the random system, the wavefunction grows exponentially to infinity due to the negative  $k_{0i}$ . This is clearly unphysical. Thus we disregard the wavefunction outside the random system and normalize the wavefunction within the random system to unity.

Optical gain is introduced to the random system by adding an imaginary part  $n_i$  (negative number) to the refractive index  $n(x)$ . In the case of an uniform gain,  $n_i$  is constant everywhere inside the system. Outside the random system  $n_i$  is set to zero. Different from the quasimode of a passive system, the vacuum wavevector  $k_0$  of a lasing mode is a real number. The wavevector inside the random system is a complex number,  $k = k_r + ik_i = k_0[n(x) + in_i]$ . Its imaginary part  $k_i = k_0n_i$  is inversely proportional to the gain length  $l_g$ . The onset of lasing oscillation corresponds to the condition that there are only outgoing waves through the boundary of the random system. The absence of incoming waves requires  $M_{22} = 0$  in Eq. 2.3. Again since  $M_{22}$  is a complex number, both its real part and imaginary part are zero. These two equations are solved to find  $k_0$  and  $n_i$ . Each set of solution  $(k_0, n_i)$  represents a lasing mode.  $k_0 = \omega/c$  sets the lasing

frequency  $\omega$ , and  $n_i k_0 = k_i = 1/l_g$  gives the gain length  $l_g$  at the lasing threshold. The spatial profile of the lasing mode is then obtained by calculating the field distribution throughout the random system with the transfer matrix  $M(k_0, n_i)$ . Since our method is based on the time-independent wave equation, it holds only up to the lasing threshold [91]. In the absence of gain saturation, the amplitude of a lasing mode would grow in time without bound. Thus we can only get the spatially-normalized profile of a lasing mode at the threshold. The lasing mode is normalized in the same way as the quasimode for comparison. The amplitudes of the forward and the backward propagating fields of a lasing mode are  $E_+(x)e^{-n_i k_0 x}$  and  $E_-(x)e^{n_i k_0 x}$  ( $n_i < 0$ ). The exponential growth factors  $e^{\pm n_i k_0 x}$  depend on the gain value  $|n_i k_0|$ .

Local pumping is commonly used in the random laser experiment. To simulate such situation, we introduce gain to a local region of the random system. Our method can be used to find the lasing modes with arbitrary spatial distribution of gain. The imaginary part of the refractive index  $n_i(x) = \tilde{n}_i f(x)$ , where  $f(x)$  describes the spatial profile of the gain and its maximum is set to 1,  $\tilde{n}_i$  represents the gain magnitude. The lasing modes can be found in the way similar to the case of uniform gain. The solution to  $M_{22} = 0$  gives the lasing frequency  $k_0$  and threshold gain  $\tilde{n}_i k_0$ . The normalized spatial profile of a lasing mode is then computed with  $M(k_0, \tilde{n}_i)$ .

Using the method described above, we calculate the quasimodes of 1D random systems. The quasimodes are formed by distributed feedback from the randomly-positioned dielectric layers. We investigate many random structures with different scattering strengths.

Depending on the relative values of the localization length  $\xi$  and the system length  $L$ , there are two distinct regimes in which the quasimodes are dramatically different: (i) overcoupling regime  $L > \xi$ ; (ii) undercoupling regime  $L \ll \xi$ .

As an example, we consider the random structure with  $\bar{d}_1 = 100\text{nm}$  and  $\bar{d}_2 = 200\text{nm}$ .  $\sigma = 0.9$  for both  $d_1$  and  $d_2$ . To change from the undercoupling regime to the overcoupling regime, we increase the refractive index  $n_d$  of the dielectric layers. In particular, we take  $n_d = 1.05$  and  $2.0$ . The larger  $n_d$  leads to stronger scattering and shorter localization length  $\xi$ . To obtain the value of  $\xi$ , we calculate the transmission  $T$  as a function of the system length  $L$ .  $\langle \ln T \rangle$  is obtained from averaging over 10,000 configurations with the same  $L$  and  $\sigma$ . When  $L > \xi$ ,  $\langle \ln T(L) \rangle$  decays linearly with  $L$ , and  $\xi^{-1} = -d\langle \ln T(L) \rangle/dL$ . In the wavelength ( $\lambda$ ) range of 500nm to 750nm,  $\xi$  exhibits slight variation with  $\lambda$  due to the residual photonic bandgap effect. For  $n_d = 1.05$ ,  $\xi \sim 200 - 240\mu\text{m}$ , while for  $n_d = 2.0$ ,  $\xi \sim 1.2 - 1.5\mu\text{m}$ . In the calculation of quasimodes, we fix the system size  $L = 24.1\mu\text{m}$ . Thus, for  $n = 1.05$ ,  $\xi \gg L$  in the wavelength range of interest and the random system is in the undercoupling regime; while for  $n = 2.0$ ,  $\xi \ll L$  and the system is in the overcoupling regime.

To illustrate the difference between overcoupling regime and undercoupling regime, we compare the quasimodes of the same random structure with different  $n_d$ , namely,  $n_d = 2.0$  or  $1.05$ . Figures 2.11(a) and (b) are the typical transmission spectra of these two systems. For the system with  $n_d = 2.0$  most transmission peaks are narrow and well separated in frequency, while for  $n_d = 1.05$  the transmission peaks are typically broad

and overlapped. We find  $k_0 = k_{0r} + ik_{0i}$  of the quasimodes in the wavelength range of 500-750nm. Figure 2.11(c) shows the values of  $k_{0r}$  and  $k_{0i}/\langle k_{0i} \rangle$  of these modes ( $\langle k_{0i} \rangle$  is the average over all the quasimodes in the wavelength range of 500-750nm). In the system with  $n_d = 2.0$ , most quasimodes are well separated spectrally, and they match the transmission peaks.  $k_{0r}$  corresponds to its frequency and  $k_{0i}$  to its linewidth. However, some quasimodes locate close to the system boundary and have relatively large  $k_{0i}$ . They are usually invisible in the transmission spectrum due to spectral overlap with neighboring transmission peaks, which cause the number of transmission peaks [Fig. 2.11(a)] slightly less than the number of quasimodes [solid squares in Fig. 2.11(c)]. In the system with  $n_d = 1.05$ , however, the number of peaks in the transmission spectrum [Fig. 2.11(b)] is significantly less than the number of quasimodes [open circles in Fig. 2.11(c)]. This is because in the undercoupling regime the decay rates of the quasimodes often exceed the frequency spacing to neighboring modes. The spectral overlap of the quasimodes makes the transmission peaks less evident and some even buried by the neighboring ones.

It is clear in Fig. 2.11(c) that the decay rate fluctuation is much stronger in the random system with  $n_d = 2.0$  (solid squares) than that with  $n_d = 1.05$  (open circles). This is consistent with the broadening of the quasimode decay rate distribution as a system approaches the localization regime with increasing scattering strength. Figure 2.11(d) plots the frequency spacing  $\Delta k_{0r}$  between adjacent quasimodes normalized to the average value  $\langle \Delta k_{0r} \rangle$ . The quasimodes of the random system with  $n_d = 1.05$  are more regularly spaced in frequency than those in the system with  $n_d = 2.0$ .

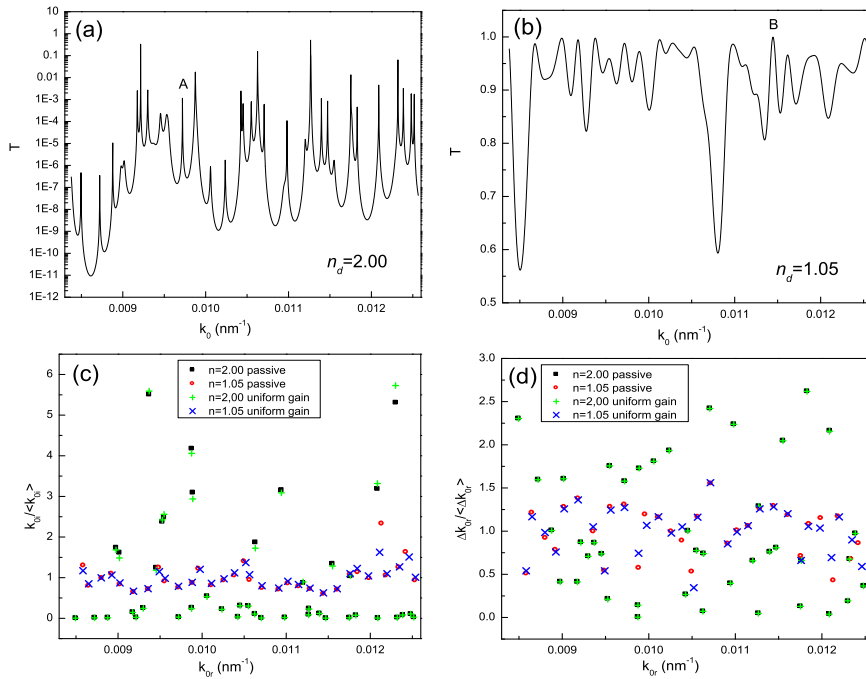


Figure 2.11: (a), (b): Transmission  $T$  through a 1D random structure with  $n_d = 2.0$ , 1.05 as a function of vacuum wavevector  $k_0$ . (c) Frequencies  $k_{0r}$  and normalized decay rates  $k_{0i}/\langle k_{0i} \rangle$  of the quasimodes in the random systems with  $n_d = 2.0$  (solid square) and  $n_d = 1.05$  (open circle), compared with the frequencies  $k_0$  and normalized threshold gain  $k_i/\langle k_i \rangle$  of lasing modes in the same systems with  $n_d = 2.0$  (+) and  $n_d = 1.05$  ( $\times$ ) under uniform excitation. (d) Normalized frequency spacing  $\Delta k_{0r}/\langle \Delta k_{0r} \rangle$  of neighboring quasimodes in the random systems with  $n_d = 2.0$  (solid square) and  $n_d = 1.05$  (open circle), compared with the normalized frequency spacing  $\Delta k_0/\langle \Delta k_0 \rangle$  of neighboring lasing modes in the same systems with  $n_d = 2.0$  (+) and  $n_d = 1.05$  ( $\times$ ) under uniform excitation.

To interpret this phenomenon, we investigate the wavefunctions of the quasimodes. Figure 2.12(a) [(b)] shows the spatial distribution of intensity  $I(x) = |E(x)|^2$  for a typical quasimode of the random system with  $n_d = 2.0$  ( $n_d = 1.05$ ).  $I(x)$  is normalized such that the spatial integration of  $I(x)$  within the random system is equal to unity. The expression of  $E(x)$  given in the previous section reveals the two factors determining the envelop of the wavefunction, i.e., the interference term  $E_{\pm}(x)$  and the exponential growth term  $e^{\pm n(x)k_0 i x}$ . Depending on which term is dominant, the spatial profile of the quasimodes can be drastically different. In the overcoupling regime, strong scattering makes the interference term dominant, and  $I(x)$  exhibits strong spatial modulation. Most quasimodes are localized inside the random system, similar to the mode in Fig. 2.12(a). Their decay rates are low as a result of the interference-induced localization. In the undercoupling regime, the interference effect is weak due to small amount of scattering. The exponential growth term  $e^{\pm n(x)k_0 i x}$  dominates  $E(x)$ , making  $I(x)$  increase exponentially toward the boundaries. The interference term only causes weak intensity modulation. A typical example of such mode profile is exhibited in Fig. 2.12(b). Since the quasimodes in the under-coupling system are spatially extended across the entire random system, the decay rates of the quasimodes are much higher than those of the localized modes in the overcoupling system.

We repeat the above calculations with many random systems, and find the two different types of quasimodes are rather typical for the systems in the overcoupling and undercoupling regimes. The mode profiles and frequency spacings in the undercoupling

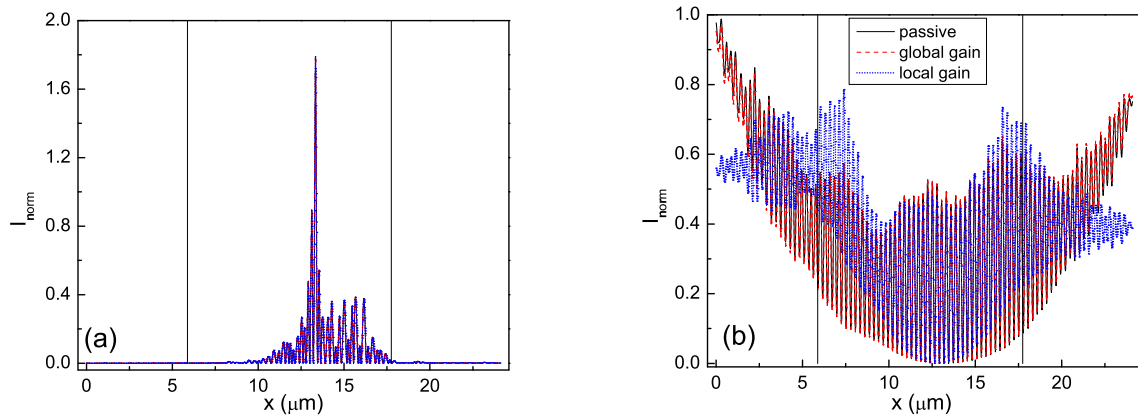


Figure 2.12: Spatial intensity distributions of quasimodes (black solid curve) and the corresponding lasing modes in the presence of global gain (red dashed curve) or local gain (green dotted curve). The pumped region is between the two vertical lines,  $L_p = 11.87\mu\text{m}$ . (a) The mode marked as A in Fig. 2.11(a),  $\lambda = 646\text{ nm}$ ,  $n_d = 2.0$ . (b) The mode marked as B in Fig. 2.11(b),  $\lambda = 549\text{ nm}$ ,  $n_d = 1.05$ .

systems imply the feedbacks from the dielectric layers close to the boundaries are dominant over those from the interior. However, the feedbacks from the scatterers in the interior of the system are weak but not negligible, e.g. they induce small fluctuations in the frequency spacings and the decay rates. Note that a random system in the undercoupling regime cannot be approximated as a uniform slab with the average refractive index  $n_{eff}$ , despite its quasimodes exhibit some similar features as the Fabry-Perot cavity modes. Since in our calculation the refractive index outside the random system is set to  $n_{eff}$ , there would be no quasimodes if the random system were replaced by a dielectric slab of  $n_{eff}$ . Hence, the quasimodes in the undercoupling regime are not formed by the boundary reflection. In the overcoupling regime, the feedback from the scatterers deep inside the system becomes dominant, and the interference of multiply scattered waves

lead to the spatial localization of the quasimodes.

Next we study the lasing modes in the random system with uniform gain and compare them to the quasimodes.  $n_i$  is constant everywhere within the random system and so the gain length  $l_g = 1/k_i = 1/k_0 n_i$ . Using the method described in the previous section, we find the frequency and the threshold gain of each lasing mode. We calculate the lasing modes in the same random systems as in Fig. 2.11 within the same wavelength range (500-750nm). The frequency  $k_0$  and normalized threshold  $k_i/\langle k_i \rangle$  of each lasing mode are plotted in Fig. 2.11(c) for comparison with the quasimodes. It is clear that there exists one-to-one correspondence between the lasing modes and the quasimodes for the random systems in both overcoupling and undercoupling regimes. For the system with  $n_d = 2.0$ , the lasing modes match the quasimodes well, with only slight difference between  $k_i/\langle k_i \rangle$  and  $k_{0i}/\langle k_{0i} \rangle$  for the relatively leaky modes. For the system with  $n_d = 1.05$ , the deviation of the lasing modes from the quasimodes is more evident, especially for those modes with large decay rates. Such deviation can be explained by the modification of the transfer matrix  $M$ . In the passive system,  $k_{0i}$  is constant but  $k_i = k_{0i} n(x)$  varies spatially. With the introduction of the uniform gain,  $k_i$  becomes constant within the random system, and the feedback inside the random system is caused only by the contrast in the real part of the wavevector  $k_r = k_0 n(x)$  between the dielectric layers and the air gaps. With a decrease in the scattering strength,  $k_{0i}$  in the passive system gets larger, and the ratio of the feedback caused by the contrast in  $k_i$  to that in  $k_r$  increases. The addition of uniform gain results in a bigger change of  $M$ , as it removes the feedback due to the inhomogeneity

of  $k_i$ . Moreover, since there is no gain outside the random system,  $k_i$  suddenly drops to zero at the system boundary. This discontinuity of  $k_i$  generates additional feedback for the lasing modes. In a weakly scattering system, the threshold gain of the lasing modes is high. The larger drop of  $k_i$  at the system boundary makes the additional feedback stronger. To check its contribution to lasing, we replace the random system with a uniform slab of  $n_{eff}$  while keeping the same gain profile. Since the real part of the refractive index or  $k_r$  is homogeneous throughout the entire space, the feedback comes only from the discontinuity of  $k_i$  at the slab boundaries. We find the lasing threshold in the uniform slab is significantly higher than that in the random system with  $n_d = 1.05$ . This result confirms that for the random systems in Fig. 2.11, the additional feedback caused by the  $k_i$  discontinuity at the system boundary is weaker than the feedback due to the inhomogeneity of  $k_r$  inside the random system. However, if we further reduce  $n_d$  or  $L$ , the threshold gain increases, and the feedback from the system boundary due to gain discontinuity eventually plays a dominant role in the formation of lasing modes.

We also compute the intensity distribution  $I(x)$  of each lasing mode at the threshold.  $I(x)$  is normalized such that its integration across the random system is equal to 1. Such normalization facilitates the comparison of the lasing mode profile to the quasimode profile. In Fig. 2.12(a) [(b)],  $I(x)$  of the lasing mode is plotted together with that of the corresponding quasimode. Although the lasing mode profiles in Figs. 2.12(a) and (b) are quite different, they are nearly identical to those of the quasimodes. For the localized mode in the random system with  $n_d = 2.0$ ,  $I(x)$  of the lasing mode does not exhibit

any visible difference from that of the quasimode in Fig. 2.12(a). For the extended mode in the system with  $n_d = 1.05$ , the lasing mode profile deviates slightly from the quasimode profile, especially near the system boundaries. This deviation results from the modification of the transfer matrix  $M$  by the introduction of the uniform gain across the random system. The modification is bigger in the under-coupling system, leading to larger difference in the mode profile.

Finally we investigate the lasing modes under local excitation. In particular,  $f(x) = 1$  for  $|x - x_c| \leq L_1/2$ ,  $f(x) = \exp[-|x - x_c|/L_2]$  for  $L_1/2 < |x - x_c| \leq L_1/2 + 2L_2$ , and  $f(x) = 0$  elsewhere ( $x_c = L/2$ ). The lasing mode frequency  $k_0$ , the threshold gain  $\tilde{k}_i = k_0 \tilde{n}_i$ , and the spatial profile  $I(x)$  are calculated with the method described in the previous section.  $I(x)$  is normalized in the same way as that of a quasimode for comparison. As an example, we consider the same random structures as in Fig. 2.11 and introduce gain to the central region of length  $L_p = L_1 + 4L_2 = 8.84 + 3.03 = 11.87 \mu\text{m}$  (marked by two vertical lines in Fig. 2.12). Figures 2.13(a) plots  $k_0$  and  $\tilde{k}_i / \langle \tilde{k}_i \rangle$  for all the lasing modes within the wavelength range of 500-750nm. Comparing with Fig. 1, we find some quasimodes fail to lase under local pumping, no matter how high the pumping level is. The rest modes lase but their wavefunctions are significantly modified by the particular local excitation. The two quasimodes shown in Fig. 2.12 both lase under the local pumping configuration and their intensity distributions at threshold are plotted. The mode in Fig. 2.12(a) is localized within the pumped region, and its spatial profile is barely modified by the local gain. In contrast, the mode in Fig. 2.12(b) is spatially

extended and has less overlap with the central gain region. The intensity distribution of the lasing mode differs notably from that of the quasimode. The exponential growth of  $I(x)$  toward the system boundaries is suppressed outside the gain region, while inside the gain region  $I(x)$  grows exponentially toward the ends of the gain region at a rate higher than that of the quasimode. These behaviors can be explained by the spatial variation of gain. Outside the pumped region, there is no optical amplification thus  $I(x)$  does not increase exponentially. Within the pumped region, the faster intensity growth results from the higher threshold gain for lasing with local pumping than that with global pumping. Nevertheless, the close match in the number and spatial position of intensity maxima justifies the correspondence of the lasing mode to the quasimode.

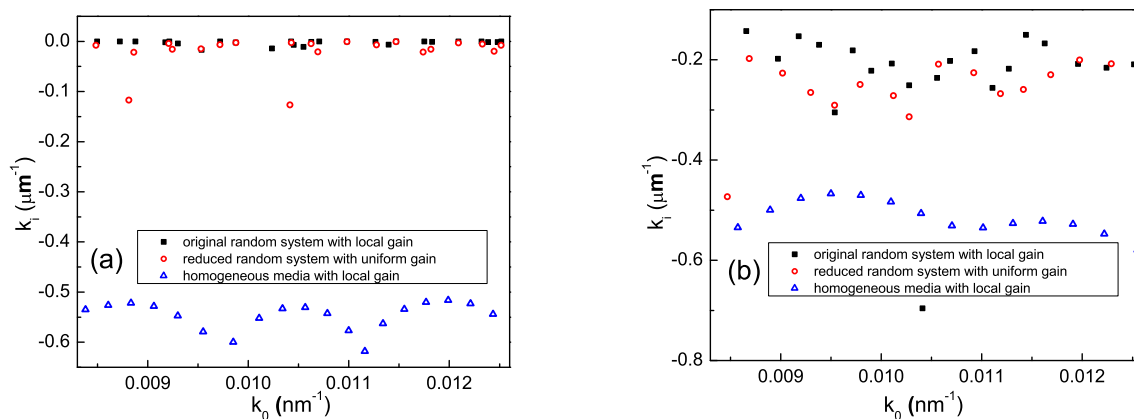


Figure 2.13: (a) Normalized threshold gain  $\tilde{k}_i/\langle k_i \rangle$  versus the frequency  $k_0$  of lasing modes in the random systems with  $n_d = 2.0$  (solid squares) and  $n_d = 1.05$  (open circles) under local excitation (between the two vertical lines in Fig. 2.12). (b) Normalized frequency spacing  $\Delta k_0/\langle \Delta k_0 \rangle$  of neighboring lasing modes in the systems with  $n_d = 2.0$  (solid squares) and  $n_d = 1.05$  (open circles) under local excitation.

We repeat the calculation with many modes under the same pumping configuration,

and find the weight of a mode within the gain region is often enhanced. To quantify such enhancement, we introduce a parameter  $\delta$  which is equal to the ratio of  $I(x)$  integrated over the pumped region to that over the entire random system. We compare the values of  $\delta$  for the lasing modes under local excitation to that of the corresponding quasimodes. For the mode Fig. 2.12(b),  $\delta$  is increased from 0.33 for the quasimode to 0.41 for the lasing mode, while for the mode in Fig. 2.12(a)  $\delta$  remains at 0.98. Thus the effect of local pumping is stronger for the modes in the weakly scattering system. This is because when scattering is weak the local gain required for lasing is high. The feedback within the pumped region is greatly enhanced, leading to the modification of the mode profile.

We also investigate the fluctuations in threshold gain and frequency spacing of lasing modes under local excitation. Figure 2.13(a) shows the lasing threshold fluctuation for the random system with  $n_d = 1.05$  is smaller than that with  $n_d = 2.0$ . Since the number of lasing modes under local pumping is usually less than that of quasimodes, the average mode spacing  $\langle \Delta k_0 \rangle$  is increased. Figure 2.13(b) plots the frequency spacing  $\Delta k_0$  of adjacent lasing modes normalized to the average value  $\langle \Delta k_0 \rangle$ . There is more fluctuation in the mode spacing for the random system with  $n_d = 2.0$  than that with  $n_d = 1.05$ . Hence, with local gain the frequency spacing of lasing modes is more regular in the undercoupling regime than in the overcoupling regime. This result is similar to that with uniform gain.

Although the local pumping enhances the feedback within the pumped region, the feedback outside the pumped region cannot be neglected. To demonstrate this, we cal-

culate the lasing modes in the reduced systems of length  $L_p$  by replacing the random structures outside the gain region with a homogeneous medium of  $n_{eff}$ . The reduced system has uniform gain instead of the gain profile  $f(x)$  in the original system. The results are shown in Fig. 2.14(a) for the system with  $n_d = 2.0$  and in Fig. 2.14(b) for the system with  $n_d = 1.05$ . The number of lasing modes in the reduced system is less than that in the original system under local pumping. In fact, the lasing modes are generally different, with only exception for a few modes localized within the gain region in the system with  $n_d = 2.0$ . Moreover, the lasing threshold in the reduced system is higher than that in the original system with local gain. These differences are attributed to the feedbacks from the random structure outside the pumped region of the original system. It demonstrates the scatterers in the unpumped region also provides feedback for lasing. By comparing Figs. 2.14(a) and (b), we find the difference in the lasing threshold between the original system under local pumping and the reduced system is smaller for the system with  $n_d = 1.05$  than that with  $n_d = 2.0$ . It indicates the contribution from the scatterers outside the gain region to lasing is reduced as the system moves further into the undercoupling regime.

We note that local pumping introduces inhomogeneity in the imaginary part of the refractive index, which generates additional feedback for lasing. To check its effect, we simulate lasing in a homogeneous medium with the average refractive index  $n_{eff}$ . The local gain profile  $f(x)$  remains the same. Only the spatial variation of  $k_i(x) = k_0 \tilde{n}_i f(x)$  provides the feedback for lasing. As shown in Figs. 2.14(a) and (b), the lasing thresholds

are much higher than those in the random systems, even for the system with  $n_d = 1.05$ . This result demonstrate that for the random systems in Figs. 2.13 and 2.14, the feedbacks for lasing under local pumping are predominately caused by the inhomogeneities in the real part of the refractive index  $n(x)$  or the wavevector  $k_r(x) = k_0 n(x)$ . However, a further reduction in either  $n_d$  or  $L_p$  could make the feedback due to the inhomogeneity of  $k_i(x)$  more significant.

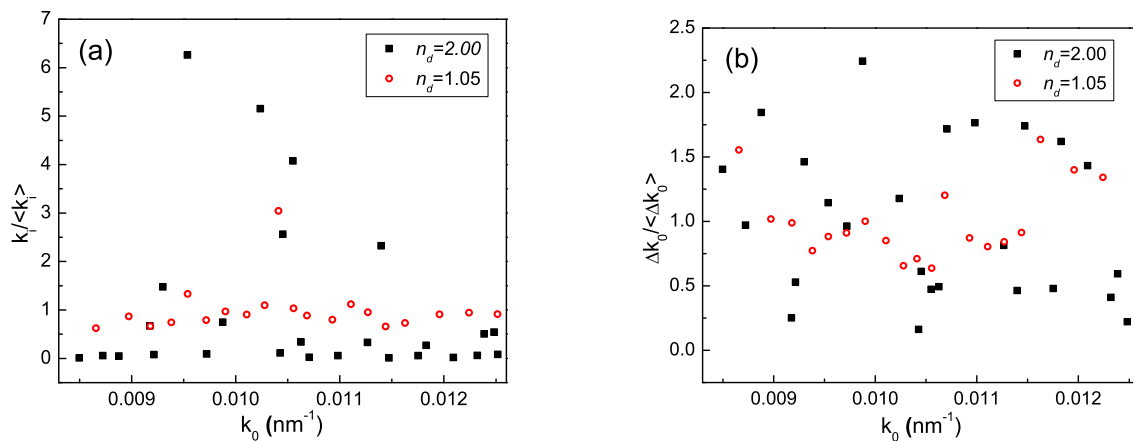


Figure 2.14: : Threshold gain  $\tilde{k}_i / \langle \tilde{k}_i \rangle$  of lasing modes in the (original) random system of length  $24.1\mu\text{m}$  with local excitation in the central region of length  $11.87\mu\text{m}$  (solid square), compared to the threshold gain of lasing modes in the reduced system of length  $11.87\mu\text{m}$  under uniform excitation (open circle) and the threshold gain of lasing modes in the homogeneous medium with  $n_{eff}$  under local excitation in the region of length  $11.87\mu\text{m}$  (a)  $n_d = 2.0$ ,  $n_{eff} = 1.3361$ , (b)  $n_d = 1.05$ ,  $n_{eff} = 1.0168$ .

In conclusion, we have developed a numerical method to calculate the quasimodes of 1D passive random systems and the lasing modes at the threshold with either global or local pumping. We identify two regimes for the quasimodes: overcoupling regime ( $L > \xi$ ) and undercoupling regime ( $L \ll \xi$ ). In the undercoupling regime the electric field of a

quasimode grows exponentially toward the system boundaries, while in the overcoupling regime the field maxima are located inside the random system. The frequency spacings of adjacent modes are more regular in the undercoupling regime, and there is less fluctuation in their decay rates. The distinct characteristic of the quasimodes in the two regimes result from the different mechanisms of mode formation. In an overcoupled system, the quasimodes are formed mainly by the interference of multiply scattered waves by the particles in the interior of the random system. In contrast, the feedbacks from the scatterers close to the system boundaries play a dominant role in the formation of quasimodes in an undercoupled system. The contributions from the scatterers in the interior of the random system to the mode formation are weak but not negligible. They induce small fluctuations in mode spacing and decay rate. As the scattering strength is increased, the feedbacks from those scatterers in the interior of the system get stronger, and the frequency spacing of the quasimodes becomes more random.

In the presence of uniform gain across the random system, the lasing modes (at the threshold) have one-to-one correspondence with the quasimodes in both overcoupled and undercoupled systems. However, the lasing modes may differ slightly from the corresponding quasimodes in frequency and spatial profile, especially in the undercoupled systems. This is because the introduction of uniform gain removes the feedback caused by spatial inhomogeneity of the imaginary part of the wavevector within the random system and creates additional feedback by the discontinuity of the imaginary part of the wavevector at the system boundaries. As long as the scattering is not too weak, the quasi-

modes are only slightly modified by the introduction of uniform gain and they serve as the lasing modes. This conclusion is consistent with that drawn from the time-dependent calculations [60, 61, 92]. Hence, the knowledge of the decay rates of the quasimodes, in conjunction with the gain spectrum, can predict the first lasing mode. Because of the correspondence between the lasing modes and the quasimodes, the frequency spacing of adjacent lasing modes is more regular in the undercoupled systems with smaller mode-to-mode variations in the lasing threshold.

When optical gain is introduced to a local region of the random system, some quasimodes cannot lase no matter how high the gain is. The rest modes can lase but their spatial profiles may be significantly modified. Such modifications originate from strong enhancement of feedbacks from the scatterers within the pumped region. It increases the weight of a lasing mode within the gain region. Nevertheless, the feedbacks from the scatterers outside the pumped region are not negligible. Moreover, the spatial variation in the imaginary part of the refractive index generates additional feedback for lasing. As the pumped region becomes smaller, the number of lasing modes is reduced, and the frequency spacing of lasing modes is increased. In an undercoupled system, the regularity in the lasing mode spacing remains under local excitation. Our calculation results will help to interpret the latest experimental observations [49, 63] of spectral periodicity of lasing peaks in weakly scattered random systems under local pumping. We note that the effect of local excitation can be significant in an overcoupled system if the size of the pumped region is much smaller than the spatial extend of a localized mode or the spatial

overlap between the pumped region and the localized mode is extremely small. Hence, caution must be exerted in using the decay rates of quasimodes to predict the lasing threshold or the number of lasing modes under local excitation. Finally we comment that the increase in the mode concentration in the gain region by local pumping have distinct physical mechanism from the absorption-induced localization of lasing modes in the pumped region [51]. The former is based on selective enhancement of feedback within the gain region, while the latter on the suppression of the feedback outside the pumped region by reabsorption.

## **2.5 Statistics of Amplified Spontaneous Emission Spikes and Coherent Random Laser Peaks**

In addition to the random lasing peaks, stochastic spikes were reported in the single-shot spectra of amplified spontaneous emission (ASE) from dye colloidal solutions over a wide range of scattering strength [71]. The spikes are intrinsically stochastic and vary from shot to shot. They are attributed to single spontaneous emission events which happen to take long open paths inside the amplifying random medium and pick up large gain [67]. Thus the emergence of ASE spikes does not rely on resonant feedback or coherent interference. To clarify the difference between the lasing peaks and ASE spikes, we conduct a systematic study and show that the ASE spikes can appear without scattering but the lasing peaks rely on the coherent feedback provided by scattering. The ensemble-averaged spectral correlation functions and the statistical distributions of

the spectral spacing and intensity of the ASE spikes and the lasing peaks are completely different. Such differences underline the distinct physical mechanisms.

Our experiments were performed on the diethylene glycol solutions of stilbene 420 dye and  $\text{TiO}_2$  particles (mean radius = 200nm). The experimental setup was the same as that described in Section 2.2. The stilbene 420 was intentionally chosen for the weak reabsorption of emitted light outside the pumped region. The absorption length  $l_a$  at the center emission wavelength  $\lambda_e = 427\text{nm}$  was 6cm at the dye concentration  $M = 8.5\text{mM}$ . It was much larger than the dimension ( $\sim 1\text{cm}$ ) of the cuvette that held the solution. At the particle density  $\rho = 3 \times 10^9\text{cm}^{-3}$ , the scattering mean free path  $l_s \simeq 1.3\text{mm}$  at the pump wavelength  $\lambda_p = 355\text{nm}$ , and  $l_s \simeq 1.0\text{mm}$  at  $\lambda_e$ . Although  $l_a \simeq 10\mu\text{m}$  at  $\lambda_p$ , the pump light penetrated much deeper than  $l_a$  due to the saturation of absorption by intense pumping. The excitation volume had a cone shape of length a few hundred micron and base diameter  $30\mu\text{m}$ . Because the cone length was smaller than  $l_s$ , the excitation cone in the colloidal solution was almost identical to that in the neat dye solution. For the emitted light, the transport was diffusive in the colloidal solution whose dimension was much larger than  $l_s$ . Light amplification, however, occurred only in a sub-mean-free-path region. The motion of particles in the solution provided different random configuration for each pump pulse, which facilitated the ensemble measurement under identical conditions.

The single-shot emission spectra from the colloidal solution are shown in Figs. 1(a)-(c) with increasing pump pulse energy  $E_p$ . At  $E_p = 0.05\mu\text{J}$  [Fig. 1(a)], the spectrum exhibited sharp spikes on top of a broad ASE band. From shot to shot the spikes changed

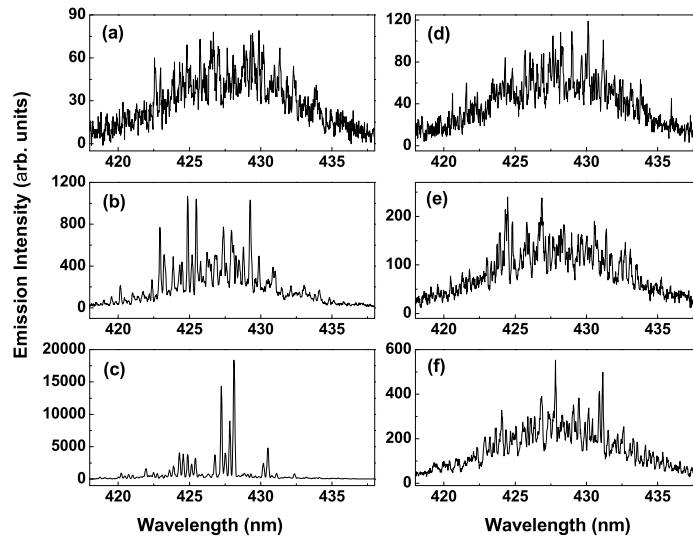


Figure 2.15: Single-shot emission spectrum from the 8.5mM stilbene 420 dye solutions with  $3 \times 10^9 \text{cm}^{-3}$   $\text{TiO}_2$  particles (a)-(c) and without particles (d)-(f). The pump pulse energy is  $0.05 \mu\text{J}$  for (a) & (d),  $0.09 \mu\text{J}$  for (b) & (e),  $0.13 \mu\text{J}$  for (c) & (f).

completely. The typical linewidth of the spikes was about 0.07nm. The neighboring spikes often overlap partially. As pumping increased, the spikes grew in intensity. When  $E_p$  exceeded a threshold, a different type of peaks emerged in the emission spectrum [Fig. 1(b)]. They grew much more rapidly with pumping than the spikes, and dominated the emission spectrum at  $E_p = 0.13 \mu\text{J}$  [Fig. 1(c)]. The peaks, with the typical width of 0.13nm, were notably broader than the spikes. Unlike the spikes, the spectral spacing of adjacent peaks was more or less regular. We repeated the experiment with solutions of different  $\rho$  as well as the neat dye solution of the same  $M$ . The peaks could only be observed with particles in the solution, while the spikes appeared also in the spectrum of emission from the neat dye solution [Fig. 1(d) - (f)]. Although they were similar at  $E_p = 0.05 \mu\text{J}$ , the emission spectra with and without particles were dramatically different

at  $E_p = 0.13\mu\text{J}$ . Even under intense pumping, the emission spectrum of the neat dye solution had only spikes but no peaks [Fig. 1(f)]. The maximum spike intensity was about 50 times lower than the maximum peak intensity in the colloidal solution at the same pumping [Fig. 1(c)]. While the pump threshold for the appearance of peaks depended on  $\rho$ , the threshold for the emergence of spikes in solutions with low  $\rho$  was similar to that with  $\rho = 0$ .

In our previous experimental and numerical studies [63], we concluded that the large peaks represented the lasing modes formed by distributed feedback in the colloidal solution of  $\text{TiO}_2$  particles. Although the feedback was weak at low particle density, the intense pumping strongly amplified the backscattered light and greatly enhanced the feedback. In contrast, the feedback from the particles was not necessary for the spikes which also existed in the neat dye solution. Thus the spikes were attributed to the amplified spontaneous emission.

To demonstrate quantitatively the differences between the ASE spikes and lasing peaks, we investigated their spectral correlations and intensity statistics. Since it was difficult to obtain reliable statistical data for the ASE spikes from the colloidal solution at high pumping due to the presence of dominant lasing peaks, the data of ASE spikes were taken from the neat dye solution instead. We checked that at low pumping where the lasing peaks had not appeared, the statistical data for ASE spikes collected from the colloidal solution with low  $\rho$  were similar to those from the neat dye solution. The ensemble-averaged spectral correlation function  $C(\Delta\lambda)$  was obtained from 200 single-

shot emission spectra acquired under identical condition. We chose the wavelength range 425-431 nm, within which the gain coefficient did not change much, to compute  $C(\Delta\lambda) = \langle I(\lambda)I(\lambda + \Delta\lambda) \rangle / \langle I(\lambda) \rangle \langle I(\lambda + \Delta\lambda) \rangle - 1$ . At low pumping [Figs. 1(a) & (d)]  $C(\Delta\lambda)$  for the neat dye solution was very similar to that for the colloidal solution with low  $\rho$ , while at high pumping [Figs. 1(c) & (f)]  $C(\Delta\lambda)$  became significantly different as shown in Figure 2(a).  $C(\Delta\lambda = 0)$ , which was equal to the intensity variance, had a much larger value for the colloidal solution than for the neat dye solution. This result reflected the intensity ratio of the lasing peaks to the background emission was much higher than that of the ASE spikes. Moreover,  $C(\Delta\lambda)$  for the colloidal solution exhibited regular oscillations with the period  $\sim 0.27\text{nm}$ . Due to slight variation of lasing peak spacing, the oscillation was damped and the correlation peaks were broadened with increasing  $\Delta\lambda$ . Nevertheless, the oscillation of  $C(\Delta\lambda)$  survived the ensemble average despite the lasing peaks changed from shot to shot. This result confirmed not only the lasing peaks in a single-shot spectrum were more or less regularly spaced, but also the average peak spacing was nearly the same for different shots. In contrast,  $C(\Delta\lambda)$  for the neat dye solution was smooth and decayed quickly to 0 as  $\Delta\lambda$  increased from 0 [inset of Fig. 2(a)]. The ASE spikes produced irregular oscillations in the spectral correlation function of a single shot emission spectrum. However, such oscillations were removed after averaging over many shots. This result reflected the stochastic nature of the ASE spikes.

We also obtained the statistical distribution  $P(\delta\lambda)$  of wavelength spacing  $\delta\lambda$  of the ASE spikes and that of the lasing peaks. The cross in Fig. 2.16(b) represented  $P(\delta\lambda)$

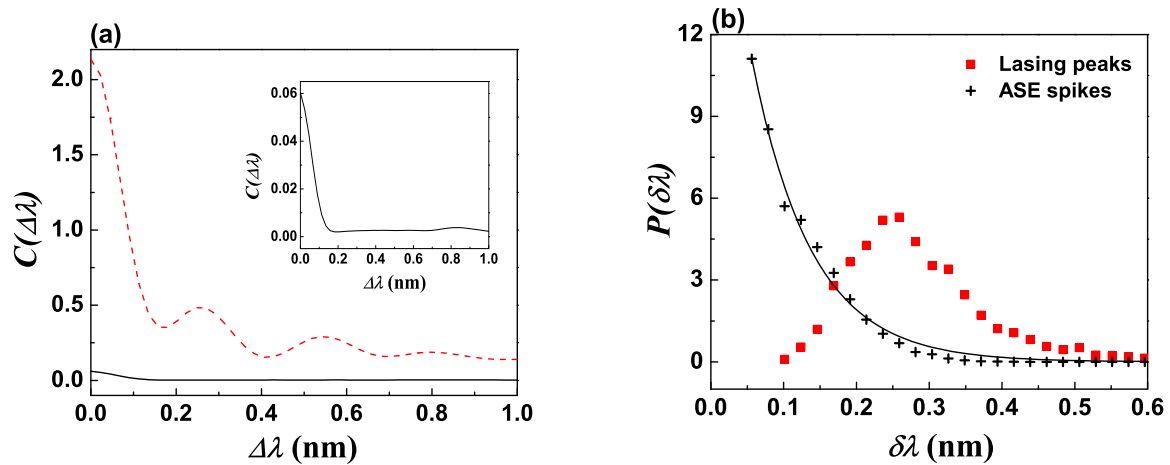


Figure 2.16: (a) Ensemble-averaged spectral correlation function of single-shot emission spectra for 8.5mM stilbene 420 dye solutions with  $3 \times 10^9 \text{ cm}^{-3}$   $\text{TiO}_2$  particles (dashed curve) and without particles (solid curve). The pump pulse energy is  $0.13 \mu\text{J}$ . (b) Statistical distribution of wavelength spacing between adjacent lasing peaks (square) and ASE spikes (cross) obtained from the same spectra as in (a). The solid curve represents an exponential fit  $P(\delta\lambda) \sim \exp(-\delta\lambda/0.082)$ .

for the ASE spikes within the wavelength range 425-431nm, obtained from 200 emission spectra of the neat dye solution at  $E_p = 1.0 \mu\text{J}$ . Note that the data at  $\delta\lambda$  close to 0 were absent because two ASE spikes with spacing less than the spike width could not be resolved.  $P(\delta\lambda)$  was fitted by an exponential decay,  $P(\delta\lambda) \sim \exp(-\delta\lambda/0.082)$  [solid curve in Fig. 2.16(b)]. It showed the ASE spikes satisfied the Poisson statistics, which meant the frequencies of individual ASE spikes were uncorrelated.  $P(\delta\lambda)$  for the lasing peaks [square in Fig. 2.16(b)] differed dramatically from that for the ASE spikes. Instead of an exponential decay,  $P(\delta\lambda)$  reached the maxima at  $\delta\lambda \sim 0.25 \text{ nm}$ . This result reflected the spectral repulsion of lasing modes. Since the particle suspension was in the diffusive regime, its quasimode spacing  $\delta\lambda$  would satisfy the Wigner-Dyson distribution  $P(\delta\lambda) \sim$

$\delta\lambda \exp[-\pi(\delta\lambda)^2/4\langle\delta\lambda\rangle^2]$  [93]. However,  $P(\delta\lambda)$  for the lasing modes did not fit well with the Wigner-Dyson distribution. The deviation might be caused by several factors such as the mode competition for gain which would limit the number of lasing modes [94]. Our numerical simulations, to be presented later, illustrated that the local pumping could strongly modify the quasimodes even without reabsorption. Since the lasing modes might be quite different from the quasimodes, the statistics of the lasing mode spacing could differ from that for the quasimode spacing.

Further difference between the ASE spikes and lasing peaks was revealed in the intensity statistics. From hundreds of emission spectra taken under identical conditions, we obtained the statistical distributions of the intensities ( $I$ ) of lasing peaks and ASE spikes within the wavelength range 425 - 431nm. Some of the data were presented in Fig. 2.17, which illustrated the two distributions were very different. The log-linear plot in Fig. 2.17(a) clearly showed that  $P(I/\langle I \rangle)$  for the ASE spikes had an exponential tail at large  $I$ . The tail became more extended as the pump pulse energy  $E_p$  increased. The solid and dotted curves in Fig. 2.17(a) represented the exponential fit  $P(I/\langle I \rangle) \sim \exp(-aI/\langle I \rangle)$  at large  $I$  for  $E_p = 0.13\mu\text{J}$  (cross) and  $0.39\mu\text{J}$  (triangle) with  $a = 5.7$  and  $4.0$ , respectively. The log-log plot in Fig. 2.17(b) revealed that  $P(I/\langle I \rangle)$  for the lasing peaks had a power-law decay at large  $I$ , namely,  $P(I/\langle I \rangle) \sim (I/\langle I \rangle)^{-b}$ . The fit of the data at  $E_p = 0.09\mu\text{J}$  (open circles) and  $0.13\mu\text{J}$  (solid squares) gave  $b = 3.0$  and  $2.3$ , respectively. Hence, the power-law decay became slower with increasing pump pulse energy.

The above experimental results of correlations and statistics demonstrated the fun-

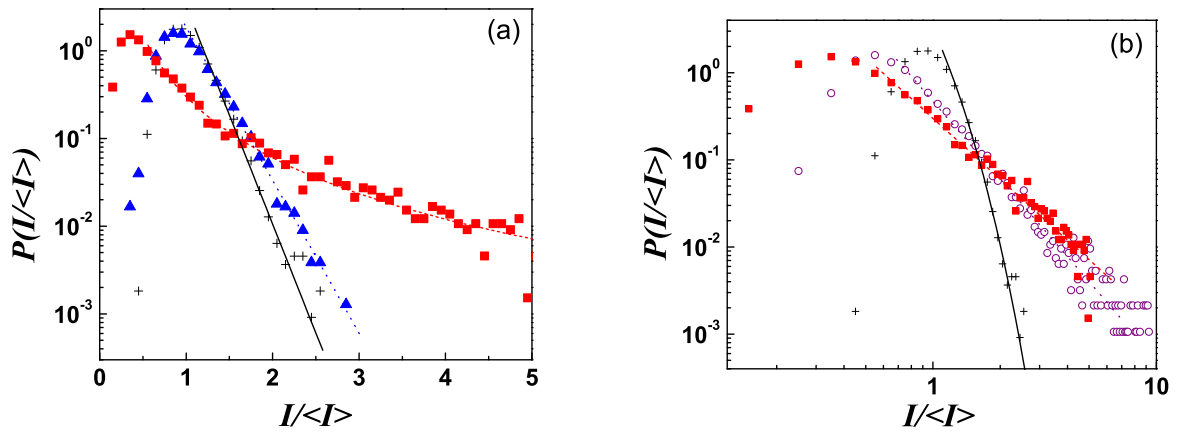


Figure 2.17: Statistical distributions of the intensities of lasing peaks (square, circle) and ASE spikes (cross, triangle), obtained from the 8.5mM stilbene 420 dye solutions with  $3 \times 10^9 \text{cm}^{-3}$   $\text{TiO}_2$  particles and without particles, respectively. The pump pulse energy is  $0.09 \mu\text{J}$  (circle),  $0.13 \mu\text{J}$  (square, cross),  $0.39 \mu\text{J}$  (triangle). The lines represent fitting (see text).

damental difference between the ASE spikes and lasing peaks. Note that the data for the ASE spikes were taken from the neat dye solution to avoid large lasing peaks at high pumping. At low pumping where the lasing peaks had not appeared, the data for ASE spikes obtained from the colloidal solution with low particle density were similar to those from the neat dye solution. Next we presented a qualitative explanation for some of the data. The stochastic structures of the pulsed ASE spectra of neat dye solutions were observed long ago [77]. In our experimental configuration, the ASE spikes originated from the photons spontaneously emitted by the stilbene molecules near the ends of the excitation cone at the beginning of the pump pulse. As they propagated along the cone, these photons experienced the largest amplification due to their longest path length inside the gain volume. The ASE at the frequencies of these photons was the strongest,

leading to the spikes in the emission spectrum. Although the spontaneous emission time was a few nanosecond, the 25ps pump pulse created the transient gain and only the initial part of the spontaneous emission pulse were strongly amplified. Thus the ASE pulse was a few tens of picoseconds long. The spectral width of the ASE spikes was determined by the ASE pulse duration. We extracted the average width of the ASE spikes from the width of spectral correlation function in Fig. 2.16(a). After taking into account the spectral resolution of our spectrometer, we estimated the ASE pulse duration to be between 10ps and 100ps, in agreement with the pumping duration. Since different ASE spikes originated from different spontaneous emission events which were independent of each other, their frequencies were uncorrelated. It led to the Poisson statistics of the frequency spacing of neighboring ASE spikes [Fig. 2.16(b)]. Although the occurrence of ASE spikes did not rely on scattering, multiple scattering could increase the path lengths of spontaneously emitted photons inside the gain volume thus raise the amplitudes of some spikes. In our experiment, the tight focusing of the pump beam and the low particle density in the colloidal solution made the scattering mean free path exceed the size of gain volume. The effect of scattering on the ASE spikes was negligibly small, thus the ASE spikes exhibited little dependence on the particle density. The intensity of an ASE spike was determined by the amount of amplification that the spontaneously emitted photon experienced, which in turn depended on when and where the spontaneous emission happened. The optical gain varied rapidly in time and space, making it difficult to calculate the intensity statistics of the ASE spikes. Although the exponential tail of

$P(I/\langle I \rangle)$  remained to be explained, the increase of the tail at higher pumping could be understood by the larger difference in amplification of individual spontaneously emitted photons.

## 2.6 Conclusion

In this chapter, we carefully studied the laser emission from weakly scattering colloidal solutions with laser dye as gain material. First, we confirmed the observations of random lasers with resonant feedback reported previously in similar systems. The key role played by multiple scattering on lasing in weakly scattering systems was undoubtedly demonstrated, moreover, the dominant contribution from the scatterers near the system boundary on its quasimodes formation was recognized. This explained the better regularity of the quasimodes' frequencies when the system transitioned from the over-coupling regime to the under-coupling regime. Second, we clarified the difference between coherent random lasing emission peaks and stochastic amplified spontaneous emission spikes. Both occurred in weakly scattering colloidal system and shared similar spiky spectral characteristics. By comparing the emission spectrum, spectral intensity correlation, peak spacing statistics and peak height statistics side by side, we showed that these two types of emission are fundamentally different. This clarification will help people to identify random lasing phenomena more accurately. Third, we investigated the relation between the quasimodes of a random system and its lasing modes under either global or local excitation. For systems under global uniform excitation, the lasing modes have one-one

correspondence to the quasimodes of the system. When inhomogeneous local gain was introduced, the number of lasing modes was reduced from the number of quasimodes. What's more, both the frequency and wavefunction of the lasing modes can be very different from that of quasimodes, especially for weakly scattering systems. With the reduction of lasing mode number, the frequency spacing between adjacent lasing modes increased, therefore discrete lasing peaks can be observed experimentally from weakly scattering systems. However, the lasing modes can be treated as neither the quasimodes of a reduced system within the excitation region, because the feedback from outside the pumped region still exists; nor the quasimodes of the original total system without gain, because the local gain changes the relative weight between the feedback inside and outside the excitation region, which makes the lasing modes different.

## CHAPTER 3

# COHERENT RANDOM LASERS IN CLOSELY PACKED RESONANT SCATTERING ZNO SPHERES

### 3.1 Motivation

In the previous chapter, we investigated coherent random lasing from weakly scattering systems both experimentally and numerically. The study provided us better understanding for the nature of random laser phenomena. However, due to the rather weak interference effect, the random laser cavities typically had huge loss and intense excitation was required to bring the laser above its threshold. Such high threshold pump requirement poses a main challenge for wide application of random lasers. To overcome this challenge, various techniques have been proposed, e.g. external feedback with mirrors [95–97] and guiding pump light deep into the samples [98]. Besides these techniques, a more intrinsic way to lower random laser threshold is to increase the scattering strength of the media. Because the random laser feedback is from multiple scattering, stronger scattering provides better light confinement and thus a higher quality factor of the laser cavity. Both experiments and theories have confirmed that the random lasing threshold decreases with stronger scattering, and a good example is the low threshold lasing from the localized modes from a 1D random system [62]. Strongly localized quasimodes offer

good candidates for low threshold random lasing modes, and the random laser, in return, provides a handy tool to study the localized modes.

Though it has been shown that light can be localized in both 1D and 2D random systems with a finite disorder, photon localization in 3D random systems still remains an open question. To reach the localization regime, Ioffe-Regel criterion  $k_e l_s < 1$  must be satisfied, where  $k_e$  is the wavevector of light inside the system and  $l_s$  is the scattering mean free path. Therefore, both  $k_e$  and  $l_s$  should be decreased to reach the localization regime. Because  $l_s$  is inversely proportional to the scatterer concentration  $\rho$  and scattering cross section of a single scatterer  $\sigma_s$ , it is natural to seek systems which optimize both  $\rho$  and  $\sigma_s$ . Light scattering from a single scatterer is maximized at certain resonance conditions, which is called resonant scattering. A good example is the Mie resonance we discussed in the Introduction. By closely packing the resonant scatterers, we can obtain a sample which optimizes both  $\rho$  and  $\sigma_s$ . In this chapter, we investigate the light scattering and random lasing from such samples.

The chapter is organized as follows: first, we describe the synthesis process of monodisperse ZnO spheres which range in diameter from the sub 100 nm scale to over 600 nm. Such monodisperse particles are crucial to achieve the same resonant scattering for individual scatterers. A natural consequence of monodisperse spheres is the periodic opal structure formed by self-assembling, which we have successfully fabricated. The opal samples, as well as their photonic band gap (PBG) structures, will be discussed in section two. The random samples, on the other hand, are prepared by a cold pressing method

and light scattering, in particular, the coherent backscattering (CBS) measurement is investigated in section three. Then, random laser experiments from these disordered samples are presented in section four, as well as some results from numerical simulations.

### 3.2 Chemical Synthesis of Monodisperse ZnO Spheres

This section describes the procedure employed to synthesize the monodisperse ZnO nanoparticles which was developed by Seelig [100]. In principle, it is hydrolysis of zinc dihydrate,  $Zn(OOCH_3)_2 \cdot 2H_2O$  (ZnAc) in diethylene glycol,  $HOCH_2CH_2OCH_2CH_2OH$  (DEG), a process similar to that described by Jezequel et al [99]. In general, ZnAc are dissociated in the solvent and oxygen in the water bonds to  $Zn^{2+}$  ions. The protons are then removed from the structure and ZnO remains. In addition to ZnO, acetic acid is the other reaction product.

The apparatus used for the reaction is shown schematically in Fig. 3.1. The reaction was carried out in a 300 ml round-bottom flask, which was heated by a heating mantle. A reflux column was attached to the top of the flask, and cold water was flowed through the outer jacket of the column. For temperature control, a long thermocouple probe was inserted through the reflux column so that the tip of the probe was inside the flask and measures the temperature of the reaction solution. The output from the thermocouple was fed to a thermostat temperature controller. The output from the controller was sent to a variable output transformer that supplied power to the heating mantle. The power setting on the transformer was used to control the heating rate. The entire assembly

was placed on a stirring plate and reaction solution was stirred by a magnetic bar. All

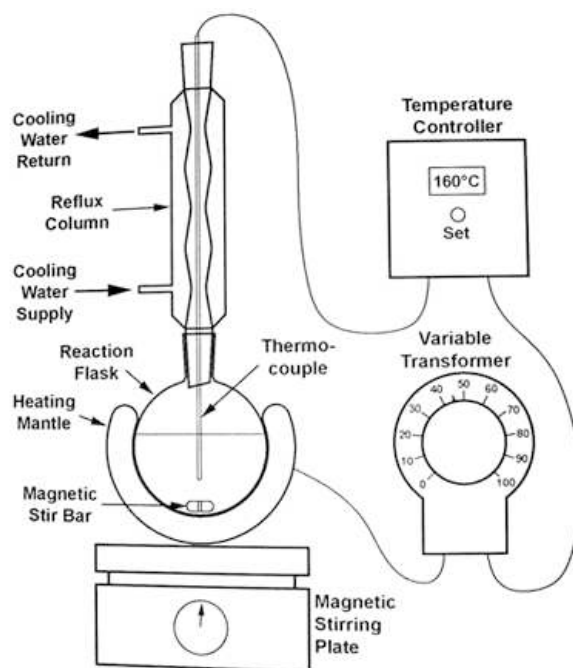


Figure 3.1: A schematic sketch of the system used for the synthesis of ZnO spheres. Cited from Ref. [100] since our systems were very similar.

reagents were used as-received with no pre-synthetic purification performed. In a typical reaction, 3.295 g  $ZnAc \cdot 2H_2O$  was dissolved in 150ml DEG solvent, and the solution was heated up while being stirred by the magnetic bar. The heating rate was  $4^\circ C/min$  till the temperature got to  $100^\circ C$ , then was slowed down to  $1^\circ C/min$  by reducing the power output from transformer. At  $150^\circ C$ , the solution started to appear cloudy which indicated the beginning of ZnO nucleation. The solution became totally white when its temperature reached  $165^\circ C$  and after that, no visible changes were observed. The setting point of temperature controller was at  $165^\circ C$ , and the solution was kept at this temperature for another hour to complete the reaction. After that, the power supply

was turned off and the flask was allowed to cool down to room temperature. ZnO powders were obtained by centrifuging the solution, and washed with iso-propanol for a few iterations of dissolving and centrifuging. Finally the clean ZnO powders were stored in iso-propanol.

The shape and size of the ZnO particles obtained from above reaction depended on the initial concentration of  $ZnAc \cdot 2H_2O$  in DEG, but in general they were polydisperse as shown in the SEM image in Fig. 3.2(a). While such polydisperse ZnO spheres proved useful for the exploration of the random lasing properties [38, 102], we still preferred monodisperse spheres for two reasons: first, the scattering resonance of every single sphere is the same in a random sample formed by packing the monodisperse spheres; second, monodisperse spheres could offer us the possibility to build periodic structures. So a revised two step reaction scheme was developed to synthesize the monodisperse ZnO spheres [101]. First, a primary reaction as described above was conducted, and the reaction solution was centrifuged to separate the ZnO powders from the supernatant. The supernatant was retained, while the polydisperse powders were discarded. Then a secondary reaction, similar as the primary reaction, was performed with only one exception: at  $150^\circ C$ , prior to the occurrence of ZnO precipitation, certain amount of primary supernatant was added into the reaction solution. A couple of things could be observed during the reaction. First, as would be expected, a temperature drop occurred scaled with the volume of room-temperature fluid added. Second, such addition resulted in precipitation occurring at lower temperatures. Visually suspensions obtained in this

two step process generally appeared whiter than that from the primary reaction.

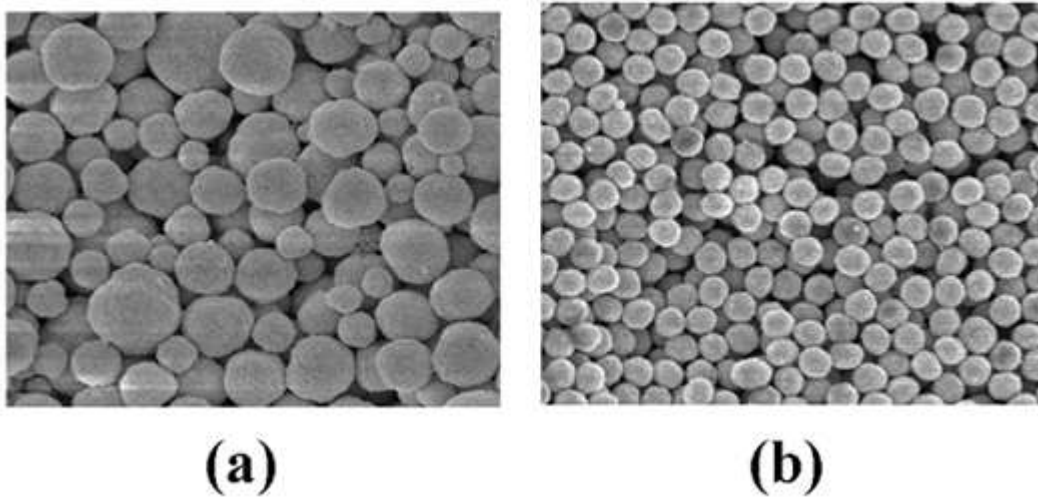


Figure 3.2: (a) SEM image of ZnO spheres obtained from a typical one step synthesis reaction. (b) SEM image of monodisperse ZnO spheres obtained from a revised two step synthesis reaction. Both images are with the full scale of  $4 \mu m$ .

SEM images of these powders revealed that they were monodisperse spherical particles, as shown in Figure 3.2(b). Careful size analysis showed that the diameter deviation was within 6%, and the relative deviation was usually smaller for larger spheres. Precise control of the size of the ZnO spheres was realized by controlling the volume of primary supernatant added [101], where best fitting showed a relation of the form  $d = kx^{-1/3}$ , where  $d$  was the mean sphere diameter,  $x$  the volume of primary supernatant added, and  $k$  a fitting constant. Changing from sphere diameter to sphere volume  $v$ , the relation became  $v = k'x^{-1}$ , which can be understood as following: if we assume the total volume of ZnO formed in the secondary reaction was a constant, then the individual particle volume should be inversely proportional to the number of particles  $N$ , while  $N$  was determined by the number of nucleation center in the added primary supernatant, which

was proportional to its volume.

High resolution SEM and XRD measurements both confirmed that the monodisperse as-grown ZnO spheres were not single crystalline spheres, but porous powders formed by many tiny ZnO single crystal grains. So the effective refractive index of such sphere needed to be determined instead of using bulk ZnO value. It was obtained by the transmission measurement of the opal structures formed by the ZnO spheres, which will be discussed in next section.

### 3.3 Self-Assembly and Optical Calibration of ZnO Opal Structures

We have managed to produce periodic opal structures from the as-made ZnO monodisperse spheres by using an evaporation-induced self-assembly process [101]. In most cases, a small amount of the colloidal reaction solution was dropped on a substrate (glass or Si), and allowed to dry. Because of the low vapor pressure of the solvent (DEG), the drying process was assisted by placing the substrate on a hot plate. The substrate temperature was set between  $160^{\circ}C$  and  $220^{\circ}C$  to get best structure qualities. Samples made in this range showed visible bright single color reflections, which was a sign of a good periodicity in the opal structure. Samples made at lower temperatures appeared as uniform layers and exhibited no bright reflection; while samples deposited at higher temperatures adhered poorly to the substrate. SEM images showed that well aligned FCC opal structure were obtained by this simple method with their  $\langle 111 \rangle$  direction normal to the

substrate, as shown in Fig. 3.3. Though the self-assembly method was simple, there

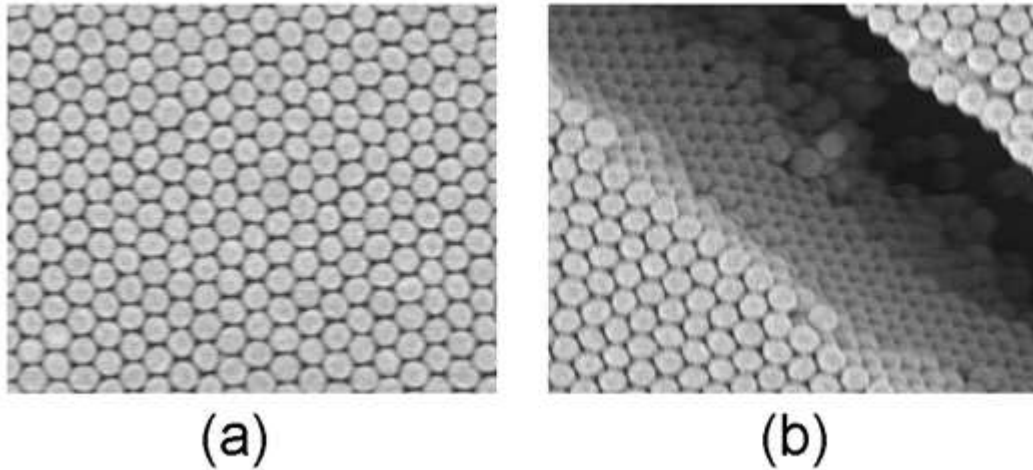


Figure 3.3: Top view (a) and side view (b) SEM images of FCC structure formed by self-assembly of monodisperse ZnO spheres obtained from two step synthesis reactions. Both images are with full scale of  $4 \mu m$ .

were some requirements one needed to follow. First, it was shown that only the as-made reaction solution should be used to get the periodic opal structures. After the solution was centrifuged and ZnO spheres were dispersed in other solvents like iso-propanol, DEG or methanol, periodic structures could not be obtained by the evaporation method. This showed that the as-made reaction solution was a stable ZnO colloidal suspension caused by the surface charges on each ZnO sphere, and such charges were removed when other solvents were used. Second, the substrate had to be hydrophobic to the colloidal solution. This could cause the formation of a meniscus and generated surface tension to force the spheres to align periodically. If the solution was wetting the substrate, no periodic structures were observed.

There were a few limitations on this self-assembly method. One limitation was the

sample thickness. Typically one drop of as-made solution generated a sample with thickness about  $2 - 3\mu m$ . In order to observe the photonic crystal behavior, it was generally necessary to have 10-20 layers of spheres. While  $2 - 3\mu m$  was thick enough to accommodate enough layers of small spheres, larger spheres, in the 300-600 nm range, may have too few layers to show the photonic crystal behavior. To increase the thickness, we centrifuged the solution first and removed some fraction of the supernatant, so the solution left had higher concentration and allowed to form a thicker opal structure. The other limitation was that the produced opal structure was not a single domain structure in the lateral direction, which was usually a few millimeters. In stead, many domains with size smaller than  $100\mu m$  were formed, separated by cracks from each other. However, while the lateral orientation of each domain was different, the vertical orientation was always along  $\langle 111 \rangle$  direction, which was exactly the direction we were interested in.

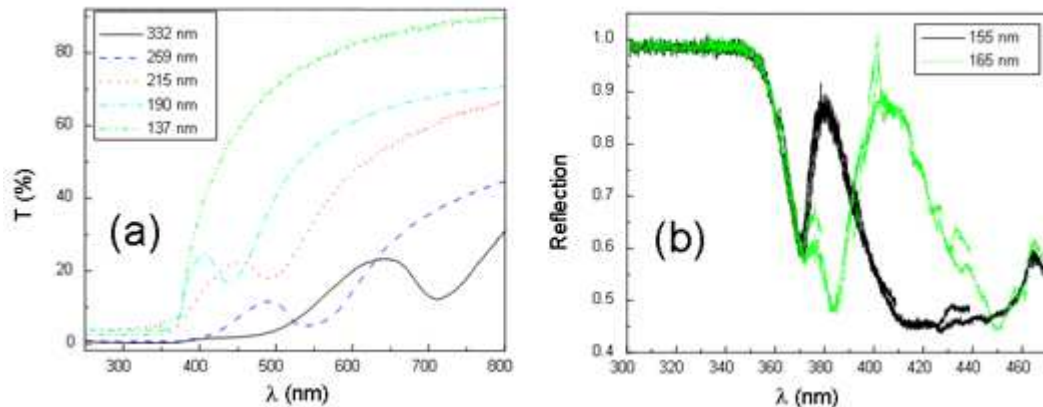


Figure 3.4: (a) Large area normal incidence transmission spectra of ZnO opal along  $\langle 111 \rangle$  direction for ZnO opals with five different sphere sizes. (b) Reflection spectrum of ZnO opal along  $\langle 111 \rangle$  direction for two different sphere sizes.

Large area normal incidence transmission measurement along  $\langle 111 \rangle$  direction was

$d(\text{nm})$	$\lambda(\text{nm})$	$d/\lambda$
137		
155	381	0.407
165	404	0.408
190	437	0.435
215	493	0.436
255	551	0.463
332	714	0.465

Table 3.1: Relation between ZnO sphere diameter and photonic band gap position.

performed with the ZnO opal samples and the results are plotted in Fig. 3.4(a). As expected, it clearly shows that the bandgap center wavelength scaled with the sphere diameter in ZnO opal structures. With the ZnO sphere size changing from 100 nm to 600 nm, the bandgap can be tuned from UV to IR regime, covering the entire visible spectral range. For opal structures formed with small spheres, the bandgap was below ZnO absorption edge (around 385 nm) and was not visible in transmission due to strong absorption. To overcome this issue, reflection spectra were measured instead along  $\langle 111 \rangle$  direction. Normal incident white light was focused by an objective lens and the reflected light was collected by the same lens. Figure 3.4(b) shows the reflection spectra for two opal structures formed with small ZnO spheres, where a reflection peak close to ZnO absorption edge was clearly observed.

To show the photonic behavior more clear, the ZnO sphere diameter  $d$ , the center wavelength of bandgap  $\lambda$  and their ratio  $d/\lambda$  are listed in Table 3.1. It can be seen that  $d/\lambda$  gradually decreases  $d$  and  $\lambda$ . This was expected since ZnO refractive index increases when  $\lambda$  approaches the absorption edge from the long side, and  $d/\lambda$  should be inversely proportional to the refractive index of ZnO opal according to Bragg reflection relation. To

get more accurate results, we calculated the band structure of our ZnO opals using MPB package from MIT [103]. By calculating band structures for ZnO opals with different refractive index values and fitting the calculation with experimental data, we determined the refractive index of the ZnO spheres. Figure 3.5(a) shows a plot of gap position ( $a/\lambda$ ) as a function of the refractive index  $n$  and the radius to interparticle distance ratio ( $r/d$ ). For  $n = 2.1$  (the approximate bulk value for ZnO), the map indicated that  $a/\lambda$  should be around 0.35, while our experimental obtained value was close to 0.45. This discrepancy implied that the effective index of ZnO spheres were significantly smaller than the bulk value. Restricting the packing parameter  $r/d$  to 0.45-0.50 as confirmed by SEM images and keeping  $d/\lambda = 0.45$ , Fig. 3.5(a) yielded an refractive index in between 1.5-1.7. Using this refractive index and  $r/d$  range, Fig. 3.5(b) predicted the gap width was about 5.5 – 7.8%. The fact that the refractive index of ZnO sphere was smaller than that of bulk ZnO indicated that these spheres were porous. The porosity of ZnO spheres was estimated from Maxwell-Garnett equation:

$$\epsilon_e = \epsilon_1 \left( \frac{2\epsilon_1 + \epsilon_2 + 2f(\epsilon_2 - \epsilon_1)}{2\epsilon_1 + \epsilon_2 - f(\epsilon_2 - \epsilon_1)} \right), \quad (3.1)$$

where  $\epsilon_1 = 1$  for air and  $\epsilon_2 = 4.24$  for bulk ZnO at  $\lambda = 500$  nm. Then for  $\epsilon_e = 1.7^2 = 2.89$ , we derived that the filling fraction  $f$  of bulk ZnO inside the sphere was around 70%.

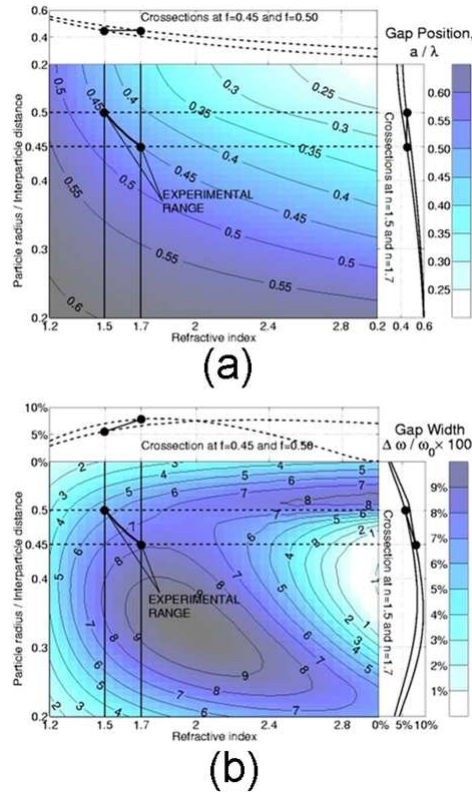


Figure 3.5: (a) Photonic band gap position ( $a/\lambda$ ) and (b) photonic band gap width ( $\Delta\omega/\omega_0 \times 100$ ) as a function of effective refractive index of the spheres  $r/d$ . The approximate experimental range is indicated on each plot.

### 3.4 Coherent Backscattering of Light in Random Samples Formed by Closely Packed Resonant ZnO Spheres

In previous section, we discussed the fabrication of the periodic opal structures from monodisperse ZnO spheres. In this section, we will discuss another sample made of ZnO spheres: random structures. Though the evaporation method introduced in last section can also generate random samples at low temperatures, we prepared random samples by a different way. First, ZnO powders were separated from the supernatant by centrifuging, then they were washed with iso-propanol a few times and finally dry ZnO powders were

obtained by evaporating iso-propanol at a high temperature. To achieve maximum gain in our sample, we cold-pressed ZnO spheres with a pressure of 150 MPa to form tablets with diameter 7.87 mm and thickness 1.40 mm. Since we used the same amount (0.17 g) of ZnO powders and made the tablets of the same volume, the densities  $\rho$  of all the tablets made of different diameter spheres were the same. The bulk ZnO filling factor of all the tablets was derived by  $\rho/\rho_0 \sim 45\%$ , where  $\rho_0 = 5.6\text{g}/\text{cm}^3$  was the density of ZnO bulk crystal. From the previous section we already knew that the ZnO spheres were porous with bulk ZnO crystal volume fraction about 70%. Therefore, the volume fraction of the ZnO spheres in the tablet was estimated to be around 60%. This number confirmed that ZnO spheres were closely packed. Unlike sedimentation, our process of packing ZnO spheres was so fast that the spheres should have no time to arrange themselves into ordered structures. Therefore, ZnO spheres were randomly positioned in those tablets.

To calibrate the scattering strength in these random samples, we needed to measure the transport mean free path  $l_t$ . Since our samples were too thick for transmission measurement, we conducted coherent backscattering (CBS) measurements to obtain the transport mean free path  $l_t$ . The experiment setup was following: the collimated probe beam passed an electric chopper, reflected from a beamsplitter onto the sample surface with a 4 mm spot. The sample was mounted on a stage which spun at  $\sim 100$  rpm around the axis normal to the sample surface. The incident probe beam was deviated from the normal direction to avoid the specular reflection. The PMT detector was put on an arm which rotated exactly around the incident spot on the sample surface horizontally with

an angular step controlled by a step motor. The detection arm was carefully screened to remove the streak light and a lock-in amplifier was used in combination with the chopperto enhance the signal to noise ratio. The angular resolution of the system was determined by the ratio between the detection area of the PMT, which was controlled by an aperture right in front of it, and the radial distance from the sample surface to the detector. The angular resolution in our CBS system was less than  $0.1^\circ$ , thus the scanning step size was set to be  $0.1^\circ$  and  $0.2^\circ$  depending on the CBS cone width from different samples. Since we planed to perform lasing experiments with those ZnO samples,  $l_t$  at the wavelength of ZnO maximum gain (385 nm) was desired. However, it could not be done due to the strong absorption of the probe light at such frequency. Instead, we measured  $l_t$  at three different probing wavelengths longer than 385nm: a CW HeNe laser ( $\lambda = 633$  nm), a mode-locked Ti:Sapphire laser ( $\lambda = 793$  nm), and the second harmonics of the Ti:Sapphire laser ( $\lambda = 400$  nm). Based on these data, we expected to find a general trend for  $l_t$  on  $\lambda$  and estimate its value at the wavelength we were interested. As an example, Fig. 3.6 shows the CBS cones from one sample with the three different probing wavelengths.

We derived the transport mean free path  $l_t$  from the full width at half maximum (FWHM) of the CBS cone  $\Delta\theta$  using the following formula:

$$l_t = \frac{\lambda}{2\pi\Delta\theta(1 + z_e)} \quad (3.2)$$

where  $z_e$  is the extrapolated length ratio [104]. We assumed that  $z_e$  only depended on

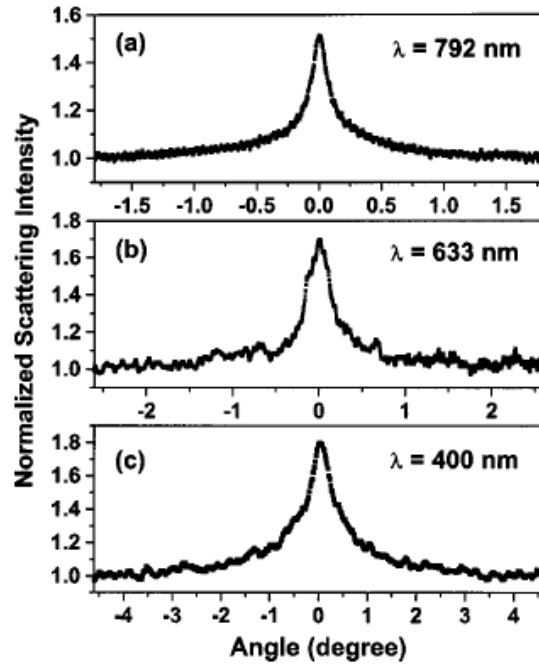


Figure 3.6: (CBS cones for sample made of ZnO spheres of 233 nm with three different probing wavelengths.

the overall reflectivity  $R$  at the sample-air interface, i.e.,  $z_e = 2(1+R)/3(1-R)$ , where  $R$  was determined by the effective refractive index  $n_{eff}$  of the sample [104]. Figure 3.7(a) shows the transport mean free path  $l_t$  versus the ZnO particle diameter  $d$  at three different probe wavelengths. First, it can be seen that for all three different  $\lambda$ , the transport mean free path  $l_t$  varied similarly with  $d$ . When  $d$  increased,  $l_t$  first decreased rapidly and then saturated. For  $\lambda = 400 \text{ nm}$ ,  $l_t$  decreased from  $4.4 \mu\text{m}$  at  $d = 85 \text{ nm}$  to  $0.6 \mu\text{m}$  at  $d = 172 \text{ nm}$ .  $l_t$  was over 7 times shorter for only 87 nm change of the sphere diameter. For  $\lambda = 633 \text{ nm}$ ,  $l_t$  decreased from  $19.5 \mu\text{m}$  at  $85 \text{ nm}$  to  $3.1 \mu\text{m}$  at  $299 \text{ nm}$ , over 6 times shorter for about 200 nm change of  $d$ . For  $\lambda = 793 \text{ nm}$ ,  $l_t$  decreased from  $25 \mu\text{m}$  at  $114 \text{ nm}$  to  $3.3 \mu\text{m}$  at  $355 \text{ nm}$ , about 8 times shorter after 240 nm change. So the decreasing was most abrupt for  $\lambda = 400 \text{ nm}$ . Though  $l_t$  behaved very differently for these three

different  $\lambda$ , when we replotted the same data in a normalized way:  $l_t/d$  vs.  $n_{eff}d/\lambda$ , the three curves became one. This universal behavior can be roughly understood as follows: in Rayleigh scattering regime,  $l_t = 1/\rho\sigma_{sc}$  (assuming  $l_t = l_{sc}$ , which is satisfied in Rayleigh scattering regime), where  $\rho = 1/V = (\pi d^3/6)^{-1}$  is the concentration of scatterers and  $V$  is the volume of one single scatterer, and  $\sigma_{sc} \propto V^2\lambda^{-4} \propto d^6\lambda^{-4}$ , thus  $\rho\sigma_{sc} \propto d^3\lambda^{-4}$ , then easily  $l_t/d \propto (d/\lambda)^4$ . If we assume that the refractive index does not change with wavelength, then  $l_t/d \propto (nd/\lambda)^4$ , which is roughly satisfied for ZnO spheres at the three wavelengths we tried experimentally. Indeed such dependence was found for samples made of small ZnO spheres in our experiments as shown in Fig. 3.7 (b). For larger spheres, resonance occurs in Mie scattering regime as we discussed in Introduction. Remember that in Mie theory, scattering efficient  $Q_{sc}$  depends on three parameters:  $x = \pi r/\lambda$ , refractive index ratio between scatterer and surround media  $m$ , and  $y = mx$  [3]. Now if we assume  $m$  is  $\lambda$  independent, then  $Q_{sc}$  is determined purely on either  $x$ , as we showed in Fig. 1.1, or  $y$ . Now remember that  $\sigma_{sc} = Q_{sc}\pi r^2$  and  $\rho = 1/V = (\pi d^3/6)^{-1}$ , thus it can be easily derived that  $l_t/d$  only depends on  $y$ , which explains the universal behavior shown in Fig. 3.7 (b).

Following the above discussion, one would expect that the multiple scattering in the samples made of the monodisperse spheres should behave similarly as scattering from a single sphere. In particular, those resonances in  $\sigma_{sc}$  should also appear in  $l_t$  with varying  $y$ . However, no resonances were observed experimentally in our samples as shown in Fig. 3.7. This discrepancy was caused by our assumption of independent scattering in

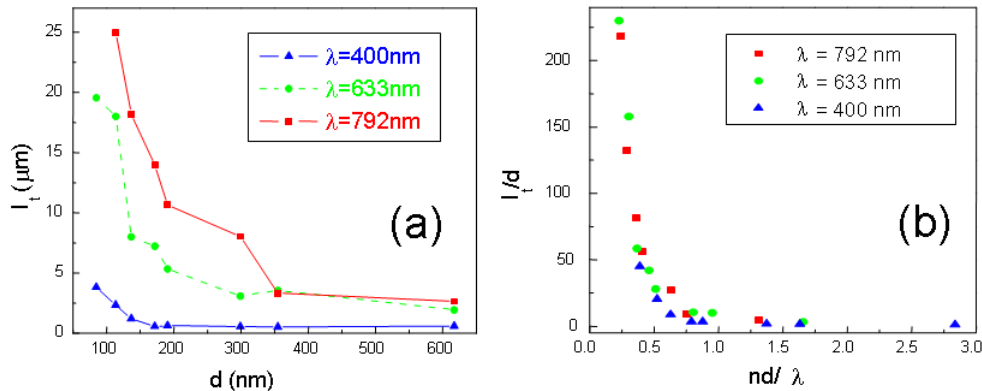


Figure 3.7: (a) Transport mean free path  $l_t$  versus ZnO sphere diameter  $d$  at wavelengths.  $\lambda = 400\text{ nm}$  (triangle),  $\lambda = 633\text{ nm}$  (circle), and  $\lambda = 793\text{ nm}$  (square). (b) the same data from (a) plotted as  $l_t/d$  versus  $n \cdot d/\lambda$ .

above consideration, which did not hold in our closely packed sample any more. When the scattering cross section of neighboring sphere began to overlap, dependent scattering became important and light propagation could no longer be regarded as a sequence of scattering events from one particle at a time. In our samples made of ZnO monodisperse spheres, the scattering from single sphere became stronger for larger sphere sizes, where Mie resonance enhanced the scattering cross section  $\sigma_{sc}$  from individual sphere and neighboring  $\sigma_s$  began to overlap and dependent scattering occurred. One straightforward approach to improve in this regime is to calculate the second-order correction in density  $\rho$ . This turned out to be a difficult task; exact calculations could only be performed for a Gaussian fluctuation model of correlated disorder [105]. This model, well suited for the porous silica sample of Ref. [105], may not give all the structures that resulted from the sample of the monodisperse spheres considered in our experiments.

Another highly accurate approximation widely used for calculating  $l_{sc}$  is the coherent

potential approximation (CPA) [106]. Within the CPA one calculates the effective dielectric constant (its imaginary part is related to  $l_{sc}$ ) of the medium, taking into consideration the microstructure of the system. For the monodisperse spheres, one considers a single sphere surrounded by an air shell embedded in the effective medium. Self-consistency requires the disappearance of scattering in the forward direction. To determine the transport mean free path, Busch *et al* proposed to calculate  $\sigma_t = \int \sigma_{sc}(\Omega)(1 - \cos\theta)d\Omega$  for the CPA unit, where the integral of the solid angle is taken [5]. Comparing this expression with equations for independent scattering, one can see that this is an extension of the weak scattering formula into the strong-scattering regime, replacing the real single scatterer by an effective scatterer.

In the strong-scattering regime CPA calculations with needed corrections become increasingly complicated and computationally heavy. Recently, it has been proposed to use truncated multipole expansions to solve the multi-sphere problem (see Ref. [107] and references therein). Within this generalized multi-sphere Mie (GMM) solution one expands the electric field inside and outside of each sphere in vector spherical harmonics, then, the field incident on a sphere is a sum of the incoming plane wave and fields scattered by all other spheres. By matching the boundary conditions on the sphere surfaces one obtains a linear system on the spherical harmonic coefficients, which is solved by recursion [107]. In order to obtain scattering coefficients one adds up the individual scattered fields in far-field zone. Computation time strongly depends on the size parameter  $x$ , as the number of multipoles needed for convergence increases with  $x$ .

Similar to Busch *et al* [5], we define  $l_{sc}$  and  $l_t$  in the strongly scattering regime as the formula for independent scattering, but instead of CPA-based calculations of  $\sigma_{sc}(\omega)$  and  $\langle \cos(\theta) \rangle$  we calculate these quantities for the individual spheres inside the finite clusters. More precisely, we (i) generate (10 realizations) clusters of 5 or 10 randomly arranged dielectric spheres with filling fraction  $f \simeq 0.5$ ; (ii) solve the scattering problem using GMM code; (iii) find  $\sigma_{sc,i}(\omega)$  and  $\langle \cos(\theta_i) \rangle$  for each sphere in the cluster, averaged over 24 angular orientations of the cluster and 2 polarizations of the incident field; (iv) compute average  $\sigma_{sc}(\omega)$  and  $\langle \cos(\theta) \rangle$  over all spheres in the cluster and 10 random configuration. To match our experimental set-up, we have chosen the spheres with refractive index  $n = 1.7$  and  $n \cdot d/\lambda \in [0, 4]$ . We should stress that our calculations become incorrect when  $l_{sc}$  becomes larger than the size of the cluster, which restricts  $y = n \cdot d/\lambda > 1$ . This is, however, the region where a weak scattering approximation described in the beginning of this section, gives reliable results. Therefore, the combination of weak scattering approximation with the cluster-based calculation gives the continuous coverage for practically all values of  $y$ .

The results of the calculations outlined above are presented on Fig. 3.8 and 3.9. The inset of Fig. 3.8 shows a significant modification of the scattering efficiency of the particles in the cluster. This is due to interaction between particles. When the resonant scatterers with scattering cross sections larger than geometrical cross section, are packed closely together, the hybridization due to interaction (dependent scattering) occurs. As a result the  $\langle \sigma_{sc} \rangle / \sigma_g$  saturates at about  $f^{-2/3}$  - square of the average (dimensionless) distance

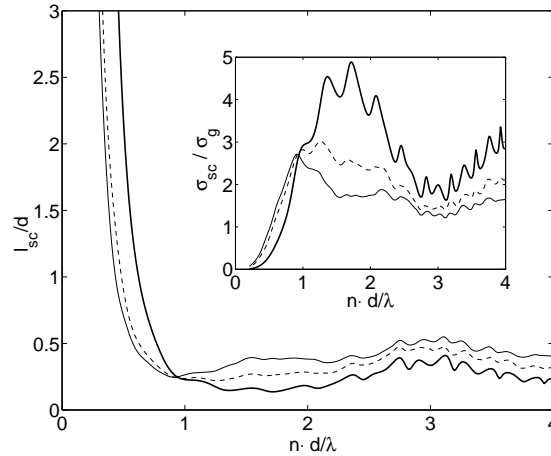


Figure 3.8: Scattering mean free path  $l_{sc}$  normalized by the sphere diameter  $d$ , calculated for clusters of 5 (dashed line) and 10 (solid line) spheres, as a function of normalized particle size  $n \cdot d/\lambda$ . The bold line represents  $l_{sc}$  calculated within independent scattering approximation. Inset shows the scattering efficiencies  $\sigma_{sc}/\sigma_g$  of a stand-alone single sphere (bold line), and a sphere in the clusters of 5 (dashed line) and 10 (solid line) particles.

between scatterers. When such saturation occurs,  $l_{sc}^{-1} \simeq \rho f^{-2/3} \sigma_g \propto (d f^{-1/3})^{-1}$ .

Normalized by the particle size  $l_{sc}/d$  appears to be a constant as it can be seen from Fig. 3.8. The residual structure can be traced back to the single particle resonances and would probably not survive a small size dispersion - inevitable in the experiment.

In the inset of Fig. 3.9, we plotted  $[1 - \langle \cos(\theta) \rangle]^{-1}$  for a particle in a cluster. The first obvious feature is that the scattering within the cluster is highly anisotropic. This may be attributed to the fact that many scatterers lie close to boundary and may not “feel” the local environment as those inside the cluster. We, however, did not notice any systematic difference in  $\langle \cos(\theta) \rangle$  for these two types of particles. Another important consequence of combining  $l_{sc}$  and  $\langle \cos(\theta) \rangle$  in expression of  $l_t$ , is the disappearance of most of irregular structure inherited from  $l_{sc}$ . Indeed,  $l_t$  is strikingly smoother function

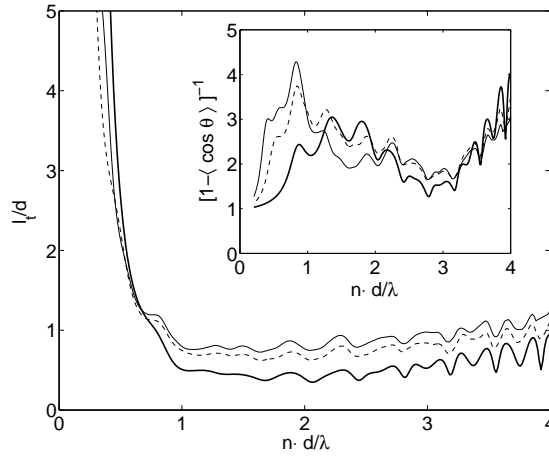


Figure 3.9: Transport mean free path  $l_t$  normalized by the sphere diameter  $d$ , calculated for clusters of 5 (dashed line) and 10 (solid line) spheres, as a function of normalized particle size  $n \cdot d/\lambda$ . The bold line represents  $l_t$  calculated within independent scattering approximation. Inset shows  $\langle \cos(\theta) \rangle$  of a stand-alone single sphere (bold line), and a sphere in the clusters of 5 (dashed line) and 10 (solid line) particles.

of the particle size, which reproduces well the experimentally observed situation reported in the previous section. The similarity between  $l_t$  calculated for the clusters of 5 and 10 spheres and the fact that  $l_t$  is smaller than the cluster size demonstrate that we capture the most important effects due to dependent scattering. Even though the calculations extended to larger clusters would improve our results, it should not, however, change it significantly. The absence of systematic difference in scattering properties between the particles in the cluster further confirms our conclusion.

### 3.5 Lasing in Random Samples Formed by Closely Packed

#### Resonant ZnO Spheres

In the lasing experiment, the samples were optically excited by the third harmonics of a mode-locked Nd:YAG laser ( $\lambda = 355$  nm, 10 Hz repetition rate, 20 ps pulse width). The pump beam was focused to a spot on the sample surface at normal incidence. The emission was collected by the same focusing lens and the spectra were measured by a spectrometer with 0.13 nm spectral resolution. As shown in Fig. 3.10, at low excitation intensity, the spectrum had a single broad spontaneous emission peak. As the pump intensity increased, the emission peak was gradually narrowed due to amplification of spontaneous emission (ASE). When the excitation intensity exceeded a threshold, extremely narrow peaks emerged around 375 nm. With a further increase of the pump intensity, more sharp peaks appeared.

Figure 3.11 is a plot of the lasing threshold pump intensity versus the ZnO sphere diameter for two different pump area sizes. When the diameter of excitation spot was changed from 8  $\mu\text{m}$  to 16  $\mu\text{m}$ , the lasing threshold exhibited similar dependence on the sphere size. There are two distinct features in Fig. 3.11: (1), the threshold pump intensity remains nearly constant for a wide range of sphere diameter from 137 nm to 617 nm; (2), with a small decrease of sphere diameter from 137 nm to 114 nm, the lasing threshold increases dramatically, especially for smaller pump area. For the sample of 85 nm spheres, we could only observe ASE but not lasing. The lasing threshold pump intensity for larger pump area is lower than that for smaller pump area, that is consistent

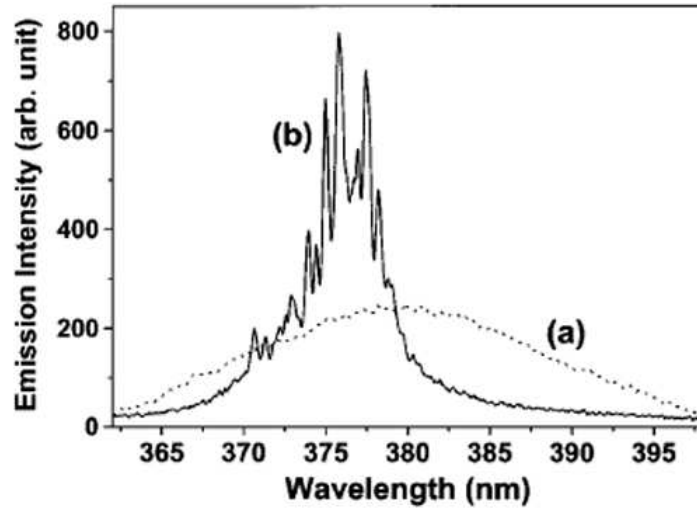


Figure 3.10: Measured spectra of emission from a ZnO pellet. The mean diameter of the ZnO spheres is 617 nm. The pump beam spot on the sample surface is  $8 \mu\text{m}$  in diameter. The incident pumping intensities are (a)  $6 \text{ MW}/\mu\text{m}^2$  and (b)  $11 \text{ MW}/\mu\text{m}^2$ . The integration times are (a) 15 and (b) 3 s.

with our previous finding [40].

The lasing threshold varied as we excited different part of the same sample. In fact, the lasing thresholds shown in Fig. 3.11 are the mean values of threshold pump intensities. The statistical fluctuation of lasing threshold is an important character of random laser. To fully understand random laser behavior, we measured the variance of lasing threshold pump intensities. The nonuniformity of a sample formed of polydisperse scatterers led to fluctuation of the scattering length across the sample, and it added an artificial variation to the intrinsic variation of random lasing threshold. Using monodisperse ZnO spheres, we were able to make uniform random samples. Experimentally, we shifted the pump spot across the sample and recorded the lasing threshold pump intensity  $I_{th}$ . The diameter of the excitation spot was kept constant. Then we calculated the mean value  $\langle I_{th} \rangle$  and

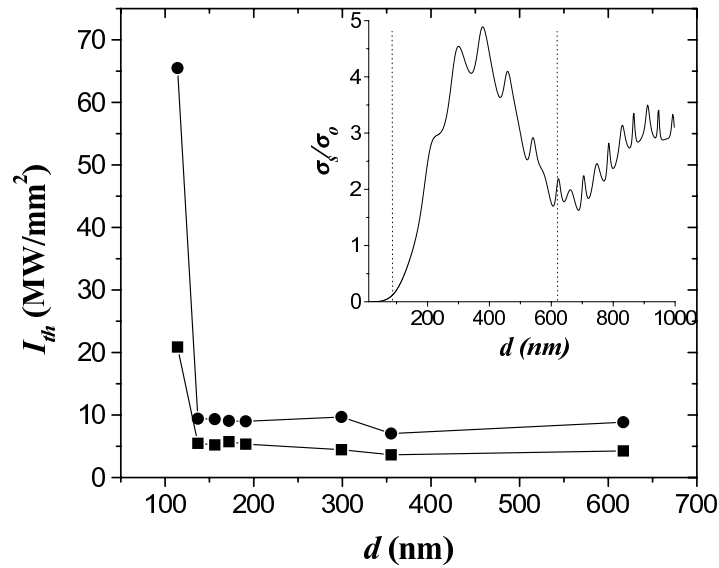


Figure 3.11: The incident pump intensity at lasing threshold  $I_{th}$  versus ZnO sphere diameter  $d$ . Squares and circles correspond to the pump spot diameter of  $8 \mu\text{m}$  and  $16 \mu\text{m}$  respectively. Inset shows normalized scattering cross section  $\sigma_{sc}/\sigma_g$  of single ZnO sphere as a function of its diameter  $d$  with parameters  $n = 1.7$  and  $\lambda = 375 \text{ nm}$ .

its standard deviation  $std(I_{th}) = \sqrt{\langle (I_{th} - \langle I_{th} \rangle)^2 \rangle}$ . The normalized standard deviation  $\delta\gamma/\langle\gamma\rangle = std(I_{th})/\langle I_{th} \rangle$ . We found experimentally that the variance for 400 threshold data has the same value as that for 200 data. Therefore, 200 threshold data were used to get the variance of lasing threshold. Table 3.2 lists some of our experimental results. The standard deviation of lasing threshold decreased with an increase of sphere diameter  $d$ . However, for the largest  $d$ , it increased slightly. As discussed earlier, in the pellets composed of larger ZnO spheres, shorter  $l_t$  resulted in smaller lasing cavities. Within a constant pump area there are more random laser cavities available. The improved “averaging” within the pump area leads to smaller fluctuation of the lasing threshold. This explains the decrease of the deviation of lasing threshold with the increase of sphere diameter  $d$ . Typically there are many spheres within the pumped region. Although the

$d(\text{nm})$	$l_t(\mu\text{m})$	$\langle I_{th} \rangle (\text{MW}/\text{mm}^2)$	$std(I_{th}) (\text{MW}/\text{mm}^2)$	$\delta\gamma/\langle\gamma\rangle (\%)$
137	1.21	20.8	3.5	17
172	0.58	19.1	2.0	11
299	0.55	19.6	1.5	8
355	0.53	16.8	1.2	7
617	0.61	17.4	1.7	10

Table 3.2: Fluctuation of lasing threshold in different samples with 5  $\mu\text{m}$  pump area.

particle configurations change with the pump positions, different pump regions of the same sample are statistically equivalent. However, when the ZnO spheres are as large as 617 nm, the number of spheres within the pumped region is rather small. At different pump positions, the number of spheres and their configuration can be quite different. This may cause more fluctuation in lasing threshold. To test the above explanation, we increased the pump area to 15  $\mu\text{m}$  in diameter, and measured the variance of lasing threshold for two samples ( $d = 137$  nm and  $d = 299$  nm). The normalized deviation for the  $d = 137$  nm sample is  $\delta\gamma/\langle\gamma\rangle = 11\%$ . It is larger than 7% deviation of the  $d = 299$  nm sample that has shorter  $l_t$ . We also compared the fluctuation of lasing threshold for the same sample at different pump diameter  $s$ . For  $d = 137$  nm,  $\delta\gamma/\langle\gamma\rangle = 17\%$  at  $s = 5$   $\mu\text{m}$ . It is larger than  $\delta\gamma/\langle\gamma\rangle = 11\%$  at  $s = 15$   $\mu\text{m}$ . In smaller pumped region, fewer random laser cavities are available, leading to larger threshold fluctuation. For  $d = 299$  nm, the two deviations are similar,  $\delta\gamma/\langle\gamma\rangle = 8\%$  at  $s = 5$   $\mu\text{m}$  and  $\delta\gamma/\langle\gamma\rangle = 7\%$  for 15  $\mu\text{m}$ . This may be due to accuracy of our threshold measurement. Because of the power fluctuation of our pump laser, we could not resolve small difference in threshold fluctuation. We simulated random laser behavior numerically by using FDTD method [86]. Due to the computation burden of 3D system, we performed the calculation in 2D system. To

determine the lasing threshold we will assume that it is solely determined by the mode of the lowest radiative loss - highest quality factor  $Q_m$ . This is a simplification that neglects non-uniformity of the gain in the system. We believe, however, that qualitative dependence should not be affected by this assumption. The system under consideration is 2D array of passive dielectric rods with refractive index  $n = 2.2$  and filling fraction of 0.5. When changing the size (diameter) of the rods  $n \cdot d/\lambda_0 \in [0.2, 2]$ , we kept the physical size of the system constant  $2 \mu\text{m} \times 2 \mu\text{m}$ , with wavelength  $\lambda_0 = 375 \text{ nm}$ . To determine the quality factor of the least leaky mode, we launched a pulse with the bandwidth of about 10 nm centered at  $\lambda_0$ . After initial excitation the modes in the excited frequency region decayed with time. After a sufficient time only one mode with the highest  $Q$  dominated the spectrum. This was evidenced by the stabilized field distribution in the sample. In this regime the total energy stored in the system followed a single exponential decay with time:  $\mathcal{E} \propto \text{Re} [\exp 2i\omega_m(1 + i/2Q_m)t]$ . From this dependence the frequency  $\omega_m$  and the quality factor  $Q_m$  were determined with a Fourier transform. Since the lasing threshold is inversely proportional to the maximum  $Q$ , we define the lasing threshold in our system as  $\gamma \equiv 1/Q_m$ . For 100 disorder realizations we calculated mean value of lasing threshold  $\langle \gamma \rangle$ , and its standard deviation  $\delta\gamma$ . In order to make the comparison with experiments done in 3D, we performed calculations for both TM (E-field parallel to the cylinder axis) and TE (H-field parallel to the cylinder axis). It can be shown that Maxwell equations for TM polarization are equivalent to scalar equations. For this reason it is sometimes called  $s$ -polarization as opposed to  $p$ - or TE polarization. In the latter two components

of electric field are available which brings them closer to the 3D case.

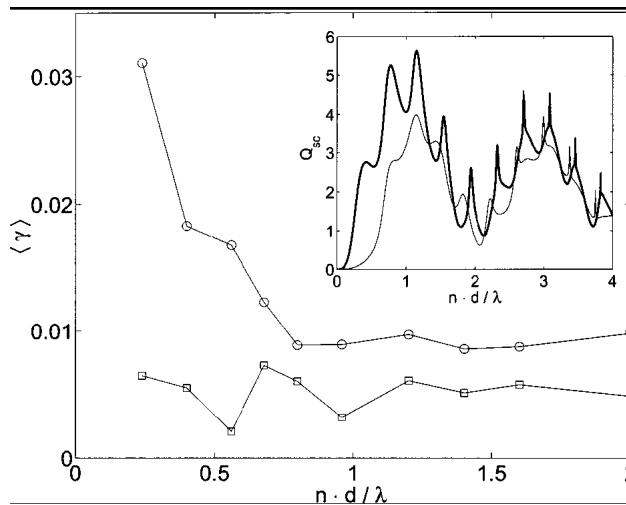


Figure 3.12: Average lasing threshold  $\langle \gamma \rangle = \langle 1/Q \rangle$  as a function of the dimensionless particle size. Squares and circles represent TM and TE polarizations respectively. Error bars are too small to be shown on the plot. Inset shows scattering efficiency of a dielectric cylinder with  $n = 2.2$  for TE (thin line) and TM (thick line) polarizations vs the dimensionless diameter.

Squares on Fig. 3.12 and 3.13 show the results for TM polarization. One can see that there exist 3 minima of lasing threshold at  $n \cdot d/\lambda = 0.6, 1, 1.4$ . As the values of  $\delta\gamma$  remain about the same (Fig. 3.13), it would lead to sharp peaks of  $\delta\gamma/\langle \gamma \rangle$ . These peaks can be shown to be related to the band gap of the order sample with the same filling ratio [108]. Apart from band gap related minima of  $\langle \gamma \rangle$ , and more relevant to the current discussion, the threshold dependence on size is featureless. The threshold is almost constant with no increase at the small particle size. This is in contrast to the experimental result reported earlier in the paper and to the numerical calculation for TE polarization in Fig. 3.12. Indeed, TE polarization does show a drastic decrease of  $\langle \gamma \rangle$  at  $n \cdot d/\lambda \simeq 0.5$ , which is similar to the characteristic size in both experiment and 3D

theoretical prediction for  $l_t$ . Naturally the question arises “Why TM polarization shows such remarkable difference?”.

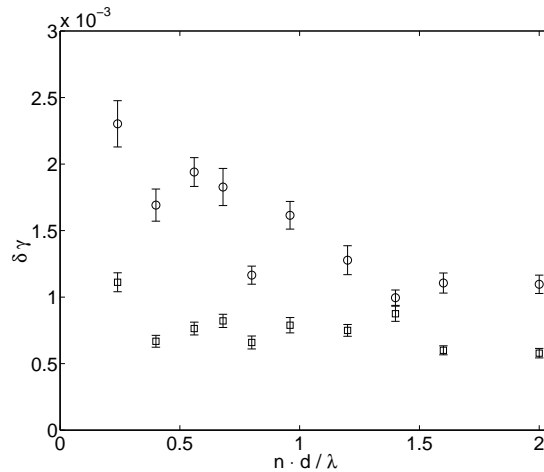


Figure 3.13: Standard deviation of lasing threshold  $\delta\gamma$  as a function of the dimensionless particle size. Squares and circles represent TM and TE polarization respectively.

To answer the above question, we plotted the scattering efficiency,  $Q_{sc} = \sigma_{sc}/\sigma_g$  (not to be confused with cavity  $Q$ ), for a single cylinder in inset of Fig. 3.12. Thin and bold lines represent TE and TM polarization respectively. One can see the significant difference in the characteristic particle size where  $Q_{sc}$  increases above one. This size is, in fact, when the weak Rayleigh scattering fails and one has to account for the interactions between the particles. For TM modes the increase in the lasing threshold (as well as  $l_t$ ) should occur at  $n \cdot d/\lambda \simeq 0.2$ , incidentally, this is the smallest value that we could reach numerically without jeopardizing the numerical accuracy. So the answer to the question posed in the previous paragraph is that we simply did not reach the transition, which should occur at yet smaller particle size. This difference in the transition size for TE and TM modes has a simple physical explanation. For thin dielectric cylinders, as in 3D,

scattering is dominated by dipolar scattering, where analytical results are available [3]:

$$Q_{TM} = \frac{\pi^2}{8} x^3 (n^2 - 1)^2; \quad Q_{TE} = \frac{\pi^2}{4} x^3 \left( \frac{n^2 - 1}{n^2 + 1} \right)^2; \quad \frac{Q_{TM}}{Q_{TE}} = \frac{(n^2 + 1)^2}{2}, \quad (3.3)$$

One can see the difference in the scattering strength is about 17, and reflects the stronger polarizability of a thin cylinder along the axis compared to that perpendicular to the axis. This numerical prefactor leads to the difference in the characteristic size for two polarizations. Moreover in the saturated regime, the value of the average lasing threshold is relatively lower for TM than that for TE waves. This can be explained by stronger interference effects in TM polarization, which is equivalent to the scalar wave. In this respect the interference is harder to achieve for TE modes, that leads to higher threshold as seen from Fig. 3.12.

The difference between TE and TM lasing threshold also exhibits itself through the fluctuations in Fig. 3.13. Computational time has limited the number of disorder realizations, and led to the relatively large errorbars. Nevertheless one can still conclude that there is a general trend in increasing fluctuations  $\delta\gamma$  upon decrease of the particle size, as it was seen in the experiment. This increase occurs at different size for TE and TM polarizations, which is in line with the above discussion. Fluctuation for TE field is generally higher than that for TM field. As mentioned earlier, availability of 2 electric field polarizations in the former case is the cause.

We should also mention that one needs to exercise caution when comparing the results of 2D simulations with 3D experiments. Indeed, the dependence of the lasing threshold

and its fluctuation on the particle size is dimension-dependent effect. As it can be seen from Table 3.2 and Fig. 3.13,  $\delta\gamma$  showed similar trend in both 2D simulations and 3D experiments. However, normalized standard deviation  $\delta\gamma/\langle\gamma\rangle$  behavior is different: in 3D it increased with decrease of  $d$  (Table 3.2), while in 2D it instead decreased for TE polarization (not shown). Further simulations performed on 3D random systems are necessary to resolve this discrepancy. The very similar behavior of lasing threshold with the transport mean free path confirmed the close relation between the random laser and photon localization. It also showed the possibility of studying photon localization in multiple scattering system by using random lasing effect.

### 3.6 Discussion and Conclusion

We would like to dress one question in this discussion section: Can Anderson localization of light can be achieved by resonant scattering? There were some reports indicating that localization was observed in the vicinity but off the resonance frequency of individual scatterers [28,109,110]. Actually, even in diffusive systems it was shown that the optimum scatterer size for maximum scattering was smaller than the that predicted by Mie theory of a single scatterer [111]. However, this result can be easily understand since  $l_{sc} = 2d/(3fQ_{sc})$ , where  $d$  is the scatterer's diameter and  $f$  is the scatterer filling fraction. For fixed  $f$ , maximum scattering occurs at scatterer size  $d_0$  where  $l_{sc}$  reaches a minimum, which requires that  $Q_{sc}/d$  reaches a maximum. The diameter  $d_0$ , however, is typically slightly smaller than the resonant scatterer size where  $Q_{sc}$  is a maximum, especially for

low refractive index scatterers. For scatterers with a high refractive index, Mie resonances are typically sharp and  $d_0$  gets very close to the resonant scatterer size. This argument, though explains Ref. [111] well, cannot explain the results in Refs. [28, 109, 110]. Those results showed that the localization region was always on the higher frequency side of the first Mie resonance, and Ref. [110] even showed that with increasing filling fraction of scatterers, the localization region shifted to even higher frequencies from the first Mie resonance. As discussed in Ref. [28], localization is achieved when  $g = \delta\nu/\Delta\nu < 1$ , where  $\delta\nu$  is the average mode linewidth and  $\Delta\nu$  is the average mode spacing. Resonant scattering helps to decrease  $\delta\nu$  by increasing the dwell time of light inside the system, while  $\Delta\nu$  can be increased by reducing the density of states by, say, the photonic band gap effect. For a random system, the PBG of its periodic counterpart system is typically at the frequency higher than the first Mie resonance frequency of single scatterers, so it is very likely that the results in Refs. [28, 109, 110] are due to the residual PBG effect in their systems. Moreover, the result in Ref. [110] that the localization region shifted to higher frequency with increasing scatterers filling fraction somehow confirmed this explanation, since increasing scatterer density induced lattice constant reduction, which would shift the PBG to higher frequency. Whether Anderson localization can be achieved solely by resonant scattering is still a debated question [20, 112–116]. Here I give a very naive derivation which, I think, shows that it is *possible* that Anderson localization can be achieved solely by resonant scattering.

The criteria for Anderson localization we are using here is the Ioffe-Regel condition:

$k_e l_{sc} < 1$  (1), where  $k_e = 2\pi n_e/\lambda$  and  $l_{sc} = 1/\rho\sigma_{sc}$ ,  $n_e$  is the effective refractive index of the random system. We know that such a definition of  $l_{sc}$  can only be satisfied in the independent scattering approximation, so we require the second condition:  $\sigma_{sc}$  of each scatterer does not touch each other, which means  $rQ_{sc}^{1/2} < 0.5\rho^{-1/3}$  (2), where  $r$  is the scatterer radius,  $Q_{sc} = \sigma_{sc}/\pi r^2$  is the scattering efficiency. Starting from condition (1) and (2), we can do the following:

$$l_{sc} = \frac{1}{\rho\sigma_{sc}} = \frac{1}{(f/v)(Q_{sc}\pi r^2)} = \frac{4r}{3Q_{sc}f} \quad (3.4)$$

where  $f$  is the scattering filling fraction and  $v = 4\pi r^3/3$  is the volume of individual scatterers. Substituting Equ. 3.4 into the Ioffe-Regel condition, one can get

$$k_e l_{sc} = \frac{2\pi}{\lambda} \cdot \frac{4r}{3Q_{sc}f} = \frac{4x}{3Q_{sc}f} < 1 \quad (3.5)$$

Here we assume  $n_e = 1$ , which should not change the results anyway. From condition (2), one can easily derive that

$$Q_{sc}^{1/2} < (\pi/6f)^{1/3} \quad (3.6)$$

Combine Equ. 3.5 and 3.6, one can get the final condition

$$\frac{4x}{3f} < Q_{sc} < \left(\frac{\pi}{6f}\right)^{2/3} \quad (3.7)$$

Such a condition can be satisfied under certain situations. For example, let's assume

$f = 0.1$ , which is a typical number satisfying the independent scattering approximation, then condition 3.7 becomes  $40x/3 < Q_{sc} < 3$ . This can be satisfied for many  $x$  and  $Q_{sc}$  pairs, e.g.,  $x = 0.1$  and  $Q = 2$ , which can be true for small scatterers with a high refractive index. Though  $Q_{sc}$  is a function of  $x$  and localization has to be achieved within a frequency window with finite width, suitable scatterers and a frequency range may still be able to be found.

Now we would like to discuss why we did not achieve light localization in our resonant scattering samples. Instead of a resonance dip in either transport mean free path  $l_t$  or random laser threshold  $I_{th}$  as functions of scatter size, we only observed that both quantities quickly decreased but then saturated with increasing scatterer size. The reason lied in the fact that our samples were too closely packed. The separation between neighboring scatterers was so short that dependent scattering occurred, which quenched the resonance enhancement from individual spheres. Unfortunately, due to our experimental limitation, we can not fix this problem. This problem, however, can be solved in either a charged colloidal solution [117] or systems where scatterers are embedded into spacer materials [28]. And indeed light localization was observed in such system.

In summary, we have managed to synthesize monodisperse ZnO spheres with well controlled sizes for a large range. Using it as the building block, both periodic opal structures and random samples were successfully prepared. The FCC ZnO opal structure was obtained by an evaporation enhanced self-assembly process, and photonic band gap was demonstrated as a transmission dip or reflection peak along the  $\langle 111 \rangle$  direction.

By changing sphere size, the gap was tuned through the entire visible spectrum range from UV to IR. Random samples were fabricated by cold pressing ZnO spheres into a pellet, and the scattering strength in such samples was calibrated by the transport mean free path  $l_t$  measurement with coherent backscattering. It was shown that with sphere diameter increasing,  $l_t$  first decreased quickly then saturated for random samples with larger spheres. A GMM simulation was performed to calculate  $l_t$  and comparisons between experimental data and simulation results were made and discussed. Random lasing behavior was studied in these random samples. The threshold mean value and standard deviation were measured experimentally and calculated by the FDTD method in 2D systems for different polarizations. The random laser mean threshold changed with sphere size, following a similar trend to that of the transport mean free path, which confirmed the important role scattering played in random lasers.

## CHAPTER 4

### ZNO PHOTONIC CRYSTAL SLAB LASERS

#### 4.1 Motivation

In the previous chapter, we explored the closely packed resonant scatterer samples trying to decrease the scattering mean free path  $l_s$ , which, according to Ioffe-Regel criterion  $k_e l_s < 1$ , would help photon localization thus reducing the random laser threshold. However, it has been shown that though  $l_s$  can be greatly reduced by resonant scattering, close packing made scattering from each scatterer strongly coupled. Such dependent scattering limits the further decrease of  $l_s$  as well as the random lasing threshold. From Ioffe-Regel criterion expression, it can be seen that the reduction of both  $k_e$  and  $l_s$  will help it to be satisfied. Therefore, in this chapter, we will investigate the effect of reducing the effective wavevector  $k_e$  on both photon localization and random lasers.

Reducing  $k_e$  can be achieved by introducing structure order into the a disordered system. Such a system can be viewed in two different ways: a disordered structure with correlations (either short or long range), or a periodic structure with disorder. In this thesis, we will follow the second description. In particular, we will start with an ideal periodic structure, then introduce disorder into it. The structures with a periodically modulated dielectric constant are called photonic crystals, which have been a field with

tremendous research interest for two decades. Though photonic crystals (which deal with periodic structures) seem to have no relation to random lasers (which deal with random structures), they can be strongly connected through a shared common point: photon localization. Photon localization, which was first proposed in completely random structures, has been achieved in photonic crystals first due to the photonic bandgap (PBG) effect in three dimension. By introducing a defect state into the PBG, the structure can lase at a very low threshold. Though it is related to the structure disorder, it is not called a random laser, but a photonic crystal laser.

We have already managed to prepare a 3D photonic crystal structure: ZnO opals by self-assembly. However, due to a lack of a complete bandgap, the lasing threshold in such samples was not significantly lowered compared to the random samples. Moreover, the self-assembly process limited our ability to control the degree of disorder in the opal structures, which prevented us from quantitatively studying the effect of disorder on lasing in photonic crystals. This situation forced us to think about preparing samples in two dimensions instead. Compared to 3D structures, 2D structures are ready to fabricate thank to all kinds of lithography and etching techniques, moreover, structures with well controlled randomness can be easily obtained by mask design. Because of those advantages, we determined to conduct our experiment using 2D structures.

In this chapter, we investigate the lasing phenomenon in 2D structures changing from periodic to random. The samples we studied are different patterns etched in ZnO film on a sapphire substrate. Strictly speaking, such structure is not 2D but 3D, which indeed

makes our experimental results different from theoretical predictions for 2D structures, which we will discuss at the end of this chapter. The chapter is presented as follows: we first discuss the design of ZnO photonic crystal slabs with an optimized PBG overlapping the ZnO gain spectrum, then discuss the structure fabrication process by FIB etching and lastly discuss the experimental results. Lasing in samples with different amount of randomness are simulated by FDTD calculations and their experimental counterparts are discussed in the conclusion.

## 4.2 Band Structure Calculation of ZnO Photonic Crystal Slabs

In our experiment, 2D periodic patterns have been etched in ZnO thin films. This kind of structure is called photonic crystal slabs (PhCS) and has attract much attention because of their potential applications to various optoelectronic devices and circuits [59, 118–123]. PhCS may lead to a complete photonic band gap for the guided modes when the wave propagation in all in-plane directions is forbidden due to Bragg interference. Moreover, its planar geometry makes it easy to incorporate on a chip, as well as offers a possibility of low threshold laser sources [59, 124–129]. These lasing modes are either defect state modes or band edge modes, however, so far the experimental efforts mainly concentrated on PhCS made of III-V semiconductors. They operate in the infrared (IR) communication frequencies. There is technological and commercial demand for compact and integrable laser sources in near the ultraviolet (UV) range of optical spectrum. Because ZnO is an efficient UV emitter with large exciton binding energy ( $\sim 60$  meV), it is a good

candidate for UV photonic crystal laser operating at room temperature. In this section, we will investigate the band structure of ZnO PhCS, which offers us the guidance for experimental fabrication of ZnO PhCS lasers.

Although Bragg reflection and index guiding description of the electromagnetic field in PhCS can elucidate many physical phenomena that occur in such system, it is naive because both in-plane and vertical propagations or confinements are inseparable. In order to obtain the photonic modes of PhCS one needs to solve the problem self-consistently within the same framework. This can be done with a plane-wave expansion method [103] that in fact became a standard in the field.

In most IR PhCS structures, the photonic layer is usually cladded with air above and below (see e.g. [59, 128, 129]). This design is advantageous for a number of reasons. First, this is a symmetric structure: there exists a reflection symmetry with respect to the plane that goes through the middle of the PhCS. This symmetry allows two orthogonal classes of eigenfunctions of Maxwell equations: symmetric and antisymmetric [130]. Supercell for the band structure calculation can be easily constructed by repeating ...-air-PhCS-air-PhCS-... indefinitely in the vertical direction. It was shown that low-lying (E-field) symmetric modes are predominantly TE polarized, while antisymmetric ones are TM polarized. Due to superior guiding properties of TE modes and the fact that a self-supporting membrane percolated by air holes (unlike the collection of dielectric cylinders in air) exhibits a PBG for the same polarization, this geometry is widely used in practice. The supercell photonic band-structure calculations also give unphysical modes that do

not correspond to the guided modes of the PhCS (confined to the slab). Fortunately, physical (guided) modes can be separated using the concept of light cone as follows. In the result of photonic band-structure calculation one obtains the frequency  $\omega$  for a given in-plane wave vector  $k_{\parallel}$ . This electromagnetic EM mode (concentrated inside the photonic layer) is coupled only to the modes outside the layer with the same  $(\omega, k_{\parallel})$ . If  $\omega < ck_{\parallel}$ , then  $k_z = \sqrt{\omega^2/c^2 - k_{\parallel}^2}$  is imaginary outside the PhCS. Thus the light intensity decays exponentially in the  $z$  direction away from the layer. This describes a guided mode. In the opposite case,  $k_z$  is real and light can escape to the infinity. Such a mode is a leaky mode, which cannot be accurately described in the supercell calculations. A continuum of modes with  $\omega > ck$  form a light cone (a cone in  $\omega - k$  space). Therefore, PBGs obtained in all planar geometries are, strictly speaking, photonic band gaps for guided modes.

In our ZnO PhCS structure, ZnO photonic layer is on sapphire substrate whose refractive index is 1.78. Unlike in III-V PhCS structures, selective removal of the underlying layer of sapphire is currently not allowed. This experimental limitation leads to severe restrictions: first, presence of the sapphire substrate lifts the reflection symmetry. this results in mixing between TE-like and TM-like classes of EM modes. second, the non-air substrate presents a second light cone, which reflects more serious radiative loss into the sapphire substrate (leakage into the substrate starts for  $\omega > (c/n_s)k_{\parallel}$ ). In such asymmetric PhCS, high filling fraction of ZnO in the photonic layer is required to satisfy the waveguiding in  $z$  direction, which in turn put a upper limit of feature size can be

fabricated in the experiment.

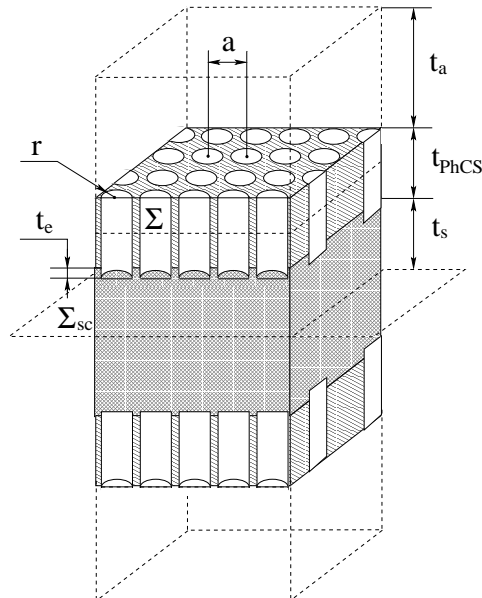


Figure 4.1: Schematic diagram of the vertical super-cell used in photonic band structure simulation. Cylindrical air holes of radius  $r$  are arranged in a hexagonal pattern with lattice constant  $a$ . The holes extend throughout the slab of thickness  $t_{PhCS}$  and may penetrate into the substrate to the depth of  $t_e$ . The thicknesses  $t_a$  and  $t_s$  need to be chosen sufficiently large (see text for discussion). The cell is symmetric with respect to reflection in  $\Sigma_{sc}$  plane. For convenience we also introduce a middle plane of the slab,  $\Sigma$ .

A band-structure calculation technique for the asymmetric geometry like ours was proposed in Ref. [130]. The authors proposed to use a supercell where ...-substrate-PhCS-air-substrate-PhCS-air-... is periodically repeated in the  $z$  direction. Special care needs to be exercised in order to avoid unphysical solutions that correspond to the guided modes in the substrate layers bounded by air and a PhCS. In our simulation we constructed a different supercell by combining the structure and its mirror image (shown in Fig. 4.1) for the photonic band calculation. Our choice of the unit cell is motivated by the following. Due to a particular arrangement of the layers in our supercell, there exists an

artificial symmetry reflection plane  $\Sigma_{sc}$  in Fig. 4.1. Therefore, there is an artificial classification of the modes into symmetric and antisymmetric, as it is schematically shown in Fig. 4.2. This property provides a way to control the precision of the bandstructure calculation. Indeed, only for the PhCS-guided modes (with eigenfrequencies outside of the air and substrate light cones), and only when the thicknesses of air  $t_a$  and substrate  $t_s$  layers are chosen to be sufficiently large, the eigenfrequencies of the  $\Sigma_{sc}$ -symmetric and  $\Sigma_{sc}$ -antisymmetric modes are nearly degenerate. This can be seen from Fig. 4.2: there should be no difference in eigenenergy between the functions when the value of the eigenfunction is close to zero at the (i)  $\Sigma_{sc}$  plane and (ii) the top/bottom of the supercell. The second condition arises because of the periodicity in the vertical direction: the top/bottom of the super-cell is also a middle plane that separates two closest PhCS layers.

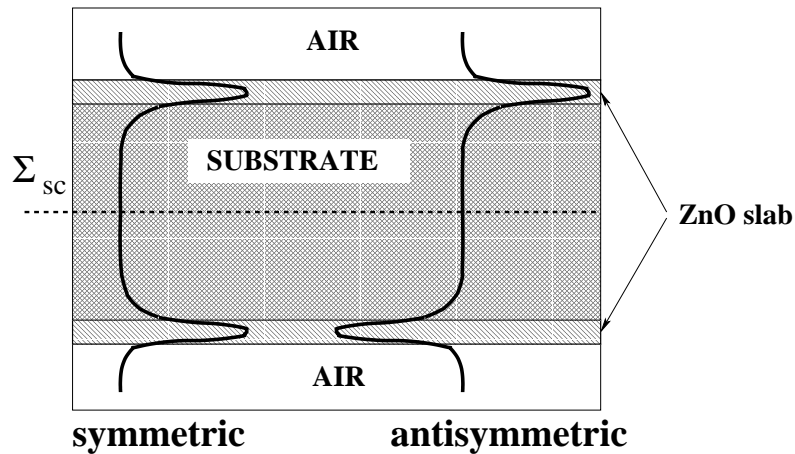


Figure 4.2: Reflection symmetry allows for solutions symmetric and antisymmetric with regard to reflection in  $\Sigma_{sc}$ . This artificial symmetry helps to separate the guided modes from the leaky ones, see text for details.

Furthermore, one may think that the doubling of the cell size should increase the computation time. However, at least for a PhCS with a hexagonal symmetry,  $\Sigma_{sc}$  contains a center of inversion. The latter allows us to perform the photonic band-structure calculation, assuming that inversion symmetry shortens the calculation time (of one symmetry) by a half. In all simulations reported below, we checked the consistency of the results with the procedure outlined above, then studied the band structure of the modes outside of the substrate (more restrictive) light cone.

We chose hexagonal lattice in-plane structure due to its high rotational symmetry, which offers a higher possibility to open a complete band gap in-plane. In Fig. 4.3 we show an example of the calculated photonic band structure. Air light-cone boundary,  $\omega = ck_{||}$ , and substrate light-cone boundary,  $\omega = (c/n_s)k_{||}$ , are shown with dash dot and dashed lines, respectively. The presence of a sapphire cone makes guiding at the  $\Gamma$  point impossible and limits any band gap to  $a/\lambda < 0.325$ . For PhCS laser operation we need to overlap a photonic band gap with a gain spectrum of ZnO,  $380 < \lambda < 400$  nm. Consequently, the lattice constant in the hexagonal air-hole pattern of PhCS has an upper bound of  $a < 130$  nm.

Since the presence of the substrate removes the symmetry with respect to reflection in PhCS middle plane ( $\Sigma$  in Fig. 4.1), one cannot separate the modes into two independent classes and consider them separately. This separability was crucial for obtaining sizable PBG in a photonic membrane (or strictly two-dimensional structures). For comparison, we calculated the band structure of the system with the same parameters as in

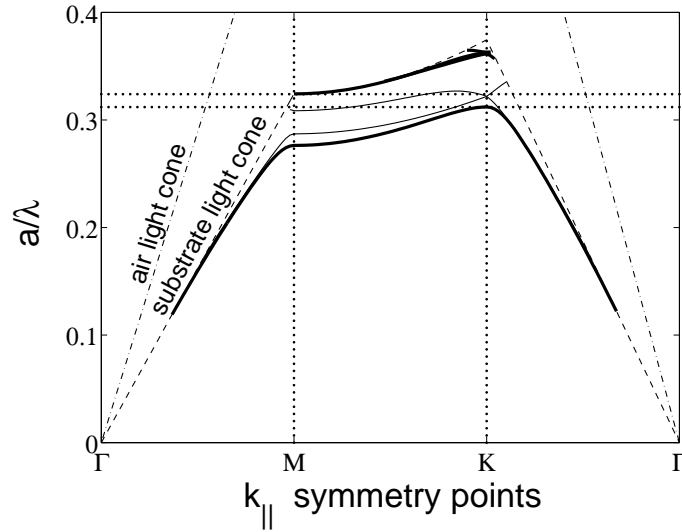


Figure 4.3: Calculated band structure of ZnO photonic crystal slab air cylinder radius  $r/a = 0.25$ , and slab thickness  $t/a = 1.4$ . The refractive indexes for ZnO and sapphire are 2.35 and 1.78. Thin and thick lines represent TM and TE polarized modes respectively.

Fig. 4.3 but sapphire substrate was replaced by air. The obtained dispersions looked qualitatively similar to the ones in Fig. 4.3, so that it was possible to make band-to-band correspondence. This has been used previously to justify the existence of PBG in the spectrum of TE modes [120]. In our case the refractive index of the substrate is quite large, moreover it may even become comparable to the effective index of PhCS as the patterning of ZnO film with original refractive index  $n_{ZnO} = 2.35$  will reduce it to just a little above that of the sapphire. These considerations warrant an in-depth analysis of the mode polarizations.

In order to determine the degree of polarization of the electromagnetic eigenmodes of PhCS, we studied

$$\langle F(z) \rangle = \int F(x, y, z) dx dy, \quad (4.1)$$

where  $F$  represents  $x, y$  or  $z$  component of electric or magnetic field. Figure 4.4 shows these quantities for the first two bands taken at  $M$ -symmetry point of Figure 4.3. It is clearly seen that the first (the lowest frequency) mode  $M_1$  is strongly TE polarized:  $E_x$ ,  $E_y$  and  $H_z$  are more than one order of magnitude larger the other components. Furthermore, as discussed above dominant components are nearly symmetric with respect to middle plane of PhCS, whereas  $H_x$ ,  $H_y$  and  $E_z$  are close to antisymmetric. The deviation from the perfect symmetry is entirely due to the presence of the sapphire substrate. Comparing the second mode  $M_2$  to the previous case one notices that the polarization of the field has changed to the opposite —  $M_2$  is predominantly TM polarized.

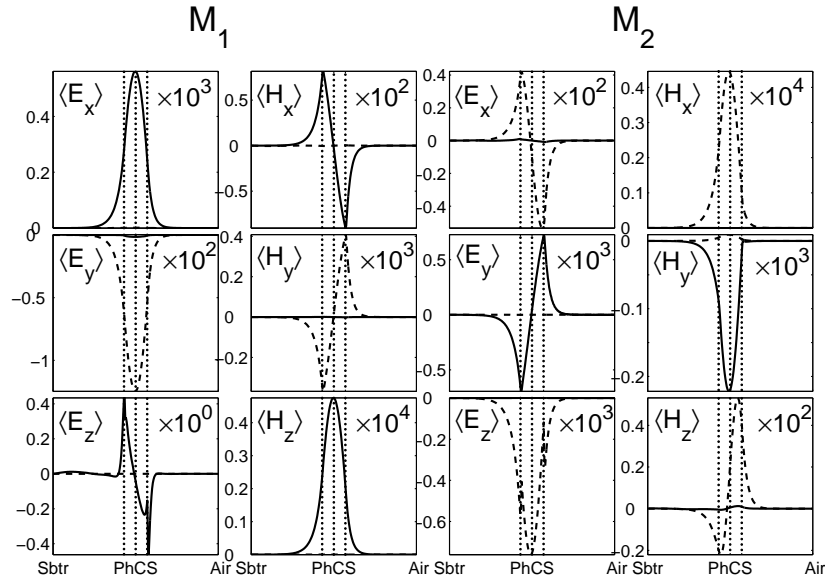


Figure 4.4: Integrated according to Eq.(4.1)  $x, y$  and  $z$  components of the electric,  $E$ , and magnetic,  $H$ , field. Solid/dashed lines represent real/imaginary part of the field. First/second two columns correspond to the first/second mode of Fig. 4.3 taken for  $k_{||}$  at  $M$  symmetry point. The same normalization is used for all field components, so that their values can be compared. Mode  $M_1/M_2$  shows a pronounced TE/TM polarization.

An increase in the order of the band does lead to enhancement of polarization mixing.

However as we will see in more detail below, the substrate light-cone condition restricts the involvement of higher-order bands. We checked the polarization of the lowest six bands in several  $k_{\parallel}$  points and found that in all relevant cases certain symmetry, TE or TM, can be assigned to each band. Therefore, despite of highly asymmetric claddings (sapphire versus air) and relatively small refractive index contrast between PhCS ( $n_{eff} \sim 2.1$ ) and the substrate ( $n_s = 1.78$ ), the mixing of the polarizations in the low-order photonic bands is limited. We measured the polarization of ZnO emission intensity from a 600 nm-thick ZnO film on sapphire substrate. c-axis of ZnO is perpendicular to the surface of the film. ZnO is optically excited by the third harmonic of a mode-locked Nd:YAG laser (355 nm, 10 Hz, 20 ps). A cylindrical lens ( $f = 100$  mm) is used to focus the pump beam to a strip normal to the edge of the sample. The emission was collected from edge of the sample at  $1 \mu J$  pump pulse energy. The pump area was about  $2000 \times 50 \mu m$ . Figure 4.5 clearly demonstrates that the emission is strongly polarized with the electric field parallel to the film (TE polarization) [37, 131]. Because the emission in the ZnO thin film is predominantly TE polarized we need to consider only the TE-polarized photonic modes. This motivates a detailed analysis of the polarization of the modes in the experimentally relevant PhCS. From now on we will ignore TM polarized bands. In the next section we will systematically study the effect of the structural parameters on the width of PBG in the spectrum of TE (see thick solid lines in Figure 4.3) modes.

We intend to optimize the following three parameters that can be controlled in the FIB etching [132]: (i) PhCS thickness,  $t_{PhCS}$ , (ii) air hole radius,  $r$  (related to the filling

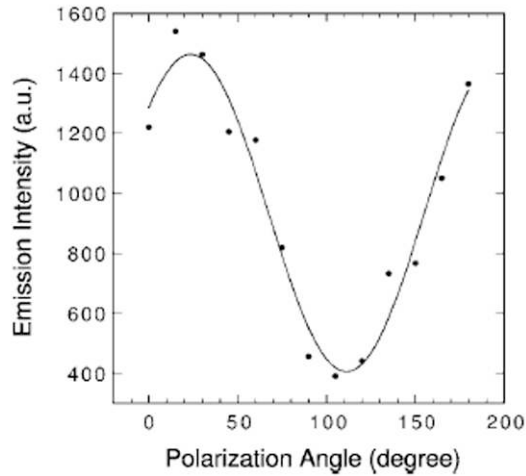


Figure 4.5: Experimentally measured emission intensity from 600 nm ZnO film as a function of polarization angle. The maximum intensity at about  $25^\circ$  corresponds to E-field polarization parallel to the plane of the film (TE polarization).

fraction  $f$ ) and etch depth,  $t_e$ . Due to linear nature of Maxwell equations, we normalize all parameters to the value of lattice constant,  $a$ . Our goal is to maximize the relative (normalized to the center frequency) PBG width. Once this is achieved, we can overlap PhCS gap with the emission spectrum of ZnO by choosing appropriate  $a$ . From the experimental perspective it is difficult to reproduce extremely small structural features, therefore we prefer to have PBG at high values of  $a/\lambda$  if possible.

Figure 4.6 shows the results of our simulation. In panel (a) of the figure, we plot the position and relative width of PhCS as we vary  $r/a$  within the range  $0.18 - 0.30$ , and keep  $t_{PhCS}/a = 1.4$  and  $t_e = 0.0$ . This corresponds to a change in the pattern filling fraction from  $f = 0.88$  to  $f = 0.67$ . One can clearly see that there exists a PBG maximum at  $r/a \simeq 0.24$  (or  $f \simeq 0.79$ ). This effect has a clear physical interpretation: at large filling fractions (small  $r/a$ ) the index contrast within PhCS is small, therefore band

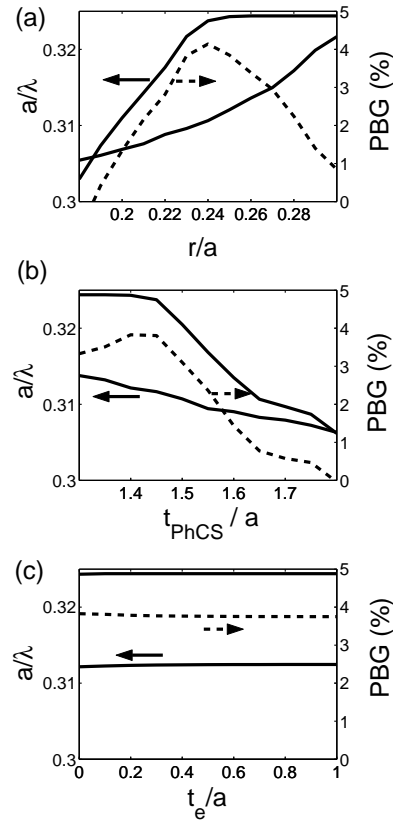


Figure 4.6: The position and relative size of photonic bandgap for PhCS with variable structural parameters. (a)  $t_{PhCS}/a = 1.4$ ,  $t_e = 0$ ; (b)  $r/a = 0.25$ ,  $t_e = 0$ ; (c)  $r/a = 0.25$ ,  $t_{PhCS}/a = 1.4$ .  $n_{ZnO} = 2.35$  and  $n_s = 1.78$  were used in the calculation. The left vertical axes should be used with solid lines, which represent the edges of PBG. Dashed lines and the right vertical axes show the relative size of the gap.

splitting, as well as PBG, is small. At small filling fractions, the wave guiding becomes poor, furthermore the decrease of the effective refractive index of the photonic layer leads to a shift of PBG as a whole to higher frequency. Eventually, at  $r/a \simeq 0.26$  the top of the gap is set not by the higher order guided mode but by  $a/\lambda \simeq 0.324$  at the light-cone when  $k_{||}$  is at  $M$ -point (see Fig. 4.3). In reality, above this frequency the guided modes will always be coupled to some leaky modes inside the light-cone. This phenomenon results in a plateau of the upper bandgap edge for  $r/a = 0.26 - 0.30$ . Consequently, PBG disappears at  $r/a > 0.30$ . For the air holes with such a large radius, the effective refractive index of PhCS  $n_{eff} \simeq 1.87$  approaches that of the substrate.

Figure 4.6(b) presents the effect of the photonic layer thickness,  $t_{PhCS}$ , on PBG. With the increase of  $t_{PhCS}$  we also observe a maximum. For samples thinner than the correspondent wavelength, the eigenmodes of the system substantially “spill” into the air and (mostly) the substrate. Consequently, the effective index of PhCS becomes comparable to  $n_s$  so that PBG lies at higher frequencies. The light-cone leads to the plateau of the upper bandgap edge as in the case of large  $r/a$  in Fig. 4.6(a). For very thick photonic layers,  $t_{PhCS}/a > 1.5$ , the gap closes again. This occurs due to a stronger dependence of upper band edge frequency on the effective refractive index of PhCS. Indeed, as  $n_{eff}$  is increased the band forming the upper edge of PBG develops the kinks close to the light-cone, that leads to the reduction of PBG as seen in Fig. 4.6(b). As a result of these dependences, the size of the gap can be maximized at  $t_{PhCS}/a \simeq 1.45$ .

The possibility of improving guiding properties of the photonic layer by extending

the air holes into the substrate was discussed in Ref. [133]. Indeed, removing a part of the substrate material lowers its refractive index and achieves a partial effect of “undercutting”. However, the fact that PBG in our case lies close to the light-cone has a significant effect. An increase in  $t_e$  results in the decrease of the effective refractive index experienced by a guided mode, because it extends into the substrate. Therefore the eigenfrequency of the mode increases and may enter the light-cone [134]. This is exactly what happens in our system as shown in Fig. 4.6c. As  $t_e$  is increased the upper edge of PBG becomes defined by the position of the substrate light-cone at  $M$  k-point (Fig. 4.3), whereas the mode that defines the lower edge of PBG is more confined to PhCS and, therefore, is less sensitive to the effect of  $t_e$ . As a result, Figure 4.6(c) shows a weak dependence on the etch depth.

As we discussed in the previous section our calculation of the photonic band gap relies on the possibility of separating the photonic bands based on their polarization. To check the consistency of this assumption we calculated the ratios between in-plane and normal components of the electric fields for various structural parameters. In Fig. 4.7, we show the polarization ratios calculated for the lowest four bands at two  $k_{||}$  vectors ( $M$  and  $K$  k-points). As the structural parameters are varied, the polarization of the modes is preserved. The most noticeable change occurs with the increase of  $r/a$  in Fig. 4.7(a). This is due to significant modification of the band structure that occurs in this case. Notwithstanding, the modes still remain strongly polarized, justifying our methodology.

As conclusion, in the photonic band structure calculation we find the optimum set of

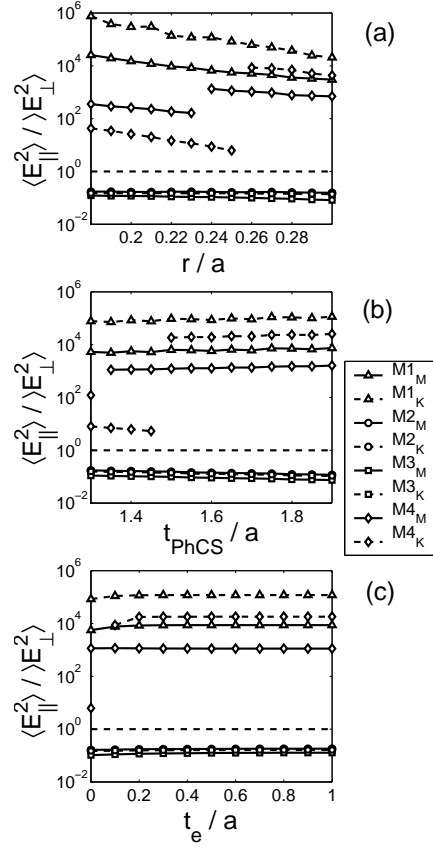


Figure 4.7: The degree of polarization of the modes calculated for  $k_{\parallel}$  in  $M$  (solid lines) and  $K$  (dashed lines) k-points. The modes belonging to the lowest four bands are considered. Cases (a)-(c) correspond to those of Fig. 4.6.  $\langle \dots \rangle$  denotes an integration over  $x$  and  $y$  coordinates. Discontinuities in the curves occur when the order of bands changes.

parameters for maximum PBG:

$$\frac{r}{a} \simeq 0.24 \quad \frac{t_{PhCS}}{a} \simeq 1.45 \quad \frac{t_e}{a} \simeq 0.0 \quad (4.2)$$

These parameters are significantly different from the typical parameters for IR PhCS. This is due to several factors: (i) presence of the sapphire substrate brakes vertical symmetry of PhCS; (ii) the refractive index contrast of ZnO/sapphire is lower than that of InP/air usually used in IR PhCS; (iii) to preserve guiding in the photonic layer the filling fraction and the thickness of ZnO PhCS needed to be significantly increased. This in turns explains the relatively small PBG of about 5% that can be obtained in the ZnO PhCS on sapphire.

Overlapping the photonic bandgap with the emission spectrum of zinc oxide required precise control of the designed pattern with

$$a \simeq 123nm; t_{PhCS} \simeq 180nm; t_e \simeq 0nm; r \simeq 30nm. \quad (4.3)$$

This has been achieved with the FIB etching technique which we will discuss in next section.

### 4.3 Fabrication of ZnO Photonic Crystal Slab Lasers

Following the design in the previous section, we started to fabricate the PhCS structure in ZnO films. To our purpose, high quality single crystalline ZnO films with well controlled

thickness are desired. Such films were grown on c-plane sapphire substrates with plasma enhanced chemical vapor deposition (PECVD) technique. Film growth details can be found in Ref. [135] and will not be discussed here. To show the film's high quality, both TEM and SEM images are shown in Fig. 4.8. From the TEM image, the crystalline structure for both sapphire substrate and ZnO film are clearly shown. Though there are defects on the first few epitaxy layers close to the interface with sapphire substrate due to the 18% lattice mismatch, superior epitaxy of the single crystalline ZnO film was obtained with its c axis normal to the sapphire substrate. The side view SEM image of the film shows a very smooth cleave face, which again confirms the single crystalline structure. The top view of the film shows some features, but AFM measurement confirmed that the film surface is very smooth, with a roughness rms value of 2nm over 10  $\mu m$  range for a 200nm thick film.

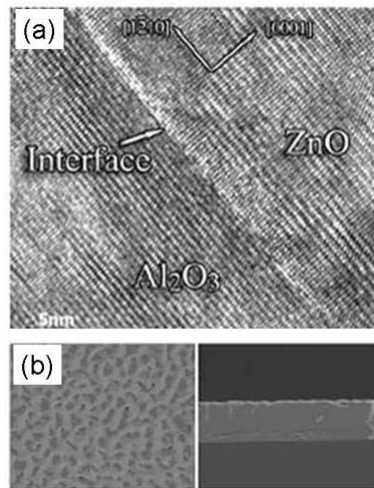


Figure 4.8: (a) High resolution TEM (b) Top and side SEM images of ZnO films grown on c-plane sapphire substrate at  $750^{\circ}C$  by POMBE. Horizontal scale for SEM: 1  $\mu m$ .

With the single crystalline ZnO film, we managed to etch various photonic patterns

through it. Our band structure calculation sets the guidance:  $a \simeq 123nm$  and  $r \simeq 30nm$  for a hexagonal lattice. Such small features are technically challenging and currently can only be obtained by two processes: (i) e-beam lithography followed by reactive ion etching, (ii) focused ion beam etching. We decided to choose the second one (FIB) for following considerations: first, FIB is a one step process while the other option needs at least two steps. It not only makes the fabrication process much simpler, but also lowers the possibility for generation of imperfections. Second, though there has been some reports on RIE etching of ZnO, the results were far from our requirement. High aspect ratio non-isotropic etching of ZnO in such small scales is quite challenging and no successful recipes available currently as we know.

In Fig. 4.9, a simple sketch of the FIB facility is shown.  $Ga^{3+}$  ions were accelerated by a high voltage from the source, and focused by an EM lens onto the sample surface. An aperture with variable size was used to change the beam current, which changed the etching rate. A typical etching recipe for a 200nm thick ZnO PhCS structure is: accelerating voltage (30 keV), beam current (30 pA), dwell time on each etching point ( $16 \mu s$ ), total number of frames (400). The fabrication time of a typical  $8 \times 8 \mu m$  PhCS structure is about 5 min.

A typical sample prepared by FIB etching is shown in Fig. 4.10, where hexagonal latticed air cylinders were fabricated in a 200nm thick ZnO film. One can see that each air cylinder is far from a perfect circle, but the deviation for all the cylinders are similar, which makes the long range periodicity still kept in the structure. The side view SEM

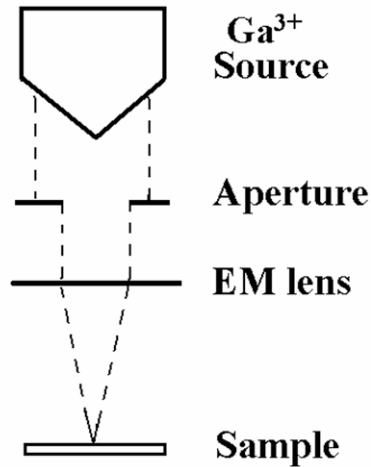


Figure 4.9: A simple sketch of FIB etching setup.

image shows that the air cylinders were etched through the ZnO layer without large deviation from the vertical direction. For a typical  $8 \times 8 \mu\text{m}$  pattern with in-plane lattice constant  $a = 125\text{nm}$ , there are more than 4000 air cylinders in the pattern. If a mode is well localized in-plane near the pattern center, the system can be treated as infinite in plane, while for an extended mode, the energy leakage from the boundary can not be neglected.

One disadvantage of the FIB etching process is that the ion bombardment introduces defects into ZnO crystal and degrades its optical quality, which was indeed confirmed by the PL measurement. In fact, none of the as-fabricated samples with FIB can lase even under intense optical excitation. To recover the optical quality, the samples were annealed in air at  $600^\circ\text{C}$  for 30 min. Such temperature was chosen because that experiments showed lower temperatures did not recover the crystal quality well, while higher temperatures changed the structure of our patterns at long annealing time. To improve the crystal quality further, rapid thermal annealing at higher temperature were

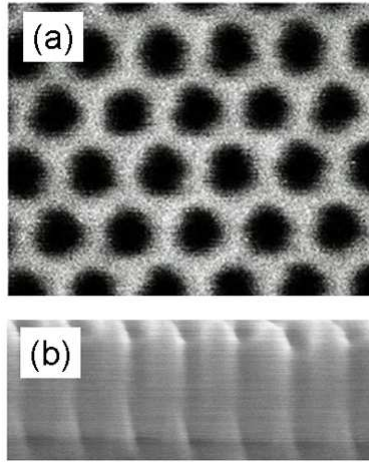


Figure 4.10: SEM of hexagonal lattice air cylinder structure fabricated with FIB in ZnO film. (a) top view, horizontal scale: 800 nm (b) side view, horizontal scale: 1.2  $\mu\text{m}$ .

tried. However, up to 1200°C with 1 min annealing time, no significant reduction of lasing threshold were observed in our samples. More systematic and detailed studies are needed to clear this issue, so far we have applied the furnace annealing at 600°C for 30 min to all of our samples.

To test our theoretical prediction, we fabricated hexagonal lattice photonic structures with different lattice constants  $a$ , while keeping  $r/a$  the same. We managed to achieve both coarse and fine tuning of  $a$  by two different methods. The coarse tuning with step size of 15.6 nm was realized by utilizing different patterns. In particular, the maximum pixel resolution of the template which can be imported into the FIB facility was 512 by 512. So for a 8x8  $\mu\text{m}$  pattern, the minimum change of  $a$  was one pixel and it was 15.6 nm. With such a step size, patterns with  $a$  from 100 nm to 160 nm were fabricated. To achieve finer tuning of  $a$ , we changed the working distance from the EM lens to the sample surface by moving the sample vertically, which changed the magnification of the

real pattern to the template. Using this method we tuned  $a$  in a step size as small as 2nm in an  $8 \times 8 \mu\text{m}$  pattern. Such fine tuning was applied to patterns where  $a$  was close to the predicted optimum value: 123 nm, and patterns with  $a$  changed from 110 nm to 130 nm were fabricated with a 2nm step.

## 4.4 Optical Characterization of ZnO Photonic Crystal Slab

### Lasers

The ZnO PhCS samples were optically pumped by the third harmonics of a mode-locked Nd:YAG laser (355 nm, 10 Hz, 20 ps) at room temperature. We used the picoseconds pump laser simply because of its availability. Since the pump pulse is much shorter than the lifetime of exciton in ZnO (which is a few hundred of pico seconds), the peak power required to reach the lasing threshold would be much higher than that with nanosecond pump pulses. A schematic sketch of the experimental setup is shown in Fig. 4.11. A  $10\times$  microscope objective lens ( $f=16.5\text{mm}$ ,  $\text{N.A.}=0.25$ ) was used to focus the pump beam, and the pump spot size were varied by changing the distance between the pump lens and sample surface. In a typical experiment, a  $6\mu\text{m}$  diameter pumping spot was used. Since the sapphire substrate is double-side polished and transparent in both visible and UV frequencies, a  $20\times$  microscope objective lens ( $f=9.0\text{mm}$ ,  $\text{N.A.}=0.40$ ) was placed at the back side of the sample for both collection of emitted light and simultaneous measurement of the spatial distribution of lasing mode. Then the emitted light was coupled into a UV fiber, which was connected to a spectrometer with 0.13 nm spectral resolution. The

pump light was blocked by a bandpass filter, while the image of lasing mode profile was projected by the objective lens onto a UV sensitive CCD camera. The sample was also illuminated by a white light source so that we could identify the position of the lasing modes in the photonic lattice.

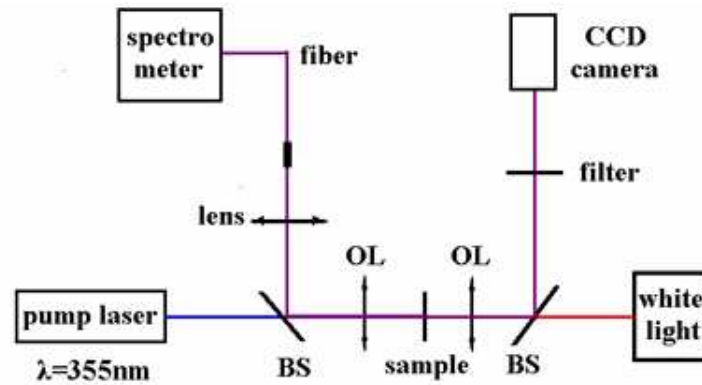


Figure 4.11: A simple sketch of lasing experiment setup on ZnO PhCS samples.

We first studied the patterns with coarse change of  $a$  from 100 nm to 160nm, Among all the fabricated patterns lasing was realized only in the structures of  $a = 115nm$  and  $a = 130nm$ . Figure 4.12(a) shows the spectrum of emission from a pattern with  $a = 115$  nm and  $r/a = 0.25$ . A single narrow lasing peak appeared at 387.7 nm. Figure 4.12(b) plots the laser emission energy as a function of the pumping pulse energy. Note that not all the pump light incident onto the sample was absorbed, part of it was transmitted, reflected, or scattered. It was difficult then to measure the exact percentage of the incident pumping being absorbed. Nevertheless, the threshold behavior is clearly seen in Fig. 4.12(b). Above the threshold, the FWHM of this lasing peak was only 0.24 nm. These data clearly indicated that lasing oscillation occurred in this PhCS structure. The near-field image of this lasing mode was obtained simultaneously and shown in the inset of

Fig. 4.12(a). The white square marks the boundary of the triangular lattice. The lasing mode was spatially localized in a small region of  $\sim 1.0 \mu\text{m}^2$  inside the lattice. As we moved the pump spot across the lattice, the lasing modes changed in both frequency and spatial pattern. This behavior suggested that this lasing mode was a spatially localized defect state. It was formed by the short range structural disorder [136] which was introduced unintentionally during fabrication. Lasing was also observed at longer wavelength for the pattern with  $a=130 \text{ nm}$  and  $r/a = 0.25$  with higher lasing threshold.

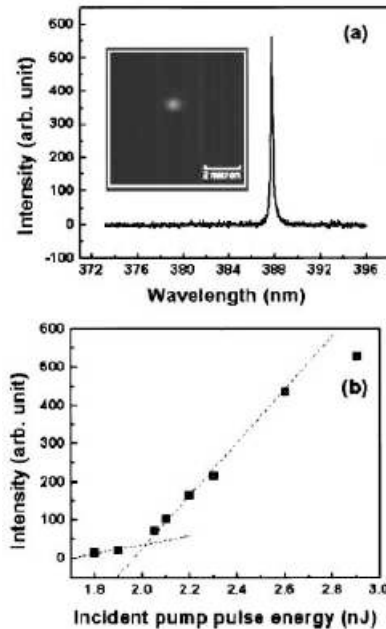


Figure 4.12: (a) Lasing spectrum of a ZnO PhCS with  $a = 115 \text{ nm}$  shows a single defect mode. The pump pulse energy is 2.3 nJ. Inset is the near field image of the lasing mode. (b) Emission intensity of the defect mode vs the incident pump pulse energy.

We would like to point a few experimental facts for our ZnO PhCS lasers. First, the single mode laser typically could only be observed during a small range of pump pulse energy. For the lasing mode shown in Fig. 4.12, single mode emission was only

observed from 2.0 nJ to 3.0 nJ. With higher pump energy, new lasing modes started to appear and multi-mode lasing emission was obtained. For some samples, the single mode emission dominated over a larger pump power range, but eventually more modes would lase at a higher pump energy. Second, even for the samples fabricated from the same template, the lasing emission was different for each sample. However, they were typically confined to a small frequency range, which was related to the PBG of the template structure. Moreover, the lasing modes were not necessary to be spatially localized like the one shown in Fig. 4.12. Actually major number of samples demonstrated lasing modes with certain spatial extension, and sometimes could be extended over almost the entire pattern area. An example is shown in Fig. 4.13, where the boundary of inset also represents the sample pattern boundary. Clearly the single mode laser was an extended mode. Third, the lasing threshold from the hexagonal latticed air cylinder structures was much lower than that from the patterns with randomly positioned air cylinders with the same filling fraction. Lasing from the random structures was generally with multiple peaks in spectrum, and the lasing threshold was one order higher than the PhCS lasers. These lasing modes were random lasers and their high threshold was mainly due to the degrading of ZnO optical quality caused by FIB etching. This fact, on the other hand, illustrated the high quality factor in our PhCS laser cavities. Fourth, to seek PhCS laser with even lower threshold, we checked the effect of the pattern size on lasing threshold. We have prepared the the same lattice structured samples with different pattern sizes:  $4 \times 4$ ,  $6 \times 6$ ,  $8 \times 8$ ,  $12 \times 12$  and  $16 \times 16 \mu m$ . It was observed that when pattern size increased

from  $4 \times 4$  to  $8 \times 8 \mu m$ , the lasing threshold decreased dramatically; while the pattern size increased further, the lasing threshold became very similar. Due to our FIB etching process limit, for the structures made from the same template, the larger the pattern was, the more deviated from the template. Thus for large area samples like  $12 \times 12$  or  $16 \times 16 \mu m$ , the structure disorder made the in-plane PBG effect less dominant, which prevented the further decrease of lasing threshold. Fifth, we tried introducing certain defects into our ZnO PhCS structure by design, e.g., intentional missing one air cylinder (called D1 defect), or one center cylinder plus the nearest neighboring six cylinders (called D2 defect). However, no significant changes were observed for the lasing modes from such structures compared to the structures without any designed defects.

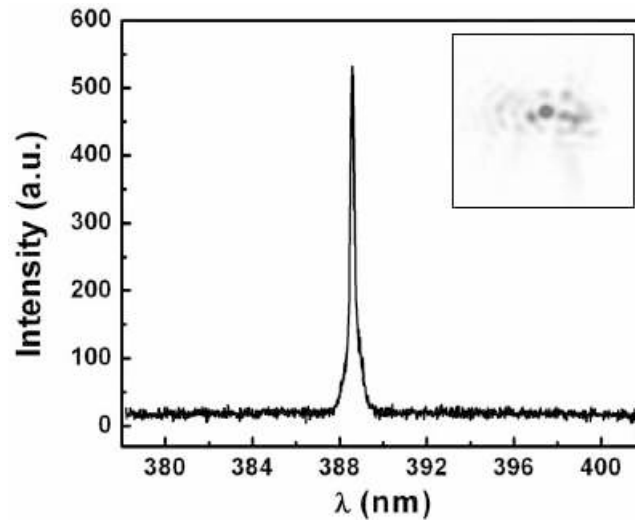


Figure 4.13: A typical lasing spectrum for an extended defect mode close to dielectric band edge. Pump pulse energy: 2.0 nJ. Inset: near field image of the lasing mode, the square boundary represents the boundary of the PhCS pattern.

To confirm the lasing modes (both localized and extended) were truly related to the in-plane photonic crystal structure, we managed to fabricate a series of samples with the

same hexagonal structure yet different lattice constant  $a$ . To overcome the 15 nm pixel resolution limit in the  $8 \times 8 \mu m$  pattern, we carefully change the working distance between the ion gun and the sample surface to change the magnification value. With this method, we successfully fabricated ZnO PhCS samples with  $a$  from 100 nm to 140 nm with step size as fine as 2 nm. The similar laser emission was observed from those samples and the results are shown in Fig. 4.14. In Fig. 4.14(a) the lasing mode wavelength is plotted for samples with different lattice constant  $a$ . It can be seen that the lasing wavelength was linearly scales with  $a$ , which clearly demonstrate the lasing modes were photonic crystal lasers. The threshold pump pulse energy for these lasing modes is shown in Fig. 4.14(b). With a minimum occurred between 110 nm to 125 nm, the lasing threshold quickly increased for samples with both smaller and larger lattice constants. This result was explained by the spectral overlap between the in-plane PBG of ZnO PhCS structures and the ZnO bulk gain. For the structures with  $a$  between 110 nm and 125 nm, the calculated PBG was positioned within the ZnO gain range, 375 nm to 405 nm. While for structures with larger or smaller  $a$ , their PBG was far away from the gain maximum, which made them difficult to lase.

## 4.5 Effect of Disorder on Photonic Crystal Lasers

The reason that different lasing modes were obtained for the samples fabricated under the same template, is because different unavoidable disorder was introduced during the fabrication process into different samples. From the top view SEM image shown in Fig.

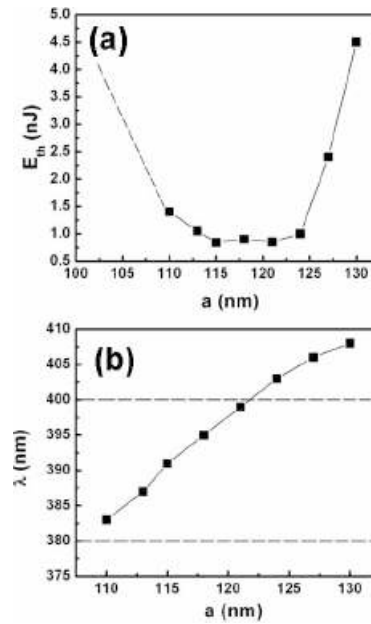


Figure 4.14: (a) Experimentally measured incident pump pulse energy at the lasing threshold as a function of lattice constant  $a$ . Dash line indicates that samples with  $a < 110$  nm don't lase at shown pump pulse energy range. (b) Measured lasing mode wavelength as a function of lattice constant  $a$ . Dash lines at  $\lambda = 380$  nm and  $400$  nm are edges of gain spectrum of ZnO.

4.10, the drilled air cylinders are deviated from perfect circles designed in template, and such deviation distribution is different for different samples. To demonstrate this point more clear, a larger area SEM image, as well as the deviation distribution from the template, is shown in Fig. 4.15. For different samples fabricated under the same template, such deviation distribution could be completely different. The deviation was mainly caused by two factors: one is the intrinsic limit of the FIB etching process, e.g. the different deviation for different air cylinders; the other is the sample or ion beam drift during the long etching process, which is typical a few minutes for a  $8 \times 8 \mu\text{m}$  pattern. We have been trying to optimize all fabrication conditions and the residual deviation is beyond our experimental control. However, such deviation distribution played a crucial

role in the formation of our ZnO PhCS lasing modes. In previous Introduction chapter, we mentioned there are typically two different type of photonic crystal lasers: the defect mode laser and bandedge state laser. The former is spatially confined to the carefully designed defect region and the later is spatially extended. However, the lasing mode observed in our ZnO PhCS is different from both of them. Without any intentionally designed defects, the lasing modes can be either spatially localized or extended due to specific structure deviation distributions in individual sample patterns. The reason that both localized and extended modes can lase under similar pump condition is because the in-plane PBG is rather narrow in our ZnO PhCS structures. Due to the narrow PBG, the FIB introduced disorder can move the bandedge state deep into the gap easily. However, such deep gap defect mode has similar lasing threshold as the bandedge states because the narrow gap becomes very shallow by the addition of defect modes. Thus with the same degree of disorder and pump condition, gap defect mode may lase first for some samples (which is spatially localized), while bandedge state will lase first for others (which is spatially extended). The narrow PBG also explains the small pump energy for single mode operation, since both the gap defect mode and the bandedge states share almost the same threshold. Same explanation applied to the observation that the structures with intentionally designed defects did not show significant difference on laing behaviors.

We know that for a PhCS laser cavity, light may escape vertically through the top/bottom interfaces into air/substrate or laterally via the edge of the periodic pattern into air or unpatterned part of the slab. The vertical leakage rate is characterized

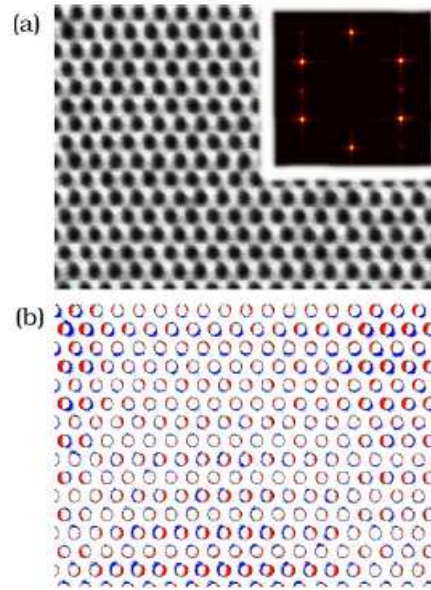


Figure 4.15: (a) Top-view SEM of a ZnO PhCS. The inset shows structural Fourier transform from the digitized SEM. Long-range periodicity is reflected in the six maxima at the positions corresponding to the perfect lattice. (b) Difference between the digitized SEM of real sample and the perfect honeycomb lattice reveals the structural disorder.

by the out-of-plane energy loss per optical cycle  $Q_{\perp}^{-1}$ , and the lateral by  $Q_{//}^{-1}$ . A defect state spatially localized in plane has a large distribution of  $k_{//}$ , thus typically has large leakage in the vertical direction, i.e.,  $Q_{\perp}^{-1} \gg Q_{//}^{-1}$ . For an extended bandedge state, the  $k_{//}$  distribution is small, so the lateral leakage usually dominates over the vertical one,  $Q_{//}^{-1} \gg Q_{\perp}^{-1}$ . The total loss is described by  $Q_{tot}^{-1} = Q_{\perp}^{-1} + Q_{//}^{-1}$ . Low lasing threshold demands maximization of  $Q_{tot}$ , which is hindered by  $Q_{\perp}$  for a localized defect state and  $Q_{//}$  for an extended bandedge state. To improve  $Q_{tot}$ , many works have been done to increase  $Q_{\perp}$  for a localized defect cavity state. For our ZnO PhCS structures, the increase of lasing threshold for smaller patterns indicated that the dominant loss was the lateral leakage for them, while the saturated threshold for larger patterns showed the vertical

leakage instead became the dominant loss. In another word, for patterns smaller than  $8 \times 8 \mu m$ ,  $Q_{//}^{-1} > Q_{\perp}^{-1}$  and  $Q_{tot}$  is dominated by  $Q_{//}$ , thus size increasing reduced the lasing threshold. While for patterns larger than  $8 \times 8 \mu m$ ,  $Q_{//}^{-1} < Q_{\perp}^{-1}$  and  $Q_{tot}$  was dominated by  $Q_{\perp}$ . Therefore as a conclusion: first, the lasing mode is a band edge type of extended mode, second, the vertical leakage dominates when pattern size is larger than  $8 \times 8 \mu m$ .

To quantitatively study the effect of disorder on both defect mode lasers and bandedge state lasers from the photonic crystal slab structures, we consider a system schematically depicted in the inset of Fig. 4.16(a). A dielectric slab of thickness 180 nm and refractive index  $n$  of 2.35 is sandwiched between air and substrate ( $n_{sub} = 1.78$ ). Within the slab,  $N$  infinitely long grooves run parallel to  $y$  axis. The width of a groove is 22 nm, the lattice constant of the disorderless structure is 100 nm. We consider light propagating in the  $x$ - $z$  plane, with the electric field along the  $y$  axis. Such a system is 2D, which allows numerical simulation of large statistical ensembles of random systems. Despite the simplification, the system in Fig. 4.16(a) retains the property essential for our study of ZnO PhCS laser: the possibility of vertical (along the  $z$  axis) and lateral (along the  $x$  axis) radiative escape. Using the FDTD method, we find the mode of the passive system that has the highest  $Q_{tot}$  [136]. A Gaussian pulse was launched at all spatial points in the slab and the energy is allowed to leak out radiatively. The simulation area is terminated by uniaxially perfectly matched absorbing layer that absorbs all outgoing waves. The pulse excites all modes within 30 nm wavelength range around 400 nm. After

the initial multimode decay the field distribution is stabilized and the longest-lived mode can be seen. This is further confirmed by observing a monoexponential decay of the total energy stored in the system that allows determination of  $Q_{tot}$ . By integrating Poynting vector over the corresponding interfaces [1], we obtained the outgoing flux in the vertical and horizontal directions, and  $Q_{\perp}$  and  $Q_{//}$ . In our simulation, the  $Q_{tot}^{-1} = Q_{\perp}^{-1} + Q_{//}^{-1}$  relation was satisfied numerically to within 2%.

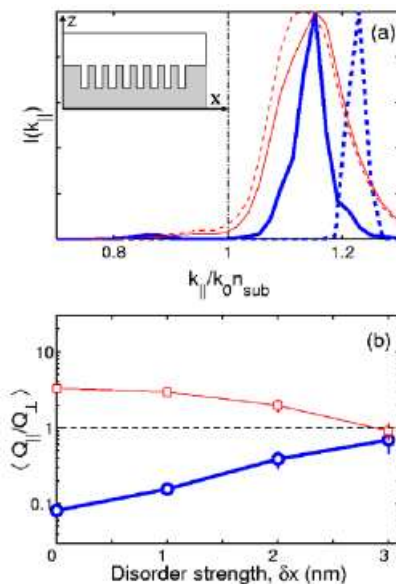


Figure 4.16: (a)  $k_{//}$  distributions of the highest- $Q_{tot}$  modes at one pixel beneath the slab-substrate interface. The thin (thick) dashed curve represents the mode found in the disorderless system ( $N = 24$ ) with (without) an artificial defect. The corresponding solid curves are representative examples of the highest- $Q_{tot}$  modes in these systems with position disorder ( $\delta x = 10$  nm). The vertical line marks the substrate light-cone boundary. The inset is a schematic sketch of the simulated structure. (b) Squares and circles represent  $\langle Q_{//} / Q_{\perp} \rangle$ , averaged over 300 random realizations of  $N = 24$  system with and without the artificial defect, versus disorder strength  $\delta x$ .

Fourier transform of the spatial profile of electric field at the interface between the slab and substrate gives the mode distribution in  $k_{//}$  (in-plane component of the wave

vector) space. In a perfectly periodic structure, the band edge mode has the highest  $Q_{tot}$ . It is spatially extended in  $x$ , thus has a narrow distribution in  $k_{//}$  [thick dashed curve in Fig. 4.16(a)]. Next we intentionally create a defect by increasing the spacing between two neighboring grooves at the center of the pattern to 150 nm. The highest- $Q_{tot}$  mode is localized around this artificial defect with a localization length of 140 nm. Strong localization in  $x$  results in a broad distribution in  $k_{//}$  [thin dashed curve in Fig. 4.16(a)], with the maximum lying closer to the edge of substrate light cone [dash-dotted vertical line in Fig. 4.16(a)]. Its  $Q_{tot}$  is limited by  $Q_{\perp}$ , which is about 3 times smaller than the corresponding  $Q_{//}$  in a system of  $N = 24$ . In contrast, the band edge mode is concentrated well beyond the light cone in  $k_{//}$  space, thus its  $Q_{\perp}$  is much higher. However, its spatial extension makes the lateral leakage larger, hence its  $Q_{tot}$  is limited by  $Q_{//}$ .

To simulate the position disorder of air cylinders in real structure [Fig. 4.15(b)], random variation of groove position  $x_n$  is introduced. We choose  $\Delta x_n$  randomly from a uniform distribution with the standard deviation  $\delta x = 5, 10, 15$  nm.  $\delta x$  characterizes the "strength" of disorder. As the disorder is introduced, the highest- $Q_{tot}$  state differs from realization to realization, and the correspondent  $Q_{//}$ ,  $Q_{\perp}$ , as well as the frequency vary. We study statistical distributions of these parameters and their dependences on disorder strength  $\delta x$  and system size  $N$ .

In small systems ( $N = 12$  and  $24$ ) with an artificial defect and weak disorder ( $\delta x = 5$  nm), the highest- $Q_{tot}$  modes always concentrate around the defect at the center of the

pattern. These modes become more spatially extended than those without disorder. Therefore, their  $k_{//}$  distribution is narrowed and the  $k_{//}$  component within the light cone is significantly reduced [Fig. 4.16(a)]. This reduction leads to a decrease in the vertical leakage, thus, an increase in  $Q_{\perp}$ . Meanwhile,  $Q_{//}$  starts increasing as the mode gets less localized in real space. The ensemble-averaged  $\langle Q_{//}/Q_{\perp} \rangle$ , shown in Fig. 4.16(b), decreases monotonously to unity with increase of disorder strength. Therefore, disorder removes the imbalance between vertical and lateral leakages of a single defect state, making  $\langle Q_{//}/Q_{\perp} \rangle \rightarrow 1$ . As a result, the ensemble-averaged quality factor  $\langle Q_{tot} \rangle$  is slightly higher than that without disorder. In a larger system or with stronger disorder, the highest- $Q_{tot}$  mode is no longer pinned at the artificial defect. Instead, it can explore the entire pattern to find the optimum configuration for the best vertical and lateral confinement. This leads to a further increase of  $\langle Q_{tot} \rangle$ .

With the introduction of disorder, the the band edge mode becomes less extended. As its "tail" moves away from boundaries of the pattern, the lateral leakage decreases, thus  $Q_{//}$  increases. Meanwhile, the distribution in  $k_{//}$  space is broadened and shifted closer to the light-cone edge [Fig. 4.16(a)]. The increase in vertical leakage results in a decrease of  $Q_{\perp}$ . The ensemble-averaged  $\langle Q_{//}/Q_{\perp} \rangle$ , shown in Fig. 4.16(b), rises continuously to unity with increasing disorder strength. Again, disorder balances the vertical and lateral leakages of the band edge mode, as it does to the defect state. However, for a band edge mode the increase in  $\langle Q_{//} \rangle$  is not as large as the decrease in  $\langle Q_{\perp} \rangle$ ; thus  $\langle Q_{tot} \rangle$  is slighter lower than it is without disorder. Nevertheless, as the pattern size  $N$  increases, the total

leakage rate decreases monotonically. This behavior differs fundamentally from that of a photonic crystal waveguide, where optical loss increases exponentially with its length. In contrast, a disordered PhCS laser benefits from an increase of the pattern size, simply because a larger system provides a bigger pool of modes from which the highest- $Q_{tot}$  mode can be selected. This effect should be more pronounced in PhCS microlasers with 2D periodicity [Fig. 4.15(a)], due to the larger phase-space compared to the numerically simulated systems with 1D periodicity.

The calculation demonstrates that the structural disorder may lead to self optimization of optical confinement in a PhCS and formation of high- $Q_{tot}$  modes which serve as the lasing modes. In a sufficiently large PhCS with short-range disorder, a microcavity with balanced  $Q_{\perp}$  and  $Q_{//}$  can be formed spontaneously without any carefully designed structural defects. In our UV PhCS lasers, random scattering by structural disorder leads to in-plane localization of band edge modes. The underlying physical mechanism is similar to that of light localization in random media. The reduction of density of states near photonic band edge enhances the localization effect. The best-confined modes are selectively amplified in the presence of optical gain due to long photon lifetime.

## 4.6 Conclusion

In summary, we have calculated the band structure of ZnO PhCS on sapphire substrate, optimized the band gap by changing the photonic layer thickness, air cylinder radius, and etching depth into the sapphire substrate. A narrow gap has been demonstrated for TE-

like bands which are preferred by the gain of our ZnO film on sapphire. The optimum parameters for a maximum PBG in our ZnO PhCS structure has been obtained and such a PhCS structure has been successfully fabricated by FIB etching techniques. The degrading of ZnO film optical quality by ion bombardment was recovered by post thermal annealing. These ZnO PhCS structures were optically excited at room temperature and single mode lasing has been demonstrated. Moreover, by changing lattice constants, the lasing wavelength was tuned over a 30 nm wavelength range. The lasing modes were identified as edge modes close to the dielectric band with cavity quality self-optimized by the defects introduced during the fabrication process.

## CHAPTER 5

### CONCLUSION AND FUTURE WORK

This thesis presents a study of lasing in multiple light scattering media. Depending on whether the spatial distribution of the scattering structure is random or periodic, the laser can be termed as a random laser or a photonic crystal laser. They are different from laser cavities with well defined boundaries, e.g. the whisper-gallery mode laser, where the interference among multiply “reflected” light determines the lasing mode. The most simple examples that demonstrate the differences between these lasers are the one dimensional laser cavities: a distributed feedback laser (DFB) is a photonic crystal laser, a randomly distributed feedback laser (RDFB) is a random laser, and a Fabry-Perot cavity is a laser cavity with a well defined boundary. In principle, such distinctions are not necessary since all the laser cavities should satisfy both amplitude and phase conditions. However, in this thesis we only focus on the laser cavities with distributed feedback, i.e. where the interference among multiply “scattered” light determines the lasing mode.

We have studied random lasers with resonant feedback in both weakly and strongly scattering media. For the weakly scattering system, we chose the colloidal solution with laser dyes as gain materials in our experiments. By changing the particle density and dye

concentration, we can control the scattering length  $l_s$  and gain length  $l_g$  (and absorption length  $l_a$ ) for both the pump and emission light separately. A semi-1D cone shaped excitation volume was achieved with tight focusing and weak scattering of the pump light. This particular gain geometry gave some special properties to the random laser emission, e.g. the directional output along the backward direction of the pump beam and the near regular multiple peaks in the single shot spectrum whose spacing inversely scaled with the excitation cone length. These characteristics inspired us to carefully investigate the nature of the lasing modes, which bore two important conclusions.

First, we demonstrated the difference between quasimodes of a random system and its lasing modes under local excitation. These two types of modes have been numerically shown to be the same for strongly scattering systems in or close to the localization regime. Such a correspondence was taken for granted in weakly scattering systems, where the lasing modes were considered to be the quasimodes with small decay rates. However, we showed that such close similarity only exists for quasimodes and lasing modes under a global uniform gain. For a weakly scattering system under local excitation, the number of lasing modes can be significantly less than that of quasimodes for the same frequency range, and the number decreases with the local pump region size. The lasing mode number reduction makes the average spacing between neighboring modes increase, which explains the requirement of tight focusing for discrete random laser modes in weakly scattering media. Notice that the difference between lasing modes and quasimodes is the intrinsic consequence of local excitation, which is different from that caused by the

presence of reabsorption of emitted light outside the pumped region. The reabsorption artificially suppresses the feedback from outside the pumped region, which is not necessary because the selective enhancement of feedback within the excitation region itself can change the lasing modes dramatically from the quasimodes of the original passive system. Generally speaking, lasing modes under inhomogeneous excitation will be different from the quasimodes of the passive system, since both type of modes are eigenmodes of the Maxwell's equations and the dielectric constant spatial distribution  $\epsilon(\vec{r}, t)$  is definitely changed by the presence of the inhomogeneous gain. The difference will be rather small if the required gain for lasing modes is small. A good example is the set of spatially localized modes in strongly scattering media which are well overlapped spatially with the excitation. However, for weakly scattering systems in the diffusive or even ballistic regime, the quasimodes are formed by the feedback from the whole system and spatially extended. The required gain for lasing modes is high in such systems and the feedback weight change caused by inhomogeneous gain is thus large, which, in turn changes the lasing modes from quasimodes more dramatically, both in frequency and in their wave function. One important consequence of the difference is that the statistical distribution of decay rates of the quasimodes (neither the original system nor the "reduced" system defined by the excitation region) cannot be applied directly to predict the lasing threshold statistics of random laser modes.

Second, we illustrated the difference between amplified spontaneous emission (ASE) spikes and coherent random laser peaks, both share a similar discrete spiky emission

spectrum. An ASE spike is attributed to a single spontaneous emission event which happens to take long *open* paths inside the amplifying random medium, while a random laser peak is formed by interference of scattered waves which return to a coherence volume via different *closed* paths. The ASE spikes are intrinsically stochastic and their frequencies vary from shot to shot, even with the fixed dielectric constant distribution. The frequencies of lasing peaks, however, are determined by the dielectric constant distribution and will be conserved under the same excitation condition for static  $\epsilon(\vec{r})$ . In a colloidal solution, where the scatterers keep floating, both spikes and peaks vary from shot to shot. However, with increasing pumping energy, lasing peaks dominate over the ASE spikes quickly. In neat dye solution, because of the absence of scatterers, only ASE spikes are observed even under intense excitation. We showed the quantitative differences between ASE spikes and lasing peaks by statistical measurements. In particular, because the ASE spikes originate from independent spontaneous emission events, their frequencies are uncorrelated, leading to a quick decaying spectral correlation under ensemble-average, as well as having Poisson statistics dictate their spectral spacing. While for lasing peaks, different peaks correspond to different lasing modes from the same system, thus their frequencies are correlated. Therefore, an oscillation with the period determined by the non-zero most probable average spacing survives after the same ensemble-average. Their difference also shows in the intensity statistics, where the ASE spikes' intensity follows an exponential tail, while the lasing peak intensity can be better fitted with a power law. Due to the complicate spatial and temporal change of gain caused by intense pulse

pumping, the exact reason behind the two different intensity statistics needs further study. However, our experiments clearly distinguished the difference between ASE spikes and random lasing peaks, which will help people to correctly identify coherent random laser emission from weakly scattering systems.

One main technical concern about random lasers is the high lasing threshold, which needs to be greatly lowered for mass application. Because the feedback for a random laser comes from multiple scattering, one solution is to enhance the strength of scattering within the random media, namely, by decreasing the scattering mean free path  $l_s$ . Since  $l_s = 1/\rho\sigma_s$ , where  $\rho$  is the scatterer density and  $\sigma_s$  is the scattering cross section from a single scatterer, a natural thought to reduce  $l_s$  is to maximize both  $\rho$  and  $\sigma_s$ .  $\rho$  can be maximized by close packing and  $\sigma_s$  can be maximized by utilizing resonant scattering. We have tested this idea by studying random lasing from the closely packed monodisperse ZnO spheres, whose size was tuned to overlap their Mie resonance with the ZnO gain spectrum. First, we developed a chemical reaction process to synthesize monodisperse ZnO spheres with a controllable diameter over a large range (from less than 100 nm to over 600 nm). A large number of these particles were then cold pressed to form a pellet-shaped random sample. The Mie resonance from each sphere was calculated numerically, with its refractive index precisely estimated by the transmission measurement with self-assembled opal structures. Then a coherent backscattering (CBS) experiment was performed with these samples, and the transport mean free path  $l_t$  was derived from the width of the CBS cone. By increasing the sphere diameter  $d$  from sub 100 nm to

about 120 nm,  $l_t$  quickly decreased to about 500 nm and saturated afterwards. This behavior was consistent with the calculation based on  $l_s = 1/\rho\sigma_s$ , with the exception that the measured saturated value of  $l_t$  at larger sphere diameters was larger than the expected value. The discrepancy was explained by dependent scattering, which happens when the scatterers are too close to each other. In another word, the scattering from a single scatterer is affected by the presence of neighboring scatterers, and the independent scattering assumption of the formula  $l_s = 1/\rho\sigma_s$  is broken. The occurrence of dependent scattering was confirmed by our generalized multiple Mie scattering (GMMS) calculation. The measured lasing threshold dependence on sphere size followed similar trends as the transport mean path, which demonstrated that resonant scattering can greatly lower the random lasing threshold before dependent scattering starts.

Two points are worth mentioning for the resonant scattering random systems. First, we were unable to vary the filling fraction  $f$  of the scatterers in our sample over a large range. By adding the control of  $f$ , we can hold the independent scattering assumption for certain  $f$ . Under this condition, whether Ioffe-Regal criteria  $k_e l_s < 1$  can be satisfied still needs further investigation. The  $f$  control can be achieved by several ways experimentally, e.g. by using colloidal solution or by embedding the scatterers into low index shell spheres. Second, we ignored the possibility of existence of locally ordered structures, which can be easily formed in the closely packed monodisperse spheres. Such locally ordered structures may form certain photonic band gaps, which will reduce the density of states at the gap frequency. According to Thouless criterion, light localization will be achieved when the

average mode linewidth  $\delta\omega$  is less than the average mode spacing  $\Delta\omega$ . Therefore, the density of states reduction will increase  $\Delta\omega$  and facilitate light localization and thus lower the lasing threshold.

Besides the random laser, we also studied photonic crystal lasers with ZnO as gain material. Facilitated by band structure calculations and the focused ion beam (FIB) etching technique, we realized the first reported ZnO photonic crystal slab (PhCS) laser, which emits ultraviolet light under optical pumping at room temperature. We developed a super-cell based plane wave expansion method to calculate the band structure of the asymmetric ZnO PhCS structure, where a ZnO layer with a 2D hexagonal lattice formed by air cylinders seated on top of a c-plane sapphire substrate. The photonic band gap of the in-plane periodic structure was optimized by choosing the correct ZnO layer thickness  $t$ , air cylinder radius  $r$  and lattice constant  $a$ . Then the designed structure was etched using the FIB technique, which overcame the fabrication challenge of small feature sizes, e.g.  $a = 100$  nm and  $r = 25$  nm. The ion etching process damaged the ZnO crystal structure severely, and its optical quality was partially recovered by post thermal annealing. Single mode lasers, both spatially localized and extended, were realized from these PhCS structures, and the lasing frequency has been finely tuned across the whole ZnO gain spectrum range by varying the in-plane lattice constant. Due to the small feature size of the ZnO PhCS structure, the unavoidable defects introduced by the FIB etching process were relatively large. However, unlike in the wave propagation case, such defects were shown not to be very detrimental to lasing in PhCS structures. The reason was

because the disorder induced a balance between vertical and lateral energy leakage. The threshold of ZnO PhCS lasers can be further lowered by reducing both the structure defects and optical quality damage introduced during fabrication, which could be achieved by some alternative fabrication methods other than FIB, e.g. E-beam lithography and reactive ion etching. The PhCS structure can be further optimized by undercutting the substrate, if possible, to make the structure symmetric and reduce the vertical loss by better waveguiding.

We have only studied lasing from either random or periodic structures, with the addition of periodic structures with a small amount of disorder. It would be interesting to map over an entire crossing from periodic structures to random structures, and investigate the lasing behavior from structures with different degrees of disorder. We have numerically studied this problem in two dimensional systems by using FDTD calculations, and found that a certain optimum degree of disorder exists for lowering the lasing threshold. It would be fruitful to experimentally test this theory, and also extend the study to the more general three dimensional systems.

## REFERENCES

- [1] J. D. Jackson, *Classical Electrodynamics*, (J. Wiley, New York, 1998).
- [2] C. F. Bohren and D. R. Huffman, *Absorption and Scattering of Light by Small Particles*, (J. Wiley, New York, 1983).
- [3] H. C. van de Hulst, *Light Scattering by Small Particles*, (Dover, New York, 1981).
- [4] A. Z. Genack, Phys. Rev. Lett. **58**, 2043 (1987).
- [5] K. Busch, C. M. Soukoulis, and E. N. Economou, Phys. Rev. B **50**, 93 (1994).
- [6] A. Ishimaru, *Wave Propagation and Scattering in Random Media* (Academic, New York, 1978).
- [7] C. I. Beard, T. H. Kays, and V. Twersky, IEEE Trans. Antennas Propag. **15**, 99 (1967).
- [8] E. Akkermans, P. E. Wolf, and R. Maynard, Phys. Rev. Lett. **56**, 1471 (1986).
- [9] E. Akkermans, P. E. Wolf, R. Maynard, and G. Maret, Journal de Physique, **1**, 77 (1987).

- [10] M. P. van Albada, M. B. van der Mark, and A. Lagendijk, *Phys. Rev. Lett.* **58**, 361 (1987).
- [11] S. Etemad, R. Thompson, M. J. Andrejco, S. John, and F. C. Mackintosh, *Phys. Rev. Lett.* **59**, 1420 (1987).
- [12] A. Yu. Zyuzin, *Europhys. Lett.* **26**, 517 (1994).
- [13] D. S. Wiersma, M. P. van Albada, and A. Lagendijk, *Phys. Rev. Lett.* **75**, 1739 (1995).
- [14] P. W. Anderson, *Phys. Rev.* **109**, 1492 (1958).
- [15] J. T. Edwards, and D. J. Thouless, *J. Phys.* **C5**, 807 (1972).
- [16] E. Abrahams, P. W. Anderson, D. C. Licciardello, and T. V. Ramakrishnan, *Phys. Rev. Lett.* **42**, 673 (1979).
- [17] A. F. Ioffe, and A. R. Regel, *Prog. Semicond.* **4**, 237 (1960).
- [18] S. John, *Phys. Rev. Lett.* **53**, 2169 (1984).
- [19] P. W. Anderson, *Phil. Mag.* **52** 505 (1985).
- [20] P. Sheng, and Z. Zhang, *Phys. Rev. Lett.* **57**, 1879 (1986).
- [21] S. John, *Phys. Rev. Lett.* **58**, 2486 (1987).
- [22] A. Z. Genack, and N. Garcia, *Phys. Rev. Lett.* **66**, 2064 (1991).

- [23] D. S. Wiersma, P. Bartolini, A. Lagendijk, and R. Righini, *Nature* **390**, 671 (1997).
- [24] F. Scheffold, R. Lenke, R. Tweer, and G. Maret, *Nature* **398**, 206 (1999).
- [25] D. S. Wiersma, J. G. Rivas, P. Bartolini, A. Lagendijk, and R. Righini, *Nature* **398**, 207 (1999).
- [26] F. J. P. Schuurmans, M. Megens, D. Vanmaekelbergh, and A. Lagendijk, *Phys. Rev. Lett.* **83**, 2183 (1999).
- [27] A. A. Chabanov, M. Stoytchev, and A. Z. Genack, *Nature* **404**, 850 (2000).
- [28] A. A. Chabanov, and A. Z. Genack, *Phys. Rev. Lett.* **87**, 153901 (2001).
- [29] M. Storzer, P. Gross, C. M. Aegerter, and G. Maret, *Phys. Rev. Lett.* **96**, 063903 (2006).
- [30] Z. Q. Zhang, C. C. Wong, K. K. Fung, Y. L. Ho, W. L. Chan, S. C. Kan, T. L. Chan, and N. Cheung, *Phys. Rev. Lett.* **81**, 5540 (1998).
- [31] Yu. A. Vlasov, M. A. Kaliteevski, and V. V. Nikolaev, *Phys. Rev. B* **60**, 1555 (1999).
- [32] H. Cao, *Wave in Random Media*, **13**, R1 (2003).
- [33] H. Cao, *J. Phys. A* **38** 10497 (2005).
- [34] V. S. Letokhov, *Sov. Phys. JETP* **26**, 1246 (1968).

- [35] V. M. Markushev, N. E. Ter-Garielyan, Ch. M. Briskina, V. R. Belan, and V. V. Zolin, *Sov. J. Quan. Electron.* **20**, 773 (1990).
- [36] N. M. Lawandy, R. M. Balachandran, A. S. L. Gomes, and E. Sauvain, *Nature* **368**, 436 (1994).
- [37] H. Cao, Y. G. Zhao, H. C. Ong, S. T. Ho, J. Y. Dai, J. Y. Wu, and R. P. H. Chang, *Appl. Phys. Lett.* **73**, 3656 (1998).
- [38] H. Cao, Y. G. Zhao, H. C. Ong, S. T. Ho, E. W. Seelig, Q. H. Wang, and R. P. H. Chang, *Phys. Rev. Lett.* **82**, 2278 (1999).
- [39] H. Cao, Y. Ling, J. Y. Xu, C. Q. Cao, and P. Kumar, *Phys. Rev. Lett.* **86**, 4524 (2001).
- [40] Y. Ling, H. Cao, A. L. Burin, M. A. Ratner, X. Liu, and R. P. H. Chang, *Phys. Rev. A* **64**, 063808 (2001).
- [41] H. Cao, J. Y. Xu, S. H. Chang, and S. T. Ho, *Phys. Rev. E* **61**, 1985 (2000).
- [42] S. V. Frolov, Z. V. Vardeny, K. Yoshino, A. A. Zakhidov, and R. H. Baughman, *Phys. Rev. B* **59**, R5284 (1999).
- [43] R. C. Polson, J. D. Huang, and Z. V. Vardeny, *Synth. Met.* **119**, 7 (2001).
- [44] S. V. Frolov, Z. V. Vardeny, K. Yoshino, A. A. Zakhidov, and R. H. Baughman, *Opt. Commun.* **162**, 241 (1999).

- [45] S. V. Frolov, M. Shkunov, A. Fujii, K. Yoshino, and Z. V. Vardeny, *IEEE J. Quantum Electron.* **36**, 2 (2000).
- [46] K. Yoshino, S. Tatsuhara, Y. Kawagishi, and M. Ozaki, *Appl. Phys. Lett.* **74**, 2590 (1999).
- [47] R. C. Polson, A. Chipouline, and Z. V. Vardeny, *Adv. Mater.* **13**, 760 (2001).
- [48] R. C. Polson, and Z. V. Vardeny, *Appl. Phys. Lett.* **85**, 1289 (2004).
- [49] R. C. Polson, and Z. V. Vardeny, *Phys. Rev. B* **71**, 045205 (2005).
- [50] V. M. Apalkov, M. E. Raikh, and B. Shapiro, *Phys. Rev. Lett.* **89**, 016802 (2002).
- [51] A. Yamilov, X. Wu, H. Cao, and A. Burin, *Opt. Lett.* **30**, 2430 (2005).
- [52] E. Yablonovitch, *Phys. Rev. Lett.* **58**, 2059 (1987).
- [53] H. Yokoyama, and S. D. Brorson, *J. Appl. Phys.* **86**, 4801 (1989).
- [54] G. Bjork, and Y. Yamamoto, *IEEE J. Quan. Electron.* **27**, 2386 (1991).
- [55] H. Kogelnik, and C. V. Shank, *Appl. Phys. Lett.* **18**, 152 (1971).
- [56] H. Kogelnik, and C. V. Shank, *J. Appl. Phys.* **43**, 2327 (1972).
- [57] V. I. Kopp, B. Fan, H. K. M. Vithana, and A. Z. Genack, *Opt. Lett.* **23**, 1707 (1998).

- [58] M. Meier, A. Mekis, A. Dodabalapur, A. Timko, R. E. Slusher, J. D. Joannopoulos, and O. Nalamasu, *Appl. Phys. Lett.* **74**, 7 (1999).
- [59] O. Painter, R. K. Lee, A. Scherer, A. Yariv, J. D. O'Brien, P. D. Dapkus, and I. Kim, *Science* **284**, 1819 (1999).
- [60] C. Vanneste and P. Sebbah, *Phys. Rev. Lett.* **87**, 183903 (2001).
- [61] X. Y. Jiang, and C. M. Soukoulis, *Phys. Rev. E* **65**, 025601 (2002).
- [62] V. Milner and A. Z. Genack, *Phys. Rev. Lett.* **94**, 073901 (2005).
- [63] X. Wu, A. Yamilov, A. A. Chabanov, A. A. Asatryan, L. C. Botten, and H. Cao, *Phys. Rev. A*, **74**, 053812 (2006).
- [64] A. L. Burin, M. A. Ratner, H. Cao, and R. P. H. Chang, *Phys. Rev. Lett.* **87**, 215503 (2001).
- [65] M. Patra, *Phys. Rev. E*, **67**, 016603 (2003).
- [66] G. Hackenbroich, *J. Phys. A: Math. Gen.* **38**, 10537 (2005).
- [67] F. A. Pinheiro and L. C. Sampaio, *Phys. Rev. A* **73** 013826 (2006).
- [68] K. L. van der Molen, A. P. Mosk, and A. Lagendijk, *Phys. Rev. A* **74**, 053808 (2006).
- [69] L. I. Deych, *Phys. Rev. Lett.* **95**, 043902 (2005).
- [70] H. E. Türeci, A. D. Stone and B. Collier, *Phys. Rev. A* **74**, 043822 (2006).

- [71] S. Mujumdar, M. Ricci, R. Torre, and D. S. Wiersma, Phys. Rev. Lett. **93**, 053903 (2004).
- [72] F. A. Korolev, G. V. Abrosimov, A. I. Odintsov, and V. P. Yakunin, Opt. Spectrosc. **28**, 540 (1970); F. A. Korolev, V. I. Atroshchenko, S. A. Bakhramov, and V. I. Odintsov, *ibid* **34** 591 (1973).
- [73] V. I. Ishchenko, V. N. Lisitsyn, A. M. Razhev, S. G. Rautian, and A. M. Shalagin, JETP Lett. **19** 346 (1974).
- [74] F. A. Korolev, A. I. Odintsov, N. G. Turkin, and V. P. Yakunin, Sov. J. Quant. Electron. **5** 237 (1975).
- [75] V. Ye. Brazovsky and V. N. Lisitsyn, Appl. Phys. **18** 421 (1979).
- [76] Z. Bor, S. Szatmari, and A. Muller, Appl. Phys. B **32**, 101 (1983).
- [77] P. Sperber, W. Spangler, B. Meier and A. Penzkofer, Opt. Quantum Electron. **20**, 395 (1988).
- [78] A. A. Chastov and O. L. Lebedev, Sov. Phys. JETP **31** 455 (1970).
- [79] V. I. Bezrodnyi, V. I. Vashchuk, and E. A. Tikhonov, Sov. Phys. Tech. Phys. **23** 89 (1978).
- [80] A. Vogel, K. Nahen, D. Theisen, and J. Noack, IEEE J. Sel. Topic. Quant. Electron. **2** 847 (1996).

- [81] D. S. Wiersma, M. P. van Albada, and A. Lagendijk, *Nature (London)* **373**, 203 (1995).
- [82] B. R. Prasad, H. Ramachandran, A. K. Sood, C. K. Subramanian, and N. Kumar, *Appl. Opt.* **36**, 7718 (1997).
- [83] D. S. Wiersma and A. Lagendijk, *Phys. Rev. E* **54**, 4256 (1996).
- [84] S. John, and G. Pang, *Phys. Rev. A* **54**, 3642 (1996).
- [85] G. A. Berger, M. Kempe, and A. Z. Genack, *Phys. Rev. E* **56**, 6118 (1997).
- [86] A. Taflove and S. C. Hagness, *Computational Electrodynamics: the finite-difference time-domain method* (Artech, 2000).
- [87] B. Wilhelmi, *Microwave and Optical Tech. Lett.* **17**, 111 (1998).
- [88] A.A. Asatryan, L.C. Botten, N.A. Nicorovici, R.C. McPhedran, and C.M. de Sterke, *Waves in Random and Complex Media*, **16**, 151 (2006).
- [89] L. C. Botten "From Multipole Theory to Photonic Crystal Device Modeling", Chapter 2 in *Electromagnetic Theory and Applications for Photonic Crystals*, Ed. K. Yasumoto, CRC Taylor and Francis (2006).
- [90] S. M. Dutra, and G. Nienhuis, *Phys. Rev. A* **62**, 063805 (2000).
- [91] X. Y. Jiang, and C. M. Soukoulis, *Phys. Rev. B* **59**, R9007 (1999).
- [92] C. Vanneste, P. Sebbah, and H. Cao, unpublished.

- [93] C. W. J. Beenakker, *Rev. Mod. Phys.* **69**, 731 (1997).
- [94] H. Cao, Y. Ling, J. Y. Xu, and A. L. Burin, *Phys. Rev. E* **66**, R25601 (2002).
- [95] H. Cao, Y. G. Zhao, X. Liu, E. W. Seelig, and R. P. H. Chang, *Appl. Phys. Lett.* **75**, 1213 (2000).
- [96] Feng Y, and Ueda K, *Phys. Rev. A* **68**, 025803 (2003).
- [97] Q. Song, L. Liu, S. Xiao, X. Zhou, W. Wang, and L. Xu, *Phys. Rev. Lett.* **96**, 033902 (2006).
- [98] M. A. Noginov, I. N. Fowlkes, and G. Zhu, *Appl. Phys. Lett.* **86**, 161105 (2005).
- [99] D. Jezequel, J. Guenot, N. Jouini, F. Fievet, *Mater. Sci. Forum* **152-153**, 339 (1994).
- [100] Eric. W. Seelig, Ph.D. thesis, Northwestern University.
- [101] E. W. Seelig, B. Tang, A. Yamilov, H. Cao, and R. P. H. Chang, *Mater. Chem. Phys.* **80**, 257 (2003).
- [102] H. Cao, J. Y. Xu, E. W. Seelig, and R.P.H. Chang, *Appl. Phys. Lett.* **76**, 2997 (2000).
- [103] [http://ab-initio.mit.edu/wiki/index.php/MIT\\_Photonic\\_Bands](http://ab-initio.mit.edu/wiki/index.php/MIT_Photonic_Bands)
- [104] J. X. Zhu, D. J. Pine, and D. A. Weitz, *Phys. Rev. A* **44**, 3948 (1991).

- [105] S. Kawato, T. Hattori, T. Takemori, and H. Nakatsuka, *Phys. Rev. B* **58**, 6180 (1998).
- [106] C. M. Soukoulis, M. Datta, and E. N. Economou, *Phys. Rev. B* **49** 3800 (1994).
- [107] Y. L. Xu, *Appl. Opt.* **36**, 9496 (1997).
- [108] A. Yamilov, and H. Cao, *Phys. Rev. B* **68** 085111 (2003).
- [109] E. Hoskinson, and Z. Ye, *Phys. Rev. Lett.* **83**, 2734 (1999).
- [110] P. Sebbah, and C. Vanneste, *Phys. Rev. B* **66**, 144202 (2002).
- [111] N. L. Swanson, and D. B. Billard, *Phys. Rev. E* **61**, 4518 (2000).
- [112] C. A. Condat, and T. R. Kirkpatrick, *Phys. Rev. B* **36**, 6782 (1987).
- [113] D. Sornette, and B. Souillard, *Europhys. Lett.* **7**, 269 (1988).
- [114] B. A. van Tiggelen, A. Lagendijk, A. Tip, and G. F. Reiter, *Europhys. Lett.* **15**, 535 (1991).
- [115] A. Lagendijk, and B. A. van Tiggelen, *Phys. Rep.* **270**, 143 (1996).
- [116] C. Vanneste, and P. Sebbah, *Phys. Rev. E* **71**, 026612 (2005).
- [117] L. F. Rojas-Ochoa, J. M. Mendez-Alcaraz, J. J. Saenz, P. Schurtenberger, and F. Scheffold, *Phys. Rev. Lett.* **93**, 073903 (2004).

- [118] T. F. Krauss, R. M. De La Rue, and S. Brand, *Nature* **383**, 699 (1996).
- [119] S. Noda, A. Chutinan, and M. Imada, *Nature* **407**, 608 (2000).
- [120] E. Chow, S. Lin, S. G. Johnson, P. R. Villeneuve, J. D. Joannopoulos, J. R. Wendt, G. A. Vawter, W. Zubrzycki, H. Hou, and A. Alleman, *Nature* **407**, 983 (2000).
- [121] C. M. Soukoulis, ed. “*Photonic Crystals and Light Localization in the 21st Century*” (Kluwer Academic, Dordrecht, 2001).
- [122] Y. Akahane, T. Asano, B. Song, and S. Noda, *Nature* **425**, 944 (2003).
- [123] M. Soljacic, and J. D. Joannopoulos, *Nature Materials* **3**, 211 (2004).
- [124] M. Imada, S. Noda, A. Chutinan, T. Tokuda, M. Murata, and G. Sasaki, *Appl. Phys. Lett.* **75**, 316 (1999).
- [125] H. Benisty, C. Weisbuch, D. Labilloy, M. Rattier, C. J. M. Smith, T. F. Krauss, R. M. De La Rue, R. Houdre, U. Oesterle, C. Jouanin, and D. Cas-sagne, and D. Jang, *IEEE J. Lightwave Technol.* **17**, 2063 (1999).
- [126] J. K. Hwang, H. Y. Ryu, D. S. Song, I. Y. Han, H. W. Song, H. K. Park, Y. H. Lee, and D. H. Jang, *Appl. Phys. Lett.* **76**, 2982 (2000).
- [127] M. Loncar, T. Yoshie, A. Scherer, P. Gogna, Y. M. Qiu, *Appl. Phys. Lett.* **81**, 2680 (2002).

- [128] H.-Y. Ryu, S.-H. Kwon, Y.-J. Lee, Y.-H. Lee, and J.-S. Kim, *Appl. Phys. Lett.* **80**, 3476 (2002).
- [129] H.G. Park, S.H. Kim, S.H. Kwon, Y.G. Ju, J.K. Yang, J.H. Baek, S.B. Kim, and Y.H. Le, *Science* **305**, 1444 (2004).
- [130] S. G. Johnson, S. Fan, P. R. Villeneuve, J. D. Joannopoulos, and L. A. Kolodziejski, *Phys. Rev. B* **60**, 5751 (1999).
- [131] S. F. Yu, C. Yuen, S. P. Lau, and W. J. Fan, *IEEE J. Quant. Electron.* **40** 406 (2004); S. F. Yu, C. Yuen, S. P. Lau, W. I. Park, and G.-C. Yi, *Appl. Phys. Lett.* **84**, 3241 (2004).
- [132] X. Wu, A. Yamilov, X. Liu, R. P. H. Chang and H. Cao, *Appl. Phys. Lett.* **85**, 3657 (2004).
- [133] R. Ferrini, R. Houdré, H. Benisty, M. Qui, and J. Moosburger, *J. Opt. Soc. Am. B* **20**, 469 (2003).
- [134] As discussed in Ref. [120], altering the substrate (by extending the air hole into it) also changes the position and the shape of the correspondent light-cone. This effect was not taken into account in our calculation since we believe it should not substantially change our optimization results.
- [135] Xiang Liu, Ph.D. thesis, Northwestern University.
- [136] A. Yamilov and H. Cao, *Phys. Rev. A* **69**, 031803 (2004).